UNIVERSITÄTSKLINIKUM HAMBURG-EPPENDORF

Institut für experimentelle Immunologie und Hepatologie

PD. Dr. rer. nat. Andrea Kristina Horst

Role of myeloid pyruvate kinase isoform M2 (PKM2) in homeostasis and acute liver inflammation

Dissertation

zur Erlangung des Grades eines Doktors der Medizin

an der Medizinischen Fakultät der Universität Hamburg

vorgelegt von

Jan Philipp Weltzsch

aus Hamburg

2021

Contents

1 Introduction

1.1 Innate immune cells

1.1.1 Development and origin of myeloid immune cells

1.1.2 Monocytes and Macrophages

1.1.3 Dendritic cells

1.1.4 Granulocytes

1.2 Immunometabolism in myeloid cells

1.2.1 Glycolysis

1.2.2 Oxidative phosphorylation

1.2.3 Lipid metabolism

1.2.4 Warburg effect

1.2.5 Reactive oxygen species

1.3 Liver homeostasis and immunity

1.3.1 Hepatic immune cell populations

1.3.2 Non-alcoholic fatty liver disease

1.3.3 Autoimmune hepatitis

Autoimmune hepatitis (AIH) is regarded a rare disease with an estimated prevalence of approximately 25 per 100.000 in the Western hemisphere (Manns, 2011 Groenbaek). Women are more likely to suffer from AIH: Depending on the subtype, the gender ratio reaches from 4:1 to 10:1 (Al-Chalabi et al., 2008). To date, the disease's cause and pathogenesis still remain largely unknown. The current understanding of its underlying pathological mechanisms includes an individual genetic predisposition (MHC/HLA molecules, Donaldson, 2004), impaired immunological tolerance (e.g. insufficient function of regulatory T cells (T_{reg}, Longhi et al., 2006) and an arising autoreactivity against hepatic autoantigens (e.g. CYP2D6 or asialoglycoprotein receptor, Treichel et al., 1994). AIH can be provoked by exogenous triggers, such as hepatitis viruses (Vento et al., 1991) or members of the family of *herpesviridae* (Manns et al., 1991), as well as various pharmaceuticals including (among many others) diclofenac or statins (Alla et al., 2006). A sequence of pathological events is believed to result in the clinical presentation of AIH patients (Heneghan et al., 2013). First, a genetically susceptible individual is exposed to an exogenous trigger, which is in turn taken up and presented via MHC molecules on an antigen presenting cell or even hepatocytes. The presented fragment of the antigen might resemble cellular compounds found on hepatocytes (molecular mimicry) and lead to the proliferation of antigen-specific B and T cells. In a healthy and non-susceptible

individual, these autoreactive T cells would be hindered by T_{reg}. In this case, however, an impaired self-tolerance leads to the initiation of an autoimmune response against hepatocytes or hepatic antigens, which is amplified by the recruitment of non-antigen specific effector cells (myeloid cells, NKT cells etc.).

The involvement of myeloid cells in the pathogenesis and perpetuation of AIH is poorly characterized. Due to the proposed etiological cascade mentioned above, most research focuses on the adaptive immune response. Very little is known about the myeloid contribution to the hepatic parenchymal damage in the context of AIH. Impaired phagocytosis and antigen presentation by KC and peripheral blood mononuclear cells (PMC) have been linked to a poor outcome in AIH patients (Lin et al., 2016), and an immune cross-talk between myeloid cells and Th1/Th17 cells has been shown in a murine model of immune-mediated hepatitis via STAT3 and STAT1 (Lafdil et al., 2009).

1.4 Hypotheses and aims of this study

2 Materials and Experimental Methods

2.1 Materials

2.1.1 Technical equipment

Technical equipment	Manufacturer
ATILON ATL-423-I Laboratory Balance	Acculab GmbH, Göttingen, Germany
BD FACSCanto™ II	Beckton Dickinson, Franklin James, NJ, USA
BD LSRFortessa™	Beckton Dickinson, Franklin James, NJ, USA
BZ-9000 Fluorescence Microscope	Keyence Corporation, Osaka, Japan
C1000 Thermal Cycler	Bio-Rad, Hercules, CA, USA
CFX96™ Real-Time PCR Detection System	Bio-Rad, Hercules, CA, USA
Centrifuge 5417R	Eppendorf, Hamburg, Germany
Centrifuge 5427R	Eppendorf, Hamburg, Germany
CK40 Inverted Microscope	Olympus, Hamburg, Germany
COBAS Integra 400 plus Analyzer®	Roche, Basel, Switzerland
Eppendorf Research® plus Pipettes • Single-channel pipettes (0.1-2.5µl, 0.5-10µl, 2-20µl, 10-100µl, 20-200µl, 100-1000µl) • 8-channel pipette (10-100µl)	Eppendorf, Hamburg, Germany
Eppendorf Thermomixer 5436	Eppendorf, Hamburg, Germany
FlexCycler, PCR Thermo Cycler	Analytik Jena AG, Jena, Germany
Forma™ 900 Series -86°C Upright Ultra-Low Temperature Freezer	Fisher Scientific GmbH, Schwerte, Germany
Galaxy® 48R CO_2 Incubator	Eppendorf, Hamburg, Germany
HandyStep® Repetitive Pipette	BRAND GmbH, Wertheim, Germany
HERAcell® 240 CO_2 Incubator	Thermo Fisher Scientific, Waltham, MA, USA
IK Comfort Series Fridge	Liebherr-Hausgeräte GmbH, Ochsenhausen, Germany
IKA-COMBIMAG RCT Heated Magnetic Stirrer	IKA-Werke GmbH & Co.KG, Staufen, Germany
KL2 Shaker	Edmund Bühler GmbH, Bodelshausen, Germany
LAUDA ecoline 011 Water Bath	LAUDA Dr. R. Wobser GmbH & Co.KG, Lauda-Koenigshofen, Germany
Mini Trans-Blot® Cell	Bio-Rad, Hercules, CA, USA
Molecular Imager® VersaDoc™ 4000 MP Imaging System	Bio-Rad, Hercules, CA, USA
MSC Advantage™ Class II Biological Safety Cabinet	Thermo Fisher Scientific, Waltham, MA, USA
MyCycler® Thermal Cycler	Bio-Rad, Hercules, CA, USA
NanoDrop ND-1000	PEQLAB Biotechnologie, Erlangen, Germany
Neubauer Improved Hemocytometer	Carl Roth GmbH & Co.KG, Karlsruhe, Germany
Pipetboy® Acu 2	Integra Biosciences AG, Biebertal, Germany
PowerPac® 200	Bio-Rad, Hercules, CA, USA
PowerPac® HC Power Supply	Bio-Rad, Hercules, CA, USA
Privileg PFVN 246W A++ -20°C Freezer	Bauknecht Hausgeräte GmbH, Stuttgart, Germany
Tube Roller Mixer SRT9	Cole-Parmer, Vernon Hills, IL, USA
Tube Racks	A. Hartenstein, Würzburg, Germany
Seahorse XFe96 Analyzer	Agilent Technologies Inc., Santa Clara, CA, USA

Stuart Tube Rotator SB2	Cole-Parmer, Vernon Hills, IL, USA
Tecan Infinite M200 Plate Reader	Tecan, Crailsheim, Germany
Thermoleader Dry Block Heat Bath	UniEquip, Planegg, Germany
TissueLyser II	Qiagen, Venlo, Netherlands
VACUSAFE^{TM} Comfort Suction Pump System	Integra Biosciences, Wallisellen, Switzerland
Vortex Mixer	Heidolph, Schwabach, Germany
XCell SureLock^{TM} Electrophoresis System	Thermo Fisher Scientific, Waltham, MA, USA

Table 1: Technical laboratory equipment.

2.1.2 Software

Software	**Developer**
Adobe Indesign	Adobe Inc., San José, CA, USA
BD FACSDiva^{TM}	Beckton Dickinson, Franklin James, NJ, USA
Bio-Rad CFX Manager 2.0	Bio-Rad, Hercules, CA, USA
BZ-II Analyzer	Keyence Corporation, Osaka, Japan
BZ-II Viewer	Keyence Corporation, Osaka, Japan
FlowJo^{TM} 10.5.3	FlowJo LLC, Ashland, OR, USA
GraphPad Prism 6, 9	GraphPad Software Inc., San Diego, CA, USA
ImageLab^{TM} 2.0	Bio-Rad, Hercules, CA, USA
LEGENDplex^{TM} Data Analysis Software v8	BioLegend Inc., San Diego, CA, USA
Mendeley Desktop v1.19	Mendeley Ltd., London, U.K.
Microsoft Office 2016	Microsoft Corporation, Redmond, WA, USA
Overleaf LaTeX Editor	Overleaf c/o Digital Science, London, U.K.
Quantity One® Software	Bio-Rad, Hercules, CA, USA
Seahorse Wave Desktop Software	Agilent Technologies Inc., Santa Clara, CA, USA
Tbase v16	4D Germany, Eching, Germany
Tecan Magellan^{TM} Software v6.5	Tecan, Crailsheim, Germany

Table 2: Computer software.

2.1.3 Laboratory consumables

Consumable	Manufacturer
BD 2 Pc Discardit II^{TM} syringes (2ml, 5ml)	Beckton Dickinson, Franklin James, NJ, USA
Cell culture dishes (60mm, 100mm)	Sarstedt, Nümbrecht, Germany
Cell culture flasks (25cm^2, 75cm^2, 175cm^2)	Sarstedt, Nümbrecht, Germany
Cell culture plates (6-well, 24-well, 96-well, flat bottom, round bottom, v bottom), Polystyrene	Sarstedt, Nümbrecht, Germany
Cell scraper, 1.7cm with 2-position blade	Sarstedt, Nümbrecht, Germany
Cell strainer, 100µm, Nylon	Corning Inc., Corning, NY, USA
Cover slips, 21×26mm	Gerhard Menzel GmbH, Braunschweig, Germany
Injekt-F® syringes (1ml)	B. Braun Melsungen AG, Melsungen, Germany
Microscope slides	Glaswarenfabrik Karl Hecht GmbH & Co.KG, Sondheim, Germany
NuPAGE Bis-Tris Gradient Gels, 4-12%, 15-well	Thermo Fisher Scientific, Waltham, MA, USA
Parafilm M®	Pechiney Plastic Packaging Inc., Chicago, IL, USA
PCR SingleCap Softstrips (8-well), DNA-, DNAse-, RNAse-free, 0.2ml	Biozym Scientific GmbH, Hessisch Oldendorf, Germany
Pipette tips (10µl, 200µl, 1000µl)	Sarstedt, Nümbrecht, Germany
Pipette tips, sterile, RNAse free (10µl, 200µl, 1000µl)	Sarstedt, Nümbrecht, Germany
Pipettes (2ml, 5ml, 10ml, 25ml, 50ml)	Sarstedt, Nümbrecht, Germany
Positive displacement tips (0.5ml, 5ml, 12.5ml)	BRAND GmbH, Wertheim, Germany
Reaction tubes (1.5ml, 2ml)	Sarstedt, Nümbrecht, Germany
Reaction tubes, conical/non-conical (15ml, 50ml)	Sarstedt, Nümbrecht, Germany
Reaction tubes, sterile, RNAse free (1.5ml, 2ml)	Sarstedt, Nümbrecht, Germany
SafeSeal® reaction tubes (1.5 ml, 2ml)	Sarstedt, Nümbrecht, Germany
Surgical blades No. 20	Feather Safety Razor Co., Osaka, Japan
Stericup-GP® Sterile Vacuum Filtration System	Merck KGaA, Darmstadt, Germany
Sterican® cannulae (23 G, 24 G, 27 G, 30 G)	B. Braun Melsungen AG, Melsungen, Germany
Tubes for flow cytometry, 5ml	Sarstedt, Nümbrecht, Germany
Weighing paper 90×115m	Macherey-Nagel GmbH & Co.KG, Düren, Germany

Table 3: Laboratory equipment.

2.1.4 Kits and reagents

Kit/Reagent	Manufacturer
2-Hydroxy-Propyl-β-Cyclodextrin	Sigma-Aldrich, St. Louis, MO, USA
Adenosine Triphosphate (ATP)	InvivoGen, San Diego, CA, USA
Agarose	Thermo Fisher Scientific, Waltham, MA, USA
Alanine Aminotransferase (ALT) Assay	Roche, Basel, Switzerland
Ammonium Chloride (NH_4Cl)	Carl Roth GmbH & Co.KG, Karlsruhe, Germany
Aprotinin	Sigma-Aldrich, St. Louis, MO, USA
β-Mercaptoethanol	Carl Roth GmbH & Co.KG, Karlsruhe, Germany
Bradford Protein Assay	Bio-Rad, Hercules, CA, USA
Bovine Serum Albumin (BSA)	Sigma-Aldrich, St. Louis, MO, USA

Calcium Chloride ($CaCl_2$)	Merck KGaA, Darmstadt, Germany
Cholesterol Assay	Roche, Basel, Switzerland
Concanavalin A from *Canavalia ensiformis*	Sigma-Aldrich, St. Louis, MO, USA
Crystal Mount™ Aqueous Mounting Medium	Sigma-Aldrich, St. Louis, MO, USA
Diethyl pyrocarbonate (DEPC) H_2O	Thermo Fisher Scientific, Waltham, MA, USA
Dimethyl Sulfoxide (DMSO)	Sigma-Aldrich, St. Louis, MO, USA
Dulbecco's Modified Eagle Medium (DMEM) + GlutaMAX™-I	Thermo Fisher Scientific, Waltham, MA, USA
Dulbecco's Phosphate Buffered Saline (DPBS)	Sigma-Aldrich, St. Louis, MO, USA
Ethylenediaminetetraacetic Acid (EDTA)	Carl Roth GmbH & Co.KG, Karlsruhe, Germany
Eosin G 0.5% solution	Carl Roth GmbH & Co.KG, Karlsruhe, Germany
Ethanol 100% pure	Th. Geyer GmbH & Co.KG, Renningen, Germany
Ethanol 70%	Th. Geyer GmbH & Co.KG, Renningen, Germany
Fetal Bovine/Calf Serum (FBS/FCS)	Thermo Fisher Scientific, Waltham, MA, USA
Glucose (D-)	Sigma-Aldrich, St. Louis, MO, USA
Glutamine (L-)	Sigma-Aldrich, St. Louis, MO, USA
Glycine	Carl Roth GmbH & Co.KG, Karlsruhe, Germany
Hemalum Solution Acid (Hematoxylin) acc. to Mayer	Carl Roth GmbH & Co.KG, Karlsruhe, Germany
Heparin Natrium (10.000 IU/ml)	B. Braun Melsungen AG, Melsungen, Germany
Horse Serum, inactivated	Thermo Fisher Scientific, Waltham, MA, USA
Hydrogen Chloride (HCl, 37%)	Carl Roth GmbH & Co.KG, Karlsruhe, Germany
Hydrogen Peroxide ($H_2O_{2)}$	Carl Roth GmbH & Co.KG, Karlsruhe, Germany
Ketamine (100mg/ml)	Albrecht GmbH, Aulendorf, Germany
Lipopolysaccharides (LPS) from *Salmonella abortus equi*	Sigma-Aldrich, St. Louis, MO, USA
Luminol Sodium Salt	Sigma-Aldrich, St. Louis, MO, USA
Magnesium Chloride ($MgCl_2$)	Merck KGaA, Darmstadt, Germany
Magnesium Sulfate ($MgSO_4$)	Merck KGaA, Darmstadt, Germany
Maxima SYBR Green	Thermo Fisher Scientific, Waltham, MA, USA
Methanol 100% pure	Th. Geyer GmbH & Co.KG, Renningen, Germany
NuPAGE™ LDS Sample Buffer	Thermo Fisher Scientific, Waltham, MA, USA
NuPAGE™ MES SDS Running Buffer	Thermo Fisher Scientific, Waltham, MA, USA
NuPAGE™ Sample Reducing Agent	Thermo Fisher Scientific, Waltham, MA, USA
Para-Formaldehyde (16%), EM Grade	Electron Microscopy Sciences, Hatfield, PA, USA
Para-hydroxy Coumaric Acid	Sigma-Aldrich, St. Louis, MO, USA
Penicillin (10.000IU/ml)/ Streptomycin (10.000µg/ml)	Thermo Fisher Scientific, Waltham, MA, USA
Percoll™ Centrifugation Medium	GE Healthcare, Chicago, IL, USA
Phenylmethylsulfonyl Fluoride	Sigma-Aldrich, St. Louis, MO, USA
PhosSTOP Phosphatase Inhibitor Tablets	Roche, Basel, Switzerland
Potassium Bicarbonate ($KHCO_3$)	Carl Roth GmbH & Co.KG, Karlsruhe, Germany
Potassium Chloride (KCl)	Sigma-Aldrich, St. Louis, MO, USA
Potassium Dihydrogenphosphage (KH_2PO4_4)	Carl Roth GmbH & Co.KG, Karlsruhe, Germany
Proteinase K	Carl Roth GmbH & Co.KG, Karlsruhe, Germany
Recombinant Murine IL-4	PeproTech Inc., Rocky Hill, NJ, USA

RNAse A (100mg/ml)	Qiagen, Venlo, Netherlands
Roswell Park Memorial Institute Medium (RPMI) 1640 + GlutaMAX^{TM}-I	Thermo Fisher Scientific, Waltham, MA, USA
Sodium Acide (NaN_3)	Carl Roth GmbH & Co.KG, Karlsruhe, Germany
Sodium Bicarbonate ($NaHCO_3$)	Carl Roth GmbH & Co.KG, Karlsruhe, Germany
Sodium Chloride (NaCl)	Sigma-Aldrich, St. Louis, MO, USA
Sodium Chloride (NaCl, 0.9%)	B. Braun Melsungen AG, Melsungen, Germany
Sodium Fluoride (NaF)	Sigma-Aldrich, St. Louis, MO, USA
Sodium Hydroxide (NaOH)	Carl Roth GmbH & Co.KG, Karlsruhe, Germany
Sodium Orthovanadate	Sigma-Aldrich, St. Louis, MO, USA
Sodium Pyrophosphate (Na_2HPO_4)	Carl Roth GmbH & Co.KG, Karlsruhe, Germany
Strep-Tactin® HRP	IBA Lifesciences, Göttingen, Germany
TEPP-46 (6-[(3-aminophenyl)methyl]-4,6-dihydro-4-methyl-2-(methylsulfinyl)-5H-thieno[2',3':4,5]pyrrolo[2,3-d]pyridazin-5-one)	Cayman Chemical, Ann Arbor, MI, USA
Triglyceride Assay	Roche, Basel, Switzerland
TRIS Hydrochloride (HCl)	Carl Roth GmbH & Co.KG, Karlsruhe, Germany
Triton^{TM} X-100	Sigma-Aldrich, St. Louis, MO, USA
Trypan Blue 0.4% (w/v)	Sigma-Aldrich, St. Louis, MO, USA
Tween® 20 (Polysorbat)	Thermo Fisher Scientific, Waltham, MA, USA
Xylazine (Rompun® 2%)	Bayer AG, Leverkusen, Germany
Xylene Substitute (HS200-5 XEM)	DiaTec, Bamberg, Germany

Table 4: Chemical reagents and kits.

2.1.5 Buffers and solutions

Buffer/Solution	**Chemical composition**
Electrochemiluminescence Solution	1.25mM Luminol / Tris HCl 15mM Para-hydroxy Coumaric Acid/DMSO 30% H_2O_2
Erythrocyte Lysis Buffer (ACK, 10×)	8.29g NH_4Cl (0.15M) 1g $KHCO_3$ (10mM) 37.2mg EDTA (0.1mM) ad 1l Deionized H_2O
FACS buffer	978ml PBS (1×) 2ml NaN_3 (0.02% w/v) 20ml FCS
Hank's Balanced Salt Solution (HBSS)	5.4mM KCl 0.3mM Na_2HPO_4× 7 H_2O 4.2mM $NaHCO_3$ 1.3mM $CaCl_2$ 0.5mM $MgCl_2$ × 6 H_2O 0.6mM $MgSO_4$ × 7 H_2O 137mM NaCl 5.6mM D-Glucose ad 1l Deionized H_2O

Lysis buffer for Western Blot	12.5ml TRIS (25mM) 75ml NaCl (150mM) 5ml EDTA (5mM) 100ml Glycerol (10%) 50ml Triton^{TM} X-100 (1%) 12.5ml Sodium Pyrophosphate (10mM) 10ml Sodium Orthovanadate (1mM) 5ml Glycerophosphate (10mM) ad 500ml Deionized H_2O
Murine Anaesthetic Solution	8% Rompun® (2%) 12% Ketamine (100mg/ml) 20% Heparin 5000 (IU/ml) 60% NaCl (isotonic)
Para-Formaldehyde Solution (PFA, 4%)	8 g Para-Formaldehyde 20ml PBS (10×) 10mM NaOH ad 200 ml Deionized H_2O
Phosphate Buffered Saline (PBS, 10×)	137.9mM NaCl 6.5mM Na_2HPO_4× 2 H_2O 1.5 mM KH_2PO_4 2.7mM KCl ad 1l Deionized H_2O
Percoll/HBSS	38% Percoll Working Solution 60% HBSS 2% Heparin (100IU/ml)
Percoll Working Solution	92.5ml Percoll Centrifugation Medium 7.2ml PBS (10×) 1.2ml $NaHCO_3$ 7.5& in Deionized H_2O
Proteinase K Buffer	1.212g Tris (100mM) 143mg EDTA (5mM) 1.17g NaCl (200mM) 200mg SDS (0.2%) Prepare freshly before usage: 90µl Proteinase K buffer + 10µ Proteinase K stock solution (20mg/ml)
RNAse A Buffer	121mg Tris (10mM) 29mg EDTA (1mM) 20µ RNAse A (100mg/ml)
Sodium Orthovanadate Solution	Sodium Orthovanadate (10mM) 150ml Deionized H_2O
Sodium Pervanadate Solution	100µl Sodium Orthovanadate Solution 16µl H_2O_2
Transfer buffer for Western Blot (10×)	250mM TRIS 2M Glycin ad 2l Deionized H_2O Transfer buffer (1×): 200ml Transfer buffer (10×) 400ml Methanol ad 2l Deionized H_2O

Tris-buffered Saline (TBS, 10×)	100mM TRIS 1.5M NaCl ad 2l Deionized H_2O
Tris-buffered Saline with Tween® 20 (TBS-T)	200ml TBS (10×) 2ml Tween® 20 ad 2l Deionized H_2O

Table 5: Chemical composition of buffers and solutions.

2.1.6 Antibodies

Primary					
Target	**Dilution**	**Host**	**Clone**	**Conjugate**	**Distributer**
β-Actin	1:1000	Goat	polyclonal	HRP	Santa Cruz Biotechnology Inc., Dallas, TX, USA
PKM2	1:1000	Rabbit	polyclonal	—	Cell Signalling Technology, Cambridge, U.K.
pPKM2 (Y105)	1:1000	Rabbit	polyclonal	—	Cell Signalling Technology, Cambridge, U.K.
Secondary					
Anti-rabbit IgG	1:5000	Goat	polyclonal	HRP	Cell Signalling Technology, Cambridge, U.K.
Anti-rabbit IgG	1:5000	Goat	polyclonal	HRP	Jackson Laboratories, Inc., West Grove, PA, USA

Table 6: Antibodies used for Western Blotting.

Primary					
Target	**Dilution**	**Host**	**Clone**	**Conjugate**	**Distributer**
Caspase 1	1:500	Hybridoma	Casper-1	—	Adipogen Life Sciences, San Diego, CA, USA
HMGB1	1:1000	Rabbit	polyclonal	—	Abcam, Cambridge, U.K.
MPO	1:40	Goat	polyclonal	—	R&D Systems Inc., Minneapolis, MN, USA
Secondary					
Anti-goat IgG	1:200	Rabbit	polyclonal	Biotin	Dako Denmark A/S, Glostrup, Denmark
Anti-mouse IgG	1:200	Rabbit	polyclonal	Biotin	Dako Denmark A/S, Glostrup, Denmark
Anti-rabbit IgG	1:500	Goat	polyclonal	Biotin	Jackson Laboratories, Inc., West Grove, PA, USA

Table 7: Antibodies used for immunohistochemical stainings.

Myeloid				
Target	**Dilution**	**Fluorophore**	**Clone**	**Distributer**
CCR2	1:200	BV711	475301	BD Biosciences, San Jose, CA, USA
CCR2	1:100	PE	475301	R&D Systems Inc., Minneapolis, MN, USA
CD11b	1:200	PE-Cy7	M1/70	BioLegend Inc., San Diego, CA, USA
CD16/32	1:100	—	93	BioLegend Inc., San Diego, CA, USA
CD39	1:200	AF647	DUHA59	BioLegend Inc., San Diego, CA, USA
CD206	1:200	BV711	CO68C2	BioLegend Inc., San Diego, CA, USA
CD206	1:200	FITC	MR5D3	BioLegend Inc., San Diego, CA, USA
CD301	1:100	PE	LOM-14	BioLegend Inc., San Diego, CA, USA
F4/80	1:100	APC	REA126	Miltenyi BioTec, Bergisch Gladbach, Germany
F4/80	1:100	FITC	REA126	Miltenyi BioTec, Bergisch Gladbach, Germany
Ly6C	1:200	PerCP	HK1.4	BioLegend Inc., San Diego, CA, USA
Ly6G	1:200	BV421	1A8	BioLegend Inc., San Diego, CA, USA
PD-L1	1:200	PE	M1H5	eBioscience Inc., San Diego, CA, USA
Zombie NIR	1:500	APC-Cy7	—	BioLegend Inc., San Diego, CA, USA
Lymphoid				
CD4	1:200	FITC	RM4-5	BioLegend Inc., San Diego, CA, USA
CD8	1:200	BV785	53-6.7	BioLegend Inc., San Diego, CA, USA
CD16/32	1:100	—	93	BioLegend Inc., San Diego, CA, USA
CD25	1:200	PE	P4-61	BioLegend Inc., San Diego, CA, USA
Foxp3	1:100	AF647	MF-14	BioLegend Inc., San Diego, CA, USA
PD1	1:200	PE-Cy7	J43	eBioscience Inc., San Diego, CA, USA
TIGIT	1:200	BV421	1G9	BioLegend Inc., San Diego, CA, USA
Zombie NIR	1:500	APC-Cy7	—	BioLegend Inc., San Diego, CA, USA

Table 8: Antibodies used for flow cytometry.

2.1.7 Oligonucleotide sequences

All primers were obtained from Metabion International AG, Planegg, Germany.

Target	Forward primer sequence Reverse primer sequence	Annealing Temp. (°C)	Extension time (s)	Reference
Actb	GGCATAGAGGTCTTTACGGATGTC TATTGGCAACGAGCGGTTCC	60	12	NM_007393
Arg1	TCACCTGAGCTTTGATGTCG CACCTCCTCTGCTGTCTTCC	60	12	NM_007482.3
Ccl2	TCCCAATGAGTAGGCTGGAG GCTGAAGACCTTAGGGCAGA	60	12	NM_011333.3
Cpt1α	CCAGGCTACAGTGGGACATT GAACTTGCCCATGTCCTTGT	60	12	NM_013495.2
Cyp7a1	CCTCTGGGCATCTCAAGCAA CGCAGAGCCTCCTTGATGAT	60	12	NM_007824.2
Fasn	CTGAAGAGCCTGGAAGATCG GTCACACACCTGGGAGAGGT	60	12	NM_007988.3
Hif1α	AGCTTCTGTTATGAGGCTCACC TGACTTGATGTTCATCGTCCTC	60	16	NM_010431
Il1β	GGGCCTCAAAGGAAAGAATC TACCAGTTGGGGAACTCTGC	60	12	NM_008316
Il6	GCCTATTGAAAATTTCCTCTG GTTTGCCGAGTAGATCTC	53	12	J03783
Il10	ATGCCTGGCTCAGCAC GTCCTGCATTAAGGAGTCG	58	16	NM_010548
Il23	GACTCAGCCAACTCCTCCAG GGCACTAAGGGCTCAGTCAG	60	12	NM_031252
Ldha	AAACCGAGTAATTGGAAGTGGTTG TCTGGGTTAAGAGACTTCAGGGAG	60	12	NM_001136069
Pkm1	GTCTGGAGAAACAGCCAAGG TCTTCAAACAGCAGACGGTG	60	12	NM_001253883.2
Pkm2	GTCTGGAGAAACAGCCAAGG CGGAGTTCCTCGAATAGCTG	60	12	NM_011099.4
Pparg	CCACAGTTGATTTCTCCAGCATTTC CAGGTTCTACTTTGATCGCACTTTG	60	12	NM_001127330.1
Slc2a1	CAGTTCGGCTATAACACTGGTG GCCCCCGACAGAGAAGATG	62	12	NM_011400
Socs1	GCCAACGGAACTGCTTCTTCG GAAGGAACTCAGGTAGTCACG	61	12	NM_009896
Srebf1	GAGATGTGCGAACTGGACAC CTCTCAGGAGAGTTGGCACC	60	12	NM_011480.4

Table 9: Run protocol conditions and oligonucleotide sequences for target-specific PCR.

2.1.8 Laboratory animals

C57BL/6J mice were bred by crossing *Pkm2*$^{fl/fl}$ mice (kind gift of Matthew G. vander Heiden, MD, PhD, Department of Medical Oncology, Dana-Farber Cancer Institute, Boston, MA, USA) and mice carrying a *Cre* recombinase downstream the myeloid specific *LysM* promotor (kind gift of Linda Diehl, PhD, Center for Experimental Medicine, Institute for Experimental Immunology and Hepatology, University Hospital Hamburg-Eppendorf, Germany) to achieve a myeloid-specific knockdown of PKM2. Details of the breeding strategy are outlined in Section 3.1.1 on page 30. All animal experiments were conducted according to the German Animal Protection Law and approved by the Institutional Review Board (G11/16, ORG 638, ORG 930, Behörde für Gesundheit und Verbraucherschutz, Hamburg, Germany). Mice received humane care according to the National Guideline of the National Institutes of Health, Hamburg, Germany. The animals were kept in individually ventilated cages under controlled conditions (22°C, 55% ambient humidity, 12-hour light/12-hour dark cycle) in groups of one to six individuals and received food and water *ad libitum*. For the experimental work, only male *Pkm2*$^{fl/fl}$ and *Pkm2*$^{\Delta myel}$ mice were used at the age of 10-15 weeks.

2.2 Methods

2.2.1 Extraction and storage of biological samples

Mice were anesthesized by intravenous injection of ketamine (120mg/kg), xylazine (16mg/kg) and heparin (8333 IU/kg) according to their body weight. 100µl of the anesthetic solution were injected per 10g body weight. The animals were subsequently weighed and then sacrificed by cervical dislocation before taking a blood sample by cardiac puncture. The blood samples were centrifuged for 5 minutes (20000g, 4°C) to retrieve the blood plasma. Plasma samples were stored at -20°C until further analyses.

Additionally, the liver was completely removed and weighed. Samples for mRNA and protein determination were frozen in liquid nitrogen before storing them at -80°C until further processing. For histological evaluations, the quadrate lobe was placed in 4% para-formaldehyde until dehydration and embedded in paraffin. Samples for flow cytometry were placed in HBSS and stored on ice for immediate processing. Spleens were removed in a similar manner and prepared equally.

For flow cytometric analyses of the bone marrow, both femura were removed and manually cleaned from adherent muscular and tendons, before placing them in HBSS on ice. Next, the bones were placed in a petri dish under a laminar flow hood and opened up with a scalpel on both ends. The bones were then placed upright in a perforated 0.2ml tube inside a 1.5ml tube and centrifuged for 10 seconds at 8000g. The inner tube and the empty bones were discarded, whereas the bone marrow was resuspended in HBSS and stored on ice until further processing.

2.2.2 Genotyping

In order to determine the genotype of the murine offspring, tissue samples were analyzed. Therefore, tail samples of the respective animals were broken down by 100µl of a lysis buffer containing proteinase K (2mg/ml) in a 1.5ml reaction tube. The reaction was incubated over night at 56°C. The next day, samples were heated to 95° for 10 minutes to inactivate the enzyme. Possible contaminations of RNA were eliminated by adding 750µl of RNAse A buffer per sample and incubation for 15 minutes. Next, a polymerase chain reaction was performed to amplify the specific parts of the DNA which had been altered by breeding (see section 3.1.1): The knock-in of two (homozygous) *loxP* sites in proximity to PKM2-specific exon 10 ($Pkm2^{fl/fl}$) and the heterozygous knock-in of the *Cre* recombinase downstream the *LysM* promotor ($LysM^{+/\Delta}$). In both cases, a Dream Taq Green Mastermix (Thermo Scientific) was used, which uses an include DNA polymerase and a loading dye for the gel electrophoresis of the PCR amplicons.

Component	$\boldsymbol{Pkm2^{fl/fl}}$	$\boldsymbol{LysM^{+}}$	$\boldsymbol{LysM^{\Delta}}$
H_2O (µl)	10	10	10
Forward primer (µl)	0.5	0.6	1.2
Reverse primer (µl)	0.5	1.2	0.6
DreamTaq MM (µl)	12.5	12.5	12.5
DNA (µl)	3	3	3
Total (µl)	26.5	27.3	27.3

Table 10: Master mix components for the genotyping PCR.

The components of the respective mastermix per sample are listed in table 10. The tubes were placed in a FlexCycler PCR Thermo Cycler (Analytik Jena, Jena, Germany) and the cycler protocol was run as shown in table 11 with 35 cycles of denaturation, annealing and elongation. To determine the heterozygous knock-in of a *Cre* recombinase downstream the *LysM* promotor, two mastermixes had to be prepared in order to amplify both the wildtype allele (320 bp) and the *Cre* knock-in allele (650 bp). Since two different pairs of primers were used, two different PCR protocols had to be run (see table 11, 35 cycles).

Target	**Initiation**	**Denaturation**	**Annealing**	**Extension**	**Final extension**
$Pkm2^{fl/fl}$	94°C	94°C	64°C	72°C	72°C
	5 min	30 sec	30 sec	1.5 min	5 min
$LysM^{+}$	94°C	94°C	63°C	72°C	72°C
	3 min	30 sec	1 min	1 min	2 min
$LysM^{\Delta}$	94°C	94°C	58°C	72°C	72°C
	3 min	30 sec	1min	1 min	2 min

Table 11: Cycler protocols for the genotyping PCR.

After amplification, the samples were loaded into the wells of a agarose gel with a 1kbp DNA ladder (Generuler, Thermo Scientific). Electrophoresis was performed using a

PowerPac® 200 power supply with 150V for 45 minutes. Visualization of the bands was performed with a Molecular Imager® VersaDoc™ 4000 MP Imaging System as described in section 2.2.10. Detailed results of the genotyping are shown in section 3.1.1 and in Figure 4.

2.2.3 Experimental animal treatment

Concanavalin A (ConA, 5mg/kg in Dulbecco's phosphate buffered saline (DPBS), both obtained from Sigma-Aldrich, Munich, Germany) or pure DPBS were administered intravenously (i.v.) into $Pkm2^{fl/fl}$ and $Pkm2^{\Delta myel}$ mice. Preparation of 6-[(3-aminophenyl)methyl]-4,6-dihydro-4-methyl-2(methyl)-sulfinyl-5H-thieno [2',3':4,5]-pyrrolo-[2,3-d]pyri-dazin-5-one (TEPP-46, Cayman Chemical, Ann Arbor, MI, USA) was performed by dissolving 40% w/v 2-Hydroxy-Propyl-β-Cyclodextrin (Sigma-Aldrich, Munich, Germany) in sterile filtered deionized H_2O, before adding 5mg TEPP-46 to 500µl of the vehicle substance. The respective mice received a dose of 50mg/kg intraperitoneally (i.p.) one hour prior to ConA injection. Mice were euthanized 8 hours after ConA injection as described in section 2.2.1.

2.2.4 Measurement of liver enzyme activity, cholesterol and triglycerides

Plasma samples were diluted 1:5 with deionized H_2O before measurement. A COBAS Integra 400 plus (Roche, Basel, Switzerland) was used to determine plasma activites of alanine aminotransferase (ALT) and plasma concentrations of total cholesterol and triglycerides.

2.2.5 Measurement of acyl carnitines

Determination of acyl carnitine concentrations in the sera of $Pkm2^{fl/fl}$ and $Pkm2^{\Delta myel}$ mice was performed by Dr. Barbara Finckh (Institute of Clinical Chemistry and Laboratory Medicine, University Hospital Hamburg-Eppendorf, Germany), who generously provided the data shown in Figure 14.

2.2.6 Measurement of PKM isoforms

PKM1 and PKM2 isoform distribution in BMDM was measured and kindly provided by Benjamin Dreyer, M. Sc. (Institute of Clinical Chemistry and Laboratory Medicine, University Hospital Hamburg-Eppendorf, Germany), using the method of Liquid chromatography–mass spectrometry (LC-MS) and an Ultrahigh Field Orbitrap Mass analyzer (ThermoFisher Scientific). Data from this measurement are shown as relative abundance of unique peptides for the respective target protein.

2.2.7 RNA isolation and transcription to cDNA

For the extraction of RNA from BMDM or whole liver tissue, the NucleoSpin RNA Kit® (Macherey & Nagel, Düren, Germany) was used. For BMDM, the cells were harvested

as described in section 2.2.12 and washed once with PBS before RNA extraction. 350µl Lysis Buffer RA1 and 3.5µl β-mercaptoethanol were mixed and applied to each sample before thorough aspiration and irrigation of the pellet in order to dissolve the cells. Whole liver tissue was prepared by placing the sample in a 2ml reaction tube with metal beads and the Lysis Buffer mentioned above before fragmenting the tissue using a TissueLyser II® (Qiagen, Venlo, Netherlands) for 2 minutes at a frequency of 30 Hz. In case of whole liver tissue, the suspension was filtered through a NucleoSpin® Filter and centrifuged for 1 minute at room temperature with 11000g. The following steps were performed identically for BMDM and whole liver tissue. The suspension was transferred into a 1.5ml reaction tube and 350µl ethanol (70% in DEPG) were added to induce precipitation of the RNA. 700µl of the mixture were loaded to a NucleoSpin® RNA Column containing a silica membrane before centrifugation for 1 minute with 11000g at room temperature. 350µl Membrane Desalting Buffer were loaded to the columns, which where centrifuged again in an equal manner. In order to eliminate any contamination by DNA, a mastermix was prepared, containing 10µl of reconstituted rDNAse and 90µl Reaction Buffer for rDNAse per specimen. 95µl of the reaction mixture were applied to the column and incubated for 15 minutes at room temperature. To inactivate the rDNAse, 200µl RAW2 Buffer were applied to the column, followed by another identical centrifugation step. Next, the column was washed with 600µl and 250µ RA3 Buffer before another centrifugation step (2 minutes, 11000g, room temperature). The columns and membranes were transferred onto new, RNAse-free reaction tubes. 30µl RNAse-free H_2O were applied to each membrane in order to elute the RNA. The columns and tubes were centrifuged for 1 minute with 11000g at room temperature, before discarding the columns and placing the tubes containing the RNA on ice immediately. The samples were stored at -80°C until usage.

The RNA was transcribed to cDNA using the Verso cDNA synthesis Kit (ThermoFisher Scientific) and a MyCycler™ Thermal Cycler System (Bio-Rad). The amount of RNA was quantified with a NanoDrop 3300 Fluorospectrometer (Thermo Fisher Scientific). After determination of the RNA yield in the samples, the volume of the RNA sample that equalled 1µg of RNA was mixed with 1µl of oligo(dT) nucleotides and a random hexamer mix and was made up to a total of 11µl with RNAse-free H_2O. The mix was placed in the cycler and incubated for 10 minutes at 70°C. Afterwards, the samples were stored on ice and a mastermix consisting of cDNA buffer (4µl per sample), deoxynucleotide triphosphates (dNTP, 2µl per sample), a reverse transcriptase enhancer (1µl per sample) and the reverse transcriptase itself (1µl per sample) was prepared. 8µl of the mastermix were given to each tube before continuing the cycler protocol for 1 hour at 42°C and subsequently for 5 minutes at 95°C to inactivate the reverse transcriptase. After transcription, the cDNA was either stored at 4°C for prompt analyses or stored at -20°C.

2.2.8 Quantitative real-time PCR

The method of real-time polymerase chain reaction was used to analyze the genetic transcription of genes of interest involved in inflammation, cellular communication, chemotaxis and metabolism. For this purpose, cDNA generated as described in section 2.2.7 was either used undiluted (in case of cytokines or transcription factors) or diluted 1:10 in RNAse-free H_2O. A mastermix of 10µl per specimen was prepared containing 5µl Maxima^{TM} SYBR Green, 2.6µl RNAse-free H_2O, 0.7µl of each of the diluted forward and reverse primer, as well as 1µl of the cDNA sample. The mastermix was distributed among the wells of a 96-well plate and inserted into the CFX96 Real-time PCR Cycler. A control specimen containing H_2O was used to rule out contamination of the plate. The running conditions for each primer set are listed in table 9 on page 14. Accuracy of the measurements was achieved by analyses of the melting curve, ensuring the exclusion of PCR data caused by unwanted amplicons.

Data for mRNA levels are shown as fold changes to the control group using the ΔΔCT method. If values from more than one independent experiment were compared, mRNA levels are shown as $2^{-\Delta CT}$ values in order to provide comparability between the experiments.

2.2.9 Extraction of protein lysates from cells and tissues

In order to perform Western Blot analyses from BMDM or whole liver tissue, the cells in question were split up using a lysis buffer (see section 5). For measurements which included the analyses of quarternary protein structures, cells were subjected to 1% para-formaldehyde in PBS for 7 minutes with gentle shaking prior to cell lysis to preserve the bond between protein oligomers for the subsequent gel electrophoreses and blotting procedures. Protein lysates from whole liver tissue were extracted by combining mechanical fractionation and chemical lysis. First, 1% 0.1M phenylmethylsulfonyl fluoride (PMSF), 1% aprotinin (Sigma-Aldrich), 0.2% sodium pervanadate solution and 1% sodium fluoride were added to the lysis buffer. For samples that were later analyzed for phosphorylated proteins, PhosSTOP (Roche Diagnostics) was used in order to protect the biological sample from dephosphorylation. A sample of pure lysis buffer per experiment was kept with its corresponding samples to ensure the accurate determination of protein yields when performing the Bradford assay (see section 2.2.10).

400µl of the (supplemented) lysis buffer were added to a sample of whole liver tissue in a 2ml reaction tube, before adding metal beads and fragmenting the tissue using a TissueLyser II® (Qiagen, Venlo, Netherlands) for 2 minutes at a frequency of 30 Hz. Afterwards, the samples were transferred to ice cold tubes and left to incubate for 10 minutes before vortexing. After three sessions of incubation and vortexing, the samples were centrifuged for 5 minutes at 5000rpm and 4°C before transferring them again into fresh, ice cold reaction tubes, leaving behind a visible smear in the previously used tube. The samples were centrifuged again for 10 minutes with 12700rpm at 4°C before storing them in aliquots of 50µl at -80°C until usage.

Lysates from BMDM were extracted by adding 150-300µl of the lysis buffer to the cell pellet after centrifugation. The pellet was dissolved in the lysis buffer by manual aspiration and irrigation in the reaction tube. Next, the sample was incubated for 10 minutes on ice before shaking it for 20 seconds using a vortex shaker (Heidolph). This cycle of incubation and shaking was repeated twice, before centrifuging the sample for 5 minutes at 4°C with 5000rpm and transferring the lysate into new, ice cold 1.5ml reaction tubes, thereby purifying the lysate. The samples were centrifuged again for 10 minutes at 4°C with 12700 rpm and subsequently transferred into new, pre-cooled reaction tubes in aliquots of 50µl. The lysates were stored at -80°C until usage.

2.2.10 Gel electrophoresis and Western Blot analyses

To determine the protein yield of cell or tissue lysates, a Bradford protein assay (Bio-Rad) was used. The Protein Assay Dye Reagent Concentrate was diluted 1:5 with deionized H_2O as a Bradford working solution. The lysates were diluted depending on their expected protein density from 1:5 to 1:20 with deionized H_2O and the diluted samples were then diluted again 1:100 with the Bradford working solution in a 96 well plate. The protein yield in the samples was assessed by 15 seconds of shaking and the ensuing spectroscopic analysis by a TECAN Infinite® 200 PRO multireader (TECAN Trading AG, Switzerland). Quantification of the protein content was calculated to determine the amount of protein loaded onto the gel. 15-30µg of protein were used, depending on the expected content of the protein in question. The wells were loaded with 20µl of NuPAGE® LDS Sample Buffer 4× (5µl), NuPAGE® Reducing Agent (2µl) and deionized H_2O (depending of the volume of protein lysate needed for the desired amount of protein, ad 20µl). To be able to estimate the size of the protein bands later in the procedure, a Precision Plus Protein Western Standard™ (Bio-Rad) was added to the first pouch of the gel. For the electrophoresis, NuPAGE® 15-well 4-12% Bis-Tris Mini Gels (Thermo Fisher Scientific) and the corresponding SDS running buffer (1:20 in deionized H_2O) were used in accordance with the manufacturer's instructions. Electrophoresis was powered by a PowerEase500 power supply (Thermo Fisher Scientific) and performed with 200V constantly for 35 to 60 minutes, depending on the size of the target protein. Afterwards, the blotting procedure was performed employing the wet-blot method (Mini Trans-Blot® Cell System and PowerPac™ HC power supply, all Bio-Rad) on a nitrocellulose membrane in a Western Blot Transfer Buffer. Next, the membrane was incubated with 5% non-fat dry milk powder (Bio-Rad) in TBS-T for 1 hour to avoid unspecific antibody binding before incubating the membrane with the primary antibody over night at 4° with gentle shaking. For a detailed list of antibodies and preparatory specifications see section 6 on page 12.

The following day, the membrane was washed three times in TBS-T for 10 minutes each and the marker bands were cut from the membrane before adding the second antibody and incubation for 1 hour at room temperature. To make the marker bands detectable, Strep-Tactin® HRP (IBA Lifesciences, Göttingen, Germany) was applied to

the marker band in a dilution of 1:10.000 in TBS-T and incubated simultaneously with the membrane for 1 hour. The membrane was then washed again three times before visualization. Therefore, an electrochemo-luminescence (ECL) solution, consisting of 0.00025% Luminol (Sigma-Aldrich) in 0.1M Tris/HCl ("Solution A") and 0.0011% para-hydroxy coumaric acid in dimethyl sulfoxide (DMSO, "Solution B"), was prepared. 3ml of A and 30µl of B were mixed immediately before the visualization procedure and 1.5µl of H_2O_2 were added to activate the ECL reaction. The activated ECL solution was then applied to the membrane; detection was performed using a Molecular Imager® Versa Doc™ MP Imaging System (Bio-Rad). After detection, the band intensity was quantified using the ImageLab 2.0 Software for Western Blot analyses (Bio-Rad).

2.2.11 Histological stainings

Liver samples were fixed in 4% para-formaldehyde and subsequently dehydrated before embedding them in paraffin.

Hematoxylin & Eosin staining. H&E stainings of liver sections were kindly provided by Tobias Gosau (Institute of Anatomy and Experimental Morphology, Center for Experimental Medicine, University Hospital Hamburg-Eppendorf, Germany). Liver sections of 3µm were cut and stained according to a standard H&E protocol.

Immunohistochemical stainings. Liver sections were de-paraffinized in xylene substitute (HS200-5 XEM) for 20 minutes before rehydrating them in a series of baths containing descending percentages of ethanol (5 minutes each in 100, 90, 70 and 50% ethanol). Then, the sections were rinsed thoroughly with H_2O and retrieved using a citrate-based retrieval solution (Target Retrieval Solution, DAKO, Glostrup, Denmark) in a dilution of 1:10 in deionized H_2O at 100°C for 10 minutes. After cooling, the samples were rinsed with H_2O and washed with TBS-T. Next, the sections were incubated with a solution of 10% Normal Swine Serum (Agilent/DAKO, Glostrup, Denmark) in a special Antibody Diluent (Agilent/DAKO, Glostrup, Denmark) for 45 minutes to avoid unspecific antibody binding. Afterwards, 50µl of the solution containing the primary antibody were applied to each liver section in Antibody Diluent (DAKO, Glostrup, Denmark) and incubated in the dark at 4°C over night. The next day, the sections were washed twice in TBS-T (TBS + 0.1% Tween® 20), before applying the biotinylated secondary antibody and incubating them for 30 minutes. The slides were washed again and incubated with a HRP-conjugated Streptavidin (Vectastain Elite ABC HRP Kit, Vectorlabs, Burlingame, CA, USA) for 30 minutes in the dark. Detection was performed by applying 3,3'-diaminobenzidine substrate buffer (BioLegend, San Diego, CA, USA) to the slides for 5 minutes before rinsing them with H_2O and counterstaining them with Hematoxylin for 1 minute. Lastly, the slides were mounted with Crystal Mount™ Aqueous Mounting Medium (Sigma, Saint-Louis, MO, USA) and let dry for 1 hour before covering them with Entellan® (Sigma-Aldrich) and cover slips.

2.2.12 Generation and maturation of BMDM

Bone marrow was extracted as described in 2.2.1. For the cell culture experiments, the pellet was resuspended in Roswell Park Memorial Institute Medium 1640 + GlutaMAX^{TM}-I (RPMI, Thermo Fisher Scientific) instead of HBSS and supplemented with 30% L929 supernatant (see section 2.2.13), 10% inactivated fetal bovine serum (Thermo Fisher Scientific), 5% inactivated horse serum (Thermo Fisher Scientific) and 1% Penicillin (104Units/ml) / Streptomycin (10mg/ml). Bone marrow cells were counted using a Neubauer Hemocytometer and cultured in 10cm cell culture dishes (Sarstedt, ASDF) at a count of 4×10^6 cells per dish and given 10ml of the growth medium. Macrophages were maturated for six days through replacement of the M-CSF containing medium depending on the color of its indicator dye, usually on day 3 - 4 after extraction. On day 6, maturity was verified by microscopic evaluation, before stimulating the cells as mentioned below.

Stimulation experiments were performed by supplementation of the fresh RPMI medium (including 10% inactivated fetal bovine serum, 5% inactivated horse serum and 1% Penicillin (104Units/ml) / Streptomycin (10mg/ml)) with the respective stimulants. BMDM were treated with LPS from *Salmonella abortus equi* (100ng/ml, Sigma-Aldrich), TEPP-46 (100µM, Cayman Chemical, Ann Arbor, MI, USA) or murine recombinant IL-4 (PeproTech, Rocky Hill, NJ, USA) at a concentration of 20ng/ml for varying time periods indicated in the description of the respective experiments. For the examination of metabolic parameters as shown in Figure 11 on page 40, BMDM were stimulated as stated in table 12. Cells were harvested by incubation with Trypsin/ethylenediaminetetraacetic acid (EDTA) in a dilution of 1:10 in PBS for 1 minute at 37°C. Remaining adherent cells were harvested using a cell scraper (Sarstedt).

2.2.13 Extraction of L929 supernatant for BMDM differentiation

To produce the macrophage growth medium described in section 2.2.12, a L929 fibroblast cell line was used (NCTC clone 929, No. CCL-1, LGC Standards, Wesel, Germany). The cells were grown in T175 cell culture flasks (Sarstedt, Nümbrecht, Germany) and given Dulbecco's Modified Eagle Medium + GlutaMAX^{TM}-I (DMEM, Thermo Fisher Scientific, Waltham, MA, USA), supplemented with 5% inactivated fetal bovine serum (Thermo Fisher Scientific), 2% L-Glutamine and 1% Penicillin (104U/ml) / Streptomycin (10mg/ml) and were cultivated for seven days before collecting the supernatant, which contained macrophage colony-stimulating factor (M-CSF). The supernatant was filtered using a Stericup-GP® Sterile Vacuum Filtration System (Merck KGaA, Darmstadt, Germany), separated into aliquots of 50ml and stored in 50ml reaction tubes (Sarstedt, Nümbrecht, Germany) at -20°C until usage.

2.2.14 Bead-based immunoassay of cytokine concentrations

For the analyses of cytokine concentrations in the supernatants of cultured BMDM, a custom made, bead-based immunoassay (LEGENDplex^{TM} Custom Panel) was performed

according to manufacturer's instructions. For the present study CCl2, CCl22, IL-10 and TNFα were measured. The basic principle of the assay equals a sandwich enzyme-linked immunosorbent assay (ELISA), but uses a flow cytometer to read out the cytokine concentrations. 6.25µl of the respective specimen (cell culture supernatants and a series of standard solutions in the assay buffer) were mixed on a vortex shaker for 20s with 6.25µl of an assay buffer and 6.25µl of a solution containing capture beads in a v-bottom 96-well plate before incubation in the dark at 4°C overnight on a plate shaker. On the day of the assay, the plate was vortexed again before adding the biotinylated detection antibody and centrifuging it for 1 minute at room temperature with 1000g. The wells were then mixed repeatedly by manual resuspension and the plate was incubated a second time for two hours at room temperature on a plate shaker. Finally, 6.25 µl of Streptavidin-Phycoerythrin were added to each well (which binds to the biotinylated detection antibody), before centifuging the plate again (room temperature, 1000g, 1 minute) and subsequent manual resuspension. A final incubation step (30 minutes at room temperature in the dark) ensured sufficient binding between the antibody and the flourescent conjugate. The preparation was completed by three consecutive washing steps with 200µl of a special washing buffer included in the assay kit, followed by a centrifugation step (1000g, 5 minutes at room temperature) before transferring the supernatants into tubes suitable for flow cytometry. The supernatants were analyzed by recording 4000 events in the bead gate using a BD FACSCanto^{TM} II flow cytometer. During the measurement, the conjugate emitted a flourescence signal which was proportional to the concentration of the respective cytokine/compound in the supernatant. The data were converted into concentration levels in pg/ml by the LEGENDplex^{TM} Data Analysis Software.

2.2.15 Metabolic measurements, Mito Stress Assay

In order to assess the metabolic properties of BMDM derived froem *Pkm2*$^{fl/fl}$ and *Pkm2*$^{\Delta myel}$ mice, an Agilent Seahorse XF Cell Mito Stress Test was performed. Briefly, this plate-based assay allows to draw conclusions about mitochondrial function of the cultured cells and their intracellular distribution of metabolic intermediates in real time. This is achieved by measuring the amount of O_2 consumed by the cells over time (hereinafter called the "oxygen consumption rate", OCR, pmol/min), as well as the efflux of intracellular protons into the extracellular space ("extracellular acidification rate", ECAR, mpH/min), the latter of which is basically an indicator for the glycolytic flux. Over the course of the assay, various modulators are injected into the wells to interfere with different components of the electron transport chain, which (apart from basal respiration and acidification) permits the determination of the maximum respiratory capacity, the proportion of respiration attributable to ATP synthesis or proton leakage of the analyzed cells.

For the analyses, BMDM were extracted and differentiated as described in section 2.2.12. In this case, stimulation of the cells prior to the assay was achieved by

supplementation of the cell culture medium as indicated in table 12.

Stimulant	**Concentration**	**Stimulation time**
Untreated	—	24 hours
LPS	100ng/ml	2 hours
LPS	100ng/ml	24 hours
LPS/ ATP	100ng/ml 200mM	2 hours
TEPP-46	µM	2 hours

Table 12: Cell culture stimulation conditions prior to the Cell Mito Stress Test.

On the day prior to the assay, the Seahorse XFe96 Analyzer was started and preheated over night. To allow the adherent BMDM to rest and settle, the cells were transferred into the assay plate on the day before the assay. Therefore, 5×10^4 BMDM in 80µl cell culture medium were seeded into the wells of an Agilent Seahorse 96-well XF Cell Culture Microplate while leaving out the background correction wells on each corner of the plate. These wells were given 80µl of pure medium. The plate was incubated at 37°C with 5% CO_2 overnight; the designated wells were stimulated with LPS (100ng/ml for 24 hours). Next, the sensor cartridge was hydrated by submerging each sensor in 200µl of sterile deionized H_2O and placed in a non-CO_2 incubator until the next day, as was a 20ml aliquot of the XF Calibrant. The last step of preparation included the design of the Mito Stress Assay using the Seahorse Wave Desktop Software as shown in table 13.

Modulator	**Concentration**	**Mixing time**	**Measurement time**	**Measurement points**
Precalibrate	—	3 min	3 min	3
Oligomycin	3µM	3 min	3 min	3
FCCP	3µM	3 min	3 min	3
Antimycin A/ Rotenone	1µM 1µM	3 min	3 min	3

Table 13: Cell Mito Stress Test run protocol.

The next day, the assay cartridge was prepared by discarding the H_2O from the utility plate and filling its wells with 200µl of the XF Calibrant Solution which was incubated overnight. Afterwards, the sensor cartridge was immersed into the filled wells of the utility plate and incubated for 1 hour at 37°C in a non-CO_2 incubator. In order to provide for accurate measurement of the metabolic parameters, the XF Assay Medium was heated to 37°C in a water bath, adjusted to a pH of 7.4 by the addition of NaOH and supplemented with L-glutamine (2mM), pyruvate (1mM) and glucose (10mM).

The cells which had not yet been stimulated were given their respective stimulatory medium (see table 12). During the stimulation time, the electron transport chain modulators (oligomycin, FCCP and antimycin A/rotenone) were diluted, warmed and adjusted to pH 7.4. After 2 hours, the medium was discarded and the cells were washed

with 100µl Assay Medium in the plate. 180µl of fresh medium were added to each well before storing the plate in an incubator at 37°C, this time without CO_2. Finally, the sensor cartridge was loaded with 20-30µl of the prepared modulatory solutions into the designated injection ports.

All ports were inspected for even loading. The the sensor cartridge and the utility plate were inserted into the preheated Seahorse XFe96 Analyzer for 30 minutes of calibration. Afterwards, the cell plate was loaded and equilibrated with the Seahorse XFe96 Analyzer before the Mito Stress Test was run.

2.2.16 Extraction and preparation of leukocytes for flow cytometry

The organ samples were extracted after euthanizing the mice as described in section 2.2.1. For the isolation of hepatic non-parenchymal cells (NPC), livers were crushed in a cell culture dish using a syringe plunger and filtered through a 100µm nylon filter (Corning Inc., Corning, NY, USA) into a 50ml reaction tube to separate the cells. The suspension was supplemented with HBSS and centrifuged for 5 minutes at room temperature with 500g. The HBSS supernatant was discarded, whereas the cell pellet was resuspended in 10ml Percoll/HBSS before transferring the suspension into a 15ml reaction tube. For the gradient, the suspension was centrifuged for 20 minutes at room temperature with 800g. Next, the supernatant and cellular debris were discarded and the pellet was dissolved in 2ml of lysis buffer to remove erythrocytes from the total of NPC. After 2 minutes of incubation at room temperature, the reaction was stopped by adding 18ml HBSS, before centrifuging the suspension again for 5 minutes at 4°C with 500g. The supernatant was discarded and the remaining pellet was resuspended and mixed with HBSS, before distributing the cell suspension into tubes for flow cytometry.

Splenocytes were isolated by crushing the organs through a 100µm nylon filter into a 50ml reaction tube and adding 15ml of cold HBSS (4°C). Afterwards, the suspension was centrifuged for 5 minutes at 4°C with 500g. The supernatant was discarded and the pellet was purified by adding lysis buffer as described. After stopping the reaction and another identical step of centrifuging, the supernatant was discarded and the pellet was dissolved in 10ml of cold HBSS. The cellular concentration of the suspension was counted using a Neubauer Hemocytometer and adjusted to a count of 1×10^6 with HBSS, before splitting the cells into tubes for flow cytometry.

Bone marrow cells were extracted as outlined in section 2.2.1. The cell suspension was treated as described for the isolation of splenocytes and finally transferred into tubes for flow cytometry.

2.2.17 Flow cytometric analyses

In order to differentiate populations and subpopulations of myeloid (and lymphoid) cells, flow cytometric analyses of BMDM as well as *ex vivo* hepatic, splenic and bone marrow leukocytes were performed. All gates were set using unstained control samples or fluorescence minus one (FMO) samples.

Preparation, staining and gating strategy of BMDM. For the analyses of BMDM, cells were cultured, differentiated, stimulated and harvested as described in section 2.2.12 (page 22). Afterwards, cells were transferred into tubes for flow cytometry and washed twice with 500µl PBS per sample and centrifuged for 5 minutes at 4°C with 500g. The supernatant was discarded and the cells were incubated for 15 minutes with an anti-CD16/32 antibody to prevent unspecific binding to F_c receptors. Next, the cells were washed with PBS and centrifuged again for 5 minutes at 4°C with 500g before incubating them for 30 minutes at 4°C in the dark with 50µl of the the antibody mastermix (see Table 8 for details). After staining, the cells were washed and centrifuged again as described before fixation by adding 200µl of 4% para-formaldehyde in PBS to each tube and immediate mixing on a vortex shaker. The samples were incubated for 15 minutes at 4°C in the dark. Next, the tubes were washed and centrifuged again and the supernatant was discarded. The cells were given 200µl of FACS buffer before covering them with Parafilm M® and storing them in the fridge until measurement. The gating

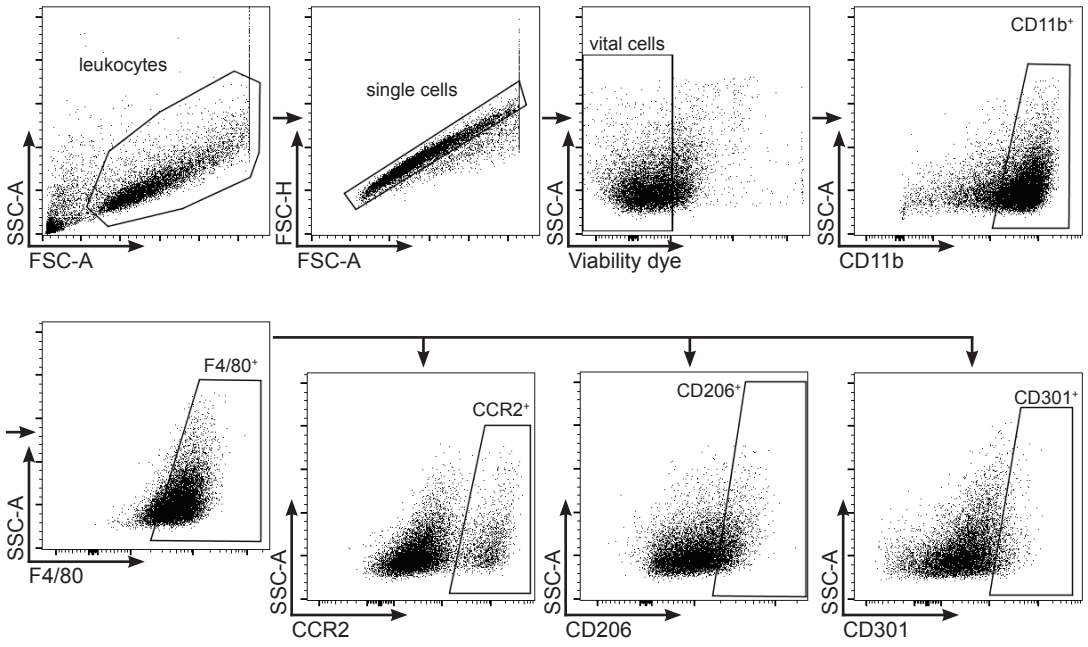

Figure 1: Representative dot plots of the gating strategy for BMDM in flow cytometric analyses. BMDM were prepared as described and analyzed by flow cytometry for myeloid purity (CD11b, F4/80), polarization markers (CD206, CD301) and the chemokine receptor CCR2.

strategy for the identification of myeloid subsets is depicted in Figure 1. To exclude damaged cells and other debris from the analysis, leukocytes were gated as shown in the first gate according to size (forward scatter area, FSC-A) and granularity (sideward scatter area, SSC-A). Next, cell aggregates were excluded by plotting height and area of the forward scatter and gating single cells as shown. Dead cells were eliminated from the measurement as they are prone to binding to various reagents in a non-specific manner. Therefore, a viability dye was included in the antibody cocktail which was only taken

up by non-vital cells. Cells who did not emit a signal were considered vital and thus included in the analysis. Vital, single cells were then gated for CD11b, a pan-myeloid marker, and F4/80, a marker of mature macrophages, to verify the purity of the cell culture (see section 3.2.1 and Figure 7). $CD11b^{+}F4/80^{+}$ cells were further analyzed for the chemokine receptor CCR2 and the M2 polarization markers CD206 and CD301.

Preparation, staining and gating strategy of *ex vivo* leukocytes. Leukocytes were isolated from the bone marrow, spleens and livers of $Pkm2^{fl/fl}$ and $Pkm2^{\Delta myel}$ mice as described in detail in section 2.2.16.

For the staining of extracellular markers, isolated cells were incubated in flow cytometry tubes with 50µl of the antibody mastermix including an anti-CD16/32 antibody against unspecific binding and a viability dye for 30 minutes at 4°C in the dark. The samples were washed with cold PBS and centrifuged as previously described. After discarding the supernatant, cells were resuspended in 200µl cold FACS buffer and stored covered with Parafilm M® at 4°C in the dark until the analysis. For the

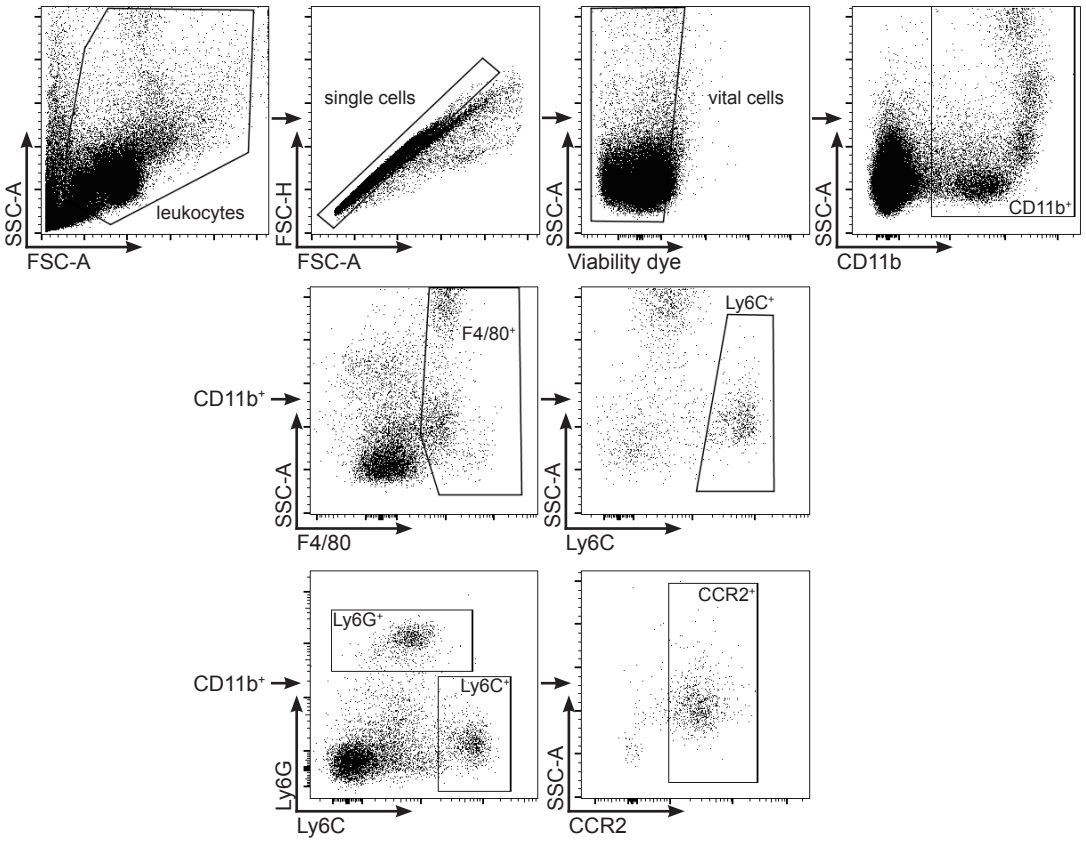

Figure 2: Representative dot plots of the gating strategy for myeloid NPC. Vital single cells were gated for the pan-myeloid marker CD11b and screened for the expression of the macrophage marker F4/80, Ly6C for monocytes and Ly6G for neutrophilic granulocytes. Monocytes were gated for the chemokine receptor CCR2.

evaluation of lymphoid cells, the respective samples were also stained intracellularly for the master transcription factor of regulator T cells, Foxp3. Therefore, a Foxp3

Transcription Factor Staining Buffer Set (eBioscience^{TM}) was used. In order to achieve a sufficient fixation and permeabilization of the cells, a Fix/Perm Buffer was prepared (Fixation/Permeabilization Concentrate in Permeabilization Diluent, 1:4). 150µl were added to each sample and mixed manually with the cell suspension. After 35 minutes of incubation at 4°C in the dark, cell samples were washed twice by adding 200µl of a wash buffer supplied by the manufacturer (Permeabilization Buffer, 1:10 in deionized H_2O) and centrifuging the samples for 5 minutes at 4°C with 500g. After pouring away the supernatant, the antibody mastermix was added to the tubes (25µl, 1:100 in the wash buffer) and mixed thoroughly with the cells before another equal similar of incubation. Next, the tubes were centrifuged as described and washed twice with the wash buffer. Lastly, the cells were mixed with 200µl of FACS buffer, covered with Parafilm M® and stored in the fridge until measurement. With regard to leukocytes of the myeloid

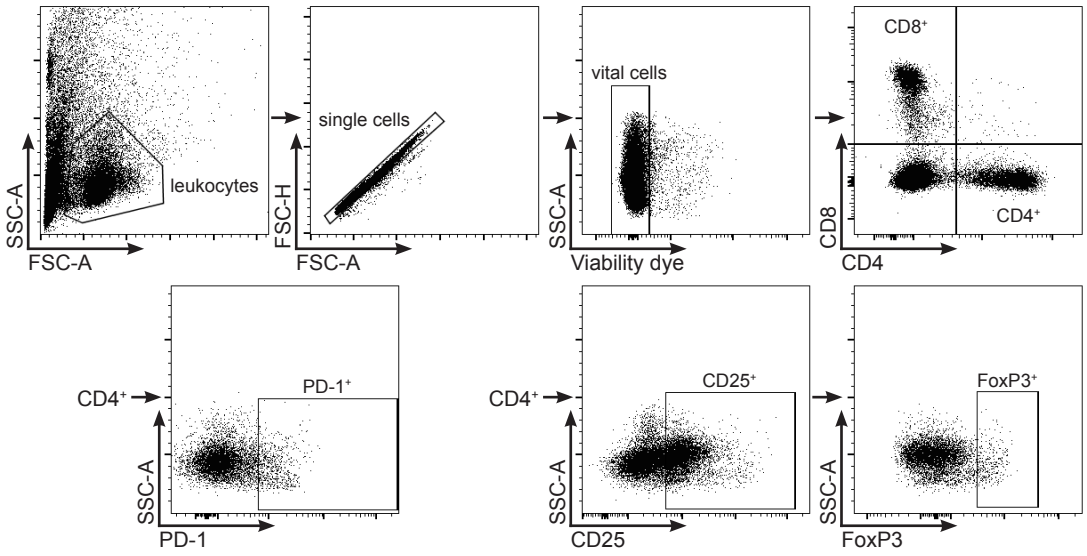

Figure 3: Representative dot plots of the gating strategy for lymphoid NPC. Vital single cells were gated for CD8 and CD4, the latter of which were analyzed for the coinhibitory marker PD-1, the activation marker CD25 and Foxp3, the master transcription factor of regulatory T cells.

lineage, cells were were analyzed for cell size (FSC-A) and granularity (SSC-A) as illustrated in Figure 2. Cell aggregates and dead cells were excluded as mentioned. To identify myeloid cells in the bone marrow, spleen and liver, the pan-myeloid marker CD11b was employed. To screen the samples for resident macrophages, $CD11b^+$ cells were gated for F4/80. A fraction of these cells was also positive for the monocyte marker Ly6C. Additionally, myeloid cells were gated for Ly6G, a marker emblematic for neutrophilic granulocytes, and Ly6C without prior inclusion of F4/80. These $Ly6C^+$ $Ly6G^-$ monocytes were ancillarily analyzed for CCR2 (see also Figure 1).

Secondly, lymphoid cells of $Pkm2^{fl/fl}$ and $Pkm2^{\Delta myel}$ mice were analyzed. The gating strategy is outlined in Figure 3. Only spleens and livers were analyzed since lymphoid cells in the bone marrow are rare and therefore difficult to quantify. Cells were

gated as mentioned above for size, granularity, single and vital cells. Next, cells were gated for CD4 and CD8 as superordinate markers for cytotoxic and T helper cells. The $CD4^+$ gate was further dissected and analyzed for the co-inhibitory molecule PD-1, as well as the activation marker CD25. Cells positive for CD4 and CD25 were additionally gated for Foxp3, the master transcription factor of regulatory T cells.

Flow cytometric measurement and data processing. Samples were measured using a BD LSRFortessa^{TM} flow cytometer and the BD FACSDiva^{TM} software for data acquisition. All experiments were analyzed using the FlowJo^{TM} software.

2.2.18 Statistical analyses

GraphPad Prism 6 and 9 were used to perform statistical analyses. All data are represented as arithmetic means ± standard error of mean (SEM). Comparisons between two groups were statistically analyzed by unpaired Student's t-tests. For statistical evaluations of more than two groups, a one-way ANOVA was performed. In case of comparisons with two variables (i.e. "treatment" and "genotype") a two-way ANOVA was used. Multiple comparisons with dependent variables were corrected for multiplicity by a Bonferroni post-hoc test. P values were reported correspondingly. To identify outliers, the ROUT method was employed. P values <0.05 were considered statistically significant. Significancy is indicated by single or multiple asterisks (*) with the following ranges: *$p<0.05$, **$p<0.01$, ***$p<0.001$, ****$p<0.0001$.

3 Results

3.1 Generation of a myeloid-specific PKM2 knockdown

3.1.1 Genetic approach and breeding strategy

To assess the role of PKM2 in myeloid cells, a transgenic mouse strain was generated. The model was initially designed to study the effects of a PKM2 knockout within myeloid cells *in vitro* and *in vivo*. As described in (REF Introduction), pre-mRNA is spliced from the *Pkm* gene, a process which determines the isoform of the enzyme. Inclusion of exon 9 leads to *Pkm1* expression, whereas exon 10 is part of the *Pkm2* mRNA. Thus, excision of exon 10 prevents the cell from generating mature *Pkm2* mRNA, which ultimately results in a loss of PKM2 protein.

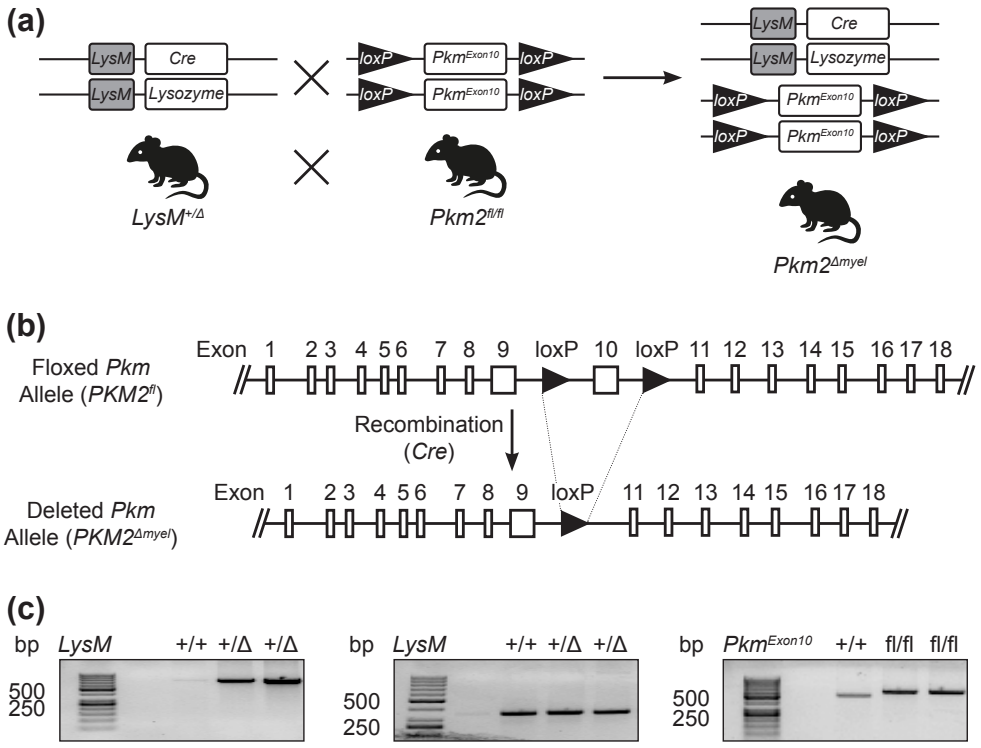

Figure 4: Genomic construct for a myeloid-specific knockdown of PKM2. (a) Breeding strategy. **(b)** Genetic locus of interest within the rodent *Pkm* gene on Chromosome 9 with *loxP* sites flanking *Pkm2*-specific exon 10 (upper panel). *Cre*-mediated excision of the exon (lower panel) was intended to lead to subsequent absence of *Pkm2* transcripts or protein (elements not shown to scale). **(c)** Genotyping by DNA purification, PCR amplification and subsequent gel electrophoresis. Left panel: *LysM-Cre* allele (+/Δ), 650 bp. Center panel: *LysM* wildtype allele (+/+), 320 bp. Right panel: Genotyping of wildtype alleles (+/+, 509 bp) and floxed alleles (fl/fl, 577 bp) within the *Pkm* gene.

For our studies, the Cre-loxP system was used to achieve a myeloid-specific knockout of PKM2. A brief summary of the genetic approach is demonstrated in Figure 4. *LoxP* sites were inserted into the *Pkm* gene on chromosome 9 in close proximity to exon 10 by

homologous recombination (Figure 4(a), center). Mice homozygous for the floxed allele ($Pkm2^{fl/fl}$) were then bred with mice heterozygous for a Cre recombinase downstream the promoter of their lysozyme gene (*LysM*, Figure 4(a), left) on chromosome 10 ($LysM^{+/\Delta}$). Once activated, this promoter leads to subsequent expression of *Cre*, which in turn results in the excision of floxed DNA segments (Figure 4(b)). *LysM* has been reported to be constitutively expressed in hematopoietic stem cells, particularly in myeloid progenitors and their descendants (Ye et al., 2003).

Since *LysM* encodes for lysozyme (a protein involved in myeloid defense reactions against a multitude of pathogens, e.g. gram-negative bacteria) and insertion of *Cre* disrupts this physiological response towards inflammatory stimuli, mice heterozygous for *Cre* (+/Δ) were chosen for the experiments in order to preserve one functional *LysM* allele (hereinafter referred to as $Pkm2^{\Delta myel}$). Animals negative for *Cre* (+/+) served as controls ($Pkm2^{fl/fl}$, see Figure 4(c), left and center panel). However, mice carrying *loxP* sites encompassing the PKM2-specific exon 10 were chosen as a background for both $Cre^{+/\Delta}$ animals and their controls ($Cre^{+/+}$, Figure 4(c), right panel), as they have previously been reported to be healthy and to show no overt phenotype (Israelsen et al., 2013).

3.1.2 *Cre*-mediated knockdown of PKM2

To evaluate the efficacy of *Cre* in the given model, bone marrow derived macrophages (BMDM) were prepared and differentiated *in vitro* as described. After extraction, the bone marrow of both $Pkm2^{fl/fl}$ and $Pkm2^{\Delta myel}$ mice was cultivated and differentiated into mature and naïve macrophages using supernatant containing M-CSF in their media. After seven days of differentiation and maturation, cells were harvested and Western blot analyses were performed. As Figure 5 shows, PKM2 was ubiquitously expressed in all experimental samples ((a), upper row). Lanes 1-4 within the blotting membrane represent lysates generated from $Pkm2^{fl/fl}$ BMDM, whereas lanes 5-8 show PKM2 expression in BMDM of $Pkm2^{\Delta myel}$ mice. The abundance of PKM2 protein in all experimental samples demonstrates an incomplete knockdown of PKM2 in $Pkm2^{\Delta myel}$-derived BMDM. However, a reduction in protein expression is visible. To quantify this effect, protein bands were normalized to their related housekeeping gene band β-Actin ((a), bottom row), which was stably expressed regardless of genotype. Quantification of Cre-loxP-mediated PKM2 knockdown efficacy (b) revealed a significant reduction in protein abundance by 33.4% ±3,69 in BMDM derived from $Pkm2^{\Delta myel}$ mice compared to controls (100% ±4.27, **p<0.01).

Next, a possible dose-dependency of *Cre* was assessed. Therefore, macrophages derived from bone marrow of mice carrying either no *Cre* allele ($Cre^{-/-}$, synonymous with $Pkm2^{fl/fl}$), one *Cre* allele ($Cre^{+/-}$, synonymous with $Pkm2^{\Delta myel}$) or two allels ($Cre^{+/+}$) downstream of the *LysM* promoter were prepared as described. As depicted in Figure 5(c), the efficacy of the *Cre*-mediated knockdown of *PKM2* mRNA increased in a dose-dependent manner. BMDM carrying one *Cre* recombinase allel showed a reduction

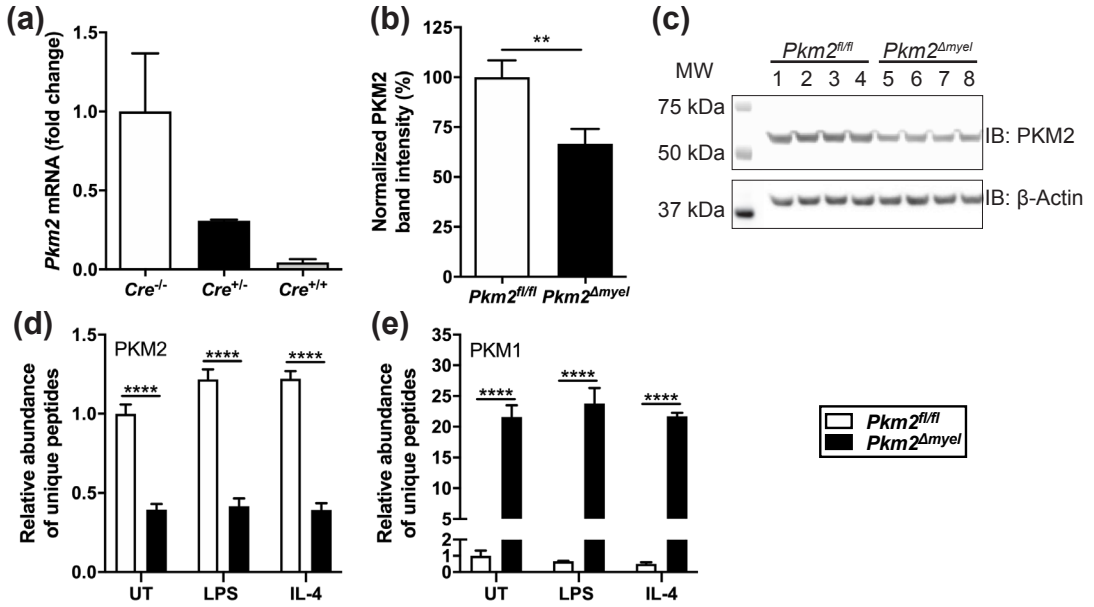

Figure 5: Evaluation of Cre-LoxP-mediated knockdown of PKM2 in BMDM. (a) PKM2 protein levels as determined by Western blot. Left: Marker bands (kDa). Lanes 1–4: BMDM lysates of $Pkm2^{fl/fl}$ mice, Lanes 5-8: BMDM lysates of $Pkm2^{\Delta myel}$ mice. Upper row: bands of PKM2 protein (60 kDa), bottom row: bands of β-Actin (loading control, 42 kDa). **(b)** Densitometric quantification of PKM2 knockdown in $Pkm2^{\Delta myel}$ BMDM by normalization of the PKM2 protein bands intensity to β-Actin as loading control. **(c)** *Pkm2* mRNA levels determined by qPCR (shown as fold changes to $Cre^{-/-}$ BMDM).

of PKM2 mRNA by 69.25% ±0.75, whereas BMDM with two *Cre* recombinase allels expressed 95.55% ±2.05 less PKM2 mRNA than the control group.

3.1.3 Implications of incomplete PKM2 knockdown on the quarternary structure of residual PKM2

As described in (), PKM2 subunits are present in an equilibrium of dimers and tetramers which differ significantly in their biological properties. To characterize residual PKM2 expression after partial knockdown and to assess whether partial knockdown had an influence on this homeostatic balance, BMDM of $Pkm2^{\Delta myel}$ mice were cross-linked by the addition of formaldehyde to the cell culture before harvesting the cells. Subsequent Western blot analyses revealed notable changes within the dimer:tetramer ratio. In untreated BMDM, tetrameric PKM2 was faintly expressed in both genotypes. However, BMDM derived from $Pkm2^{\Delta myel}$ mice showed even less tetrameric PKM2, though this difference was not significant (Figure 6(a), lanes 1-2 [100% ±39.9] vs. lanes 3-4 [59.14% ±1.61]). Stimulation of the cell culture with LPS (100ng/ml for 24 hours) did not noticeably alter the amount of tetrameric PKM2 in BMDM (93.58% ±6.66 in $Pkm2^{fl/fl}$ vs. 60.65% ±7.95 in $Pkm2^{\Delta myel}$).

Dimeric PKM2 is a result of posttranslational modification in response to activation of Toll-like receptors, such as TLR4, by inflammatory stimuli (Palsson-McDermott et al., 2015). Phosphorylation of Y105 leads to separation of PKM2 tetramers by releasing its

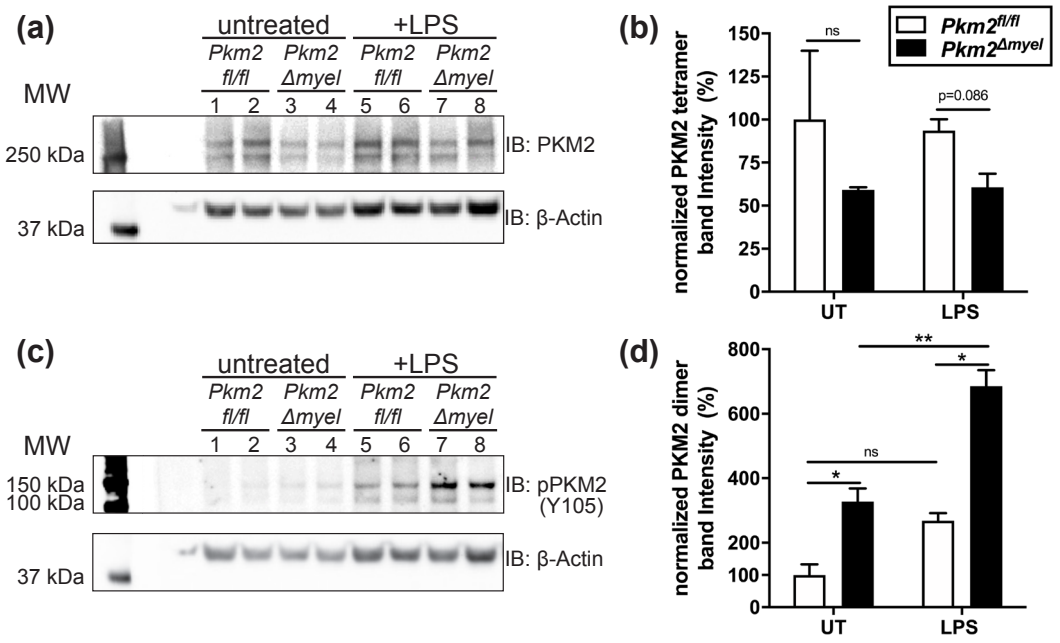

Figure 6: PKM2 quarternary protein structure. **(a)** Western blot of PKM2 (upper bands) in crosslinked BMDM either left untreated (lanes 1-4) or stimulated with LPS (100ng/ml for 24 hours, lanes 5-8), which were normalized to β-Actin (lower bands) **(b)** Quantification of tetrameric PKM2 normalized to β-Actin. **(c)** Western blot of pPKM2 (upper bands) in crosslinked BMDM stimulated as shown in (a) and normalized to β-Actin (lower bands). **(d)** Quantification of normalized dimeric pPKM2.

cofactor FBP, subsequently benefiting the formation of dimers (Hitosugi et al., 2009). In cellular homeostasis, PKM2 is expressed on a low level. Accordingly, PKM2 dimers were only gradually detectable. Faint bands for dimeric PKM2 were visible after visualization of the Western blot membrane. Figure 6(b) shows bands for dimeric PKM2 under untreated conditions. Yet, dimeric PKM2 was more abundant in BMDM generated from $Pkm2^{\Delta myel}$ mice than in those generated from $Pkm2^{fl/fl}$ mice (327.64% ±40.97 vs. 100% ±33, *p<0.05). In line with previous reports (Palsson-McDermott et al., 2015), stimulation with LPS (100ng/ml for 24 hours) lead to an increase of dimeric (phospho)PKM2 in both genotypes (lanes 5-8). Still, the increase in dimeric pPKM2 was more pronounced in BMDM derived from $Pkm2^{\Delta myel}$ mice than those of their controls (lanes 5-6 vs. 7-8). After normalization to β-Actin and in comparison to pPKM2 levels without stimulation, the proportional increase in dimeric pPKM2 after stimulation turned out to be significantly higher in $Pkm2^{\Delta myel}$-derived BMDM (685.34% ±49,77 vs. 268.29% ±23.69 in $Pkm2^{fl/fl}$-derived BMDM, *p<0.05). Dimeric PKM2 from $Pkm2^{\Delta myel}$-derived BMDM was markedly boosted by LPS stimulation (327.64% ±40.97 to 685.34% ±49.77, **p<0.01), whereas no significant increase was observed for $Pkm2^{fl/fl}$-derived BMDM (100% ±33 to 268.29% ±23.69).

3.2 *In vitro* characterization of *Pkm2*$^{\Delta myel}$-derived BMDM

3.2.1 Purity of BMDM cell culture

Further analyses of the myeloid phenotype included an estimate on the cell culture's purity. Therefore, BMDM were cultivated as described and examined by flow cytometry with regard to expression of typical myeloid markers on the cellular surface. As displayed

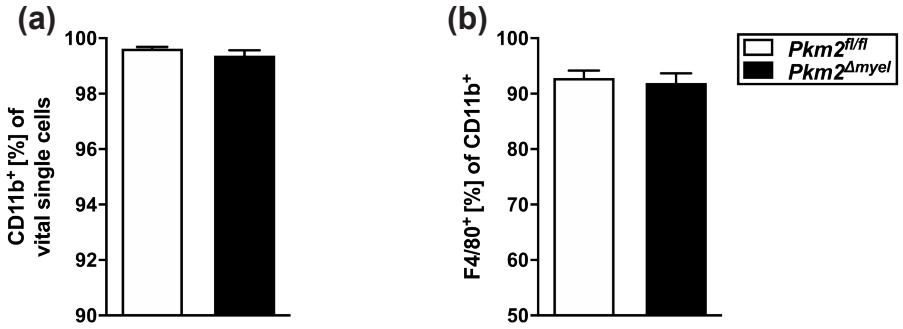

Figure 7: Purity of BMDM after differentiation. Bone marrow of *Pkm2*$^{\Delta myel}$ and *Pkm2*$^{fl/fl}$ mice was cultivated and differentiated over one week with supernatants gained from murine L929 fibroblasts, which contains M-CSF. Purity was assessed by flow cytometry for myeloid and macrophage surface markers (CD11b **(a)** and F4/80 **(b)**, respectively).

in Figure 7, the myeloid marker CD11b was expressed on the vast majority of cells (99.63% ±0.06 in *Pkm2*$^{fl/fl}$ BMDM vs. 99.38% ±0.19 in *Pkm2*$^{\Delta myel}$ BMDM). Further dissection showed F4/80 expression by more than 90% within the CD11b^{+} gate (92.83% ±1.35 in *Pkm2*$^{fl/fl}$ BMDM vs. 91.95% ±1.74 in *Pkm2*$^{\Delta myel}$ BMDM). There was no significant difference between genotypes in either measurement.

3.2.2 Cytokine profiles in BMDM

Macrophages form a heterogenous group of myeloid cells with a broad spectrum of subpopulations, depending on their microenvironment. Although simplified, the M1/M2 polarization theorem provides a useful model for the characterization of macrophages. Thus, BMDM were cultivated with typical stimuli of either classical (LPS) or alternative (IL-4) macrophage activation and subsequent polarization to assess whether PKM2 knockdown and subsequent dimerization of the residual protein might alter the inflammatory response. The experimental setup was completed by TEPP-46, a small molecule frequently used to activate PKM2 by promoting the assembly of PKM2 into tetramers, to evaluate its effect on the cells' immunological response.

Figure 8 shows fold changes in mRNA quantities of cytokines released by BMDM. Upon stimulation with LPS, a strong cytokine mRNA response was observable for *Il1*β, *Il6*, *Ccl2* and *Il10*. In case of *Il1*β mRNA, this increase was significant for *Pkm2*$^{\Delta myel}$-derived BMDM after stimulation with LPS ((a), 1.35-fold ±0.43 vs. 846.18-fold ±556.17, *$p<0.05$), but not for BMDM of *Pkm2*$^{fl/fl}$ mice. Similarly, an apparent rise could be observed in *Il10* mRNA levels after LPS stimulation in *Pkm2*$^{\Delta myel}$-derived BMDM

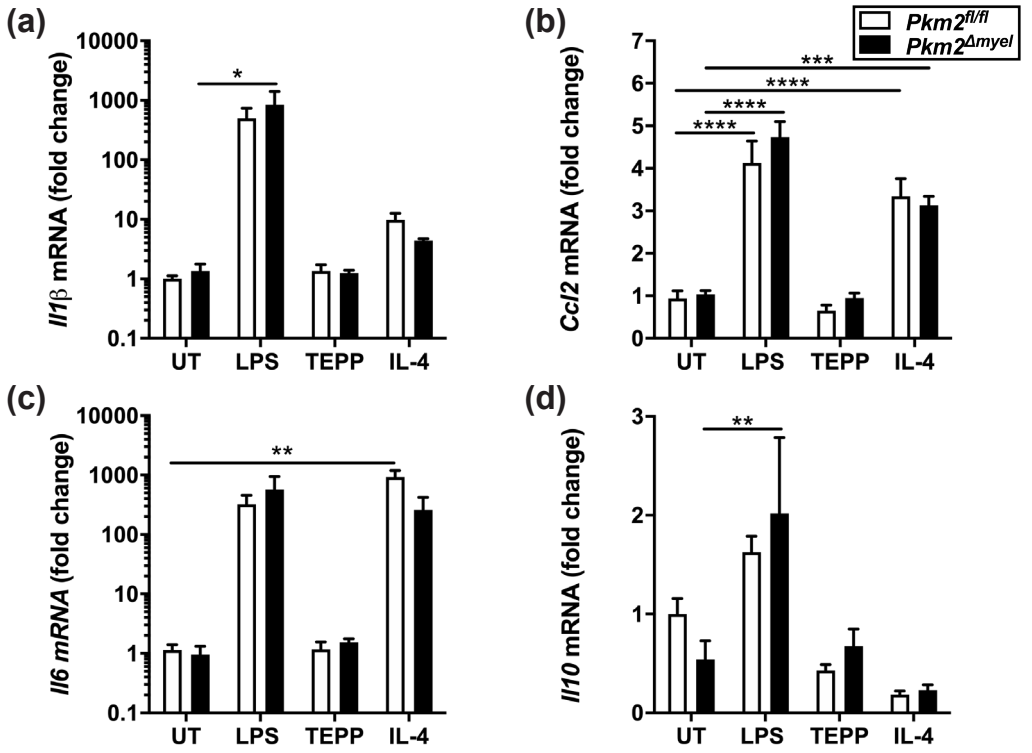

Figure 8: Cytokine profile of BMDM. BMDM differentiated from $Pkm2^{fl/fl}$ and $Pkm2^{\Delta myel}$ mice were either left untreated or stimulated for 24 hours with LPS (100ng/ml), TEPP-46 (100µM) or IL-4 (20ng/ml) in their respective medium. qPCR was performed, changes in mRNA quantities are shown as fold changes in comparison to untreated controls. Determination of *Il1*β **(a)**, *Ccl2* **(b)**, *Il6* **(c)** and *Il10* mRNA **(d)**.

compared to untreated conditions ((d), 0.54-fold ±0.19 vs. 2,02 ±0.77, **p<0.01). Yet, mRNA for *Ccl2* increased significantly under LPS stimulation in both genotypes ((b), 1-fold ±0.24 vs. 4.13-fold ±0.52 in $Pkm2^{fl/fl}$ BMDM, 1.04-fold ±0.09 vs. 4.73-fold ±0.37 in $Pkm2^{\Delta myel}$ BMDM, ****p<0.0001). TEPP-46 alone did not cause visible changes in mRNA of those cytokines. IL-4, responsible for alternative macrophage activation, lead to a significant increment in *Ccl2* ((b), 1-fold ±0.24 vs. 3.35-fold ±0.41 in $Pkm2^{fl/fl}$ BMDM, 1.04-fold ±0.09 vs. 3.13-fold ±0.21 in $Pkm2^{\Delta myel}$ BMDM) and *Il6* mRNA levels ((c), 1-fold ±0.33 vs. 932.33-fold ±264.73 in $Pkm2^{fl/fl}$ BMDM, **p<0.01). Although tending towards a more pro-inflammatory response in mRNA levels of those key cytokines, no other significant differences were detected in BMDM derived from $Pkm2^{\Delta myel}$ mice in comparison to their floxed controls with regard to mRNA levels.

Next, a bead-based immunoassay was employed to examine possible changes in cytokine levels on a protein level. To assess whether TEPP-46 was able to mitigate the strong pro-inflammatory cytokine response towards LPS, BMDM were pretreated with TEPP-46 (100µM) 30 minutes prior to LPS stimulation. Figure 9 shows quantities of the key pro -and anti-inflammatory cytokines TNFα, CCL2 and IL-10 in the supernatant. As expected and in accordance with the aforementioned strong pro-inflammatory response towards LPS in mRNA levels, LPS treatment lead to a significant increment in TNFα

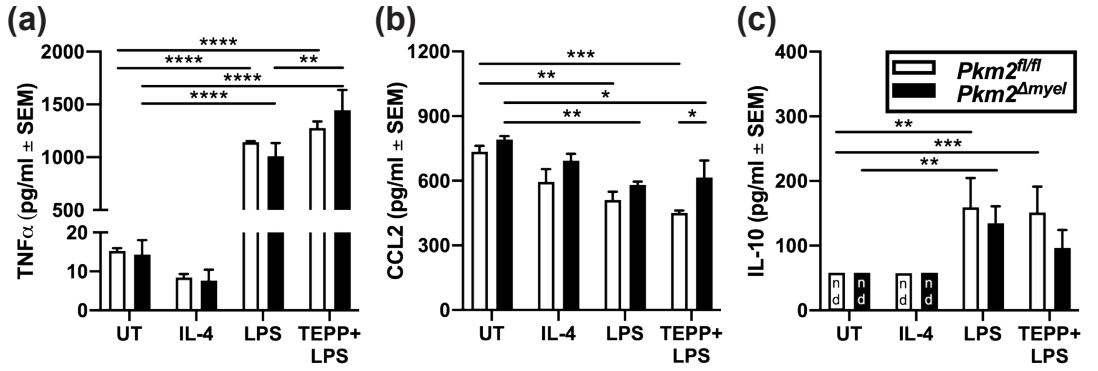

Figure 9: Protein levels of cytokines in BMDM as determined by immunoessay. BMDM of $Pkm2^{fl/fl}$ and $Pkm2^{\Delta myel}$ mice were either left untreated or stimulated for 24 hours with IL-4 (20ng/ml), LPS (100ng/ml) or TEPP-46 (100µM) 30 minutes prior to stimulation with LPS (10ng/ml) in their respective medium. Cytokine levels of TNFα **(a)**, CCL2 **(b)** and IL-10 **(c)** (n.d. = not detectable).

production in both genotypes in comparison to untreated conditions ((a), 15.29pg/ml vs. 1141.72pg/ml in $Pkm2^{fl/fl}$ BMDM and 14.30pg/ml vs. 1010.20pg/ml in $Pkm2^{\Delta myel}$ BMDM, ****p<0.0001). Surprisingly, TEPP-46 did not ameliorate this response. On the contrary, pretreatment of the cells resulted in a significantly higher TNFα production of BMDM when compared to LPS alone in $Pkm2^{\Delta myel}$ BMDM (1010.29pg/ml ±123.30 vs. 1445.48pg/ml ±191.67, **p<0.01), whereas no significant difference was observed in $Pkm2^{fl/fl}$ BMDM. For CCL2, a small cytokine of the CC-chemokine family which multiplies the recruitment of monocytes from the bloodstream, unexpectedly high protein levels were detectable in supernatants of untreated BMDM. This might be due to the fact that a L929-fibroblast-derived growth medium was used to differentiate naïve bone marrow into mature macrophages. This supernatant has recently been reported to contain high amounts of CCL2 (Heap et al., 2020). Interestingly, LPS stimulation of BMDM resulted in a substantial decrease of CCL2 protein in both genotypes ((b), 725.48pg/ml ±26.22 vs. 511.36pg/ml ±37.23 in $Pkm2^{fl/fl}$ BMDM and 791.41pg/ml ±15.77 vs. 580.54 in $Pkm2^{\Delta myel}$ BMDM, **p<0.01). Pretreatment with TEPP-46 caused CCL2 levels to recede even further in $Pkm2^{fl/fl}$ BMDM, whereas BMDM derived from $Pkm2^{\Delta myel}$ mice displayed significantly higher levels of the chemokine (450.81pg/ml ±10.89 vs. 615.03pg/ml ±79.12, *p<0.05). Still, CCL2 turned out to be significantly reduced when treated with TEPP-46 and LPS in both genotypes in comparison to untreated conditions (725.48pg/ml ±26.22 vs. 450.81pg/ml ±10.89 in $Pkm2^{fl/fl}$ BMDM and 791.41pg/ml ±15.77 vs. 615.03pg/ml ±79.12 in $Pkm2^{\Delta myel}$ BMDM, *p<0.05, ***p<0.001).

As for the anti-inflammatory response, IL-10 protein levels were measured as well. Untreated and IL-4 treated BMDM did not produce detectable amounts of IL-10, whereas stimulation with LPS triggered a robust IL-10 response regardless of genotype ((c), 159.16pg/ml ±45.44 for $Pkm2^{fl/fl}$ BMDM, **p<0.01; 134.6pg/ml ±26.27 for $Pkm2^{\Delta myel}$ BMDM, **p<0.01). Notably, IL-10 did not increase after pretreatment

of the cell culture with TEPP-46 prior to LPS stimulation, which which stands in contrast to previous reports by Palsson-McDermott and colleagues who performed similar experiments in BMDM (Palsson-McDermott et al., 2015). IL-10 was slightly less abundant in the supernatants of cells pretreated with TEPP-46 (151.4pg/ml ±40.06 for $Pkm2^{fl/fl}$ BMDM, 96.66pg/ml ±27.65 for $Pkm2^{\Delta myel}$ BMDM).

Taken together, BMDM prepared as described showed a sufficient purity for further analyses. Although the pro -and anti-inflammatory response by BMDM derived from both genotypes turned out to be widely comparable, a tendency towards a more pronounced cytokine response was observable upon LPS stimulation in BMDM derived from $Pkm2^{\Delta myel}$ mice. Adding TEPP-46 to the cell culture medium to promote the assembly of tetrameric PKM2 did neither dampen the cellular pro-inflammatory response after LPS stimulation significantly, nor did it amplify the production IL-10 in BMDM.

3.2.3 Metabolic characteristics of BMDM

Pyruvate kinase as one of the key regulatory enzymes of glycolysis is located at the very center of metabolism and provides glucose-derived carbon compounds for the ensuing tricarboxylic acid cycle. As described in (), regulation of the glycolytic flux in myeloid cells enables the cells to divert metabolic intermediates into the generation of biomass (such as purines or pyrimidines for proliferation) or to activate intracellular signalling pathways that have an impact on genetic transcription. To evaluate the metabolic properties of BMDM derived from both genotypes, metabolic analyses were performed using a Seahorse Analyzer for measurement of extracellular acidification (ECAR) and oxygen consumption (OCR) of the cells in either untreated or stimulated cultural conditions. The results are displayed in Figure 10. BMDM derived from $Pkm2^{\Delta myel}$ mice showed a substantially increased basal oxygen consupmtion compared to controls (Figure 10(a), 339.6pmol/min ±25.43 vs. 264.05pmol/min ±11.48, *p<0.05). A similar effect was visible after two hours of stimulation with LPS (357.57pmol/min ±15.0 vs. 241.84pmol/min ±22.59, ***p<0.001). After 24 hours, this effect had diminshed and did not show signficant differences between genotypes. However, the overall basal OCR was drastically reduced after 24 hours of LPS exposure in comparison to untreated conditions (101.08pmol/min ±4.69 vs. 264.05 pmol/min ±11.48 in $Pkm2^{fl/fl}$ BMDM, ****p<0.0001; 129.9pmol/min ±9.24 vs. 339.6pmol/min ±25.43 in $Pkm2^{\Delta myel}$ BMDM, ****p<0.0001). Treatment of the cell culture with TEPP-46 (100µM) resulted in a massive reduction of oxygen consumption that exceeded the aforementioned reduction caused by 24 hours of LPS stimulation. Interestingly, the effect on cellular respiration was more pronounced in BMDM derived from $Pkm2^{\Delta myel}$ mice, which only exhibited lower respiratory rates after treatment with TEPP-46 in comparison to controls (49.95pmol/min ±3.26 vs. 264.05 pmol/min ±11.48 in $Pkm2^{fl/fl}$ BMDM, ****p<0.0001; 35.8pmol/min ±3.37 vs. 339.6pmol/min ±25.43 in $Pkm2^{\Delta myel}$ BMDM, ****p<0.0001).

Simultaneous to cellular respiration, the change in extracellular pH was assessed (Figure 10(b)). Extracellular acidification as a result of proton efflux served as surrogate

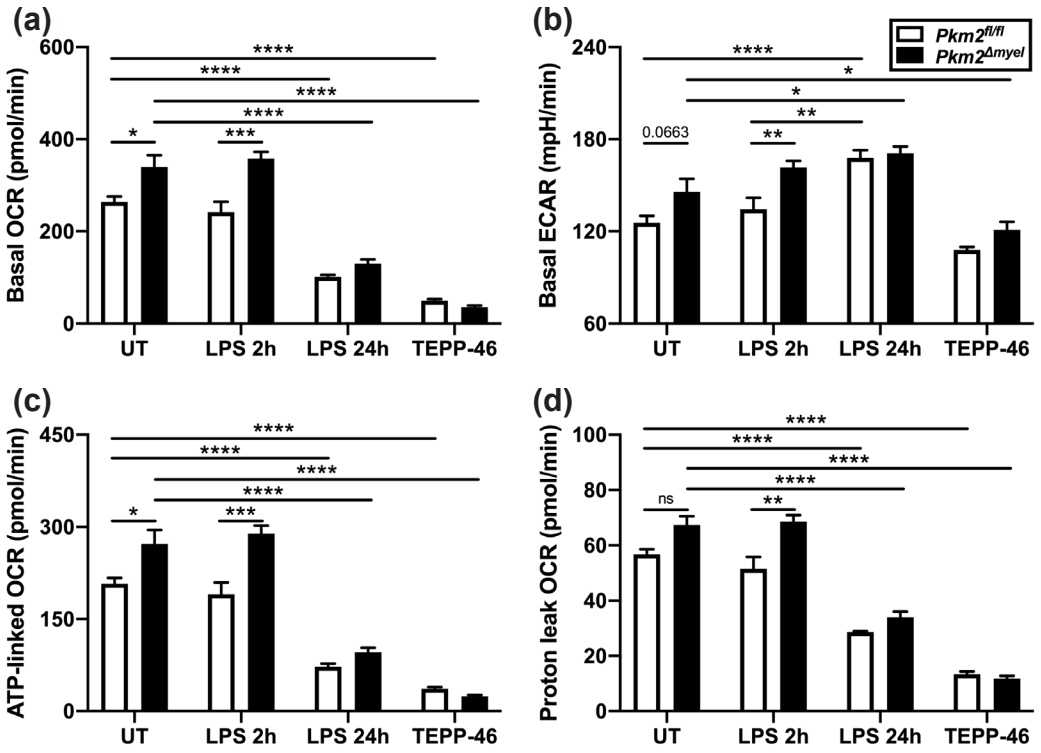

Figure 10: Metabolic properties of BMDM derived from $Pkm2^{fl/fl}$ and $Pkm2^{\Delta myel}$ mice. BMDM were either left untreated or stimulated with LPS (100ng/ml) for 2 or 24 hours or treated with TEPP-46 (100µM) and subsequently assessed by a Seahorse XFe96 metabolic analyzer. **(a)** Intrinsic oxygen consumption rate (OCR) within different treatments. **(b)** Intrinsic extracellular acidification rate (ECAR). **(c)** Calculated fraction of OCR linked exclusively to ATP synthesis. **(d)** Calculated fraction of OCR not attributable to ATP synthesis (proton leakage).

parameter for glycolytic turnover in the cell culture. Notably, $Pkm2^{\Delta myel}$ BMDM showed increased rates of acidification in untreated conditions (145.78mpH/min ±8.56 in $Pkm2^{\Delta myel}$ BMDM vs. 125.64mpH/min ±4.56 in $Pkm2^{fl/fl}$ BMDM, p=0.063) and after short term LPS exposure (161.57mpH/min ±4.36 in $Pkm2^{\Delta myel}$ BMDM vs. 134.42mpH/min ±7.47 in $Pkm2^{fl/fl}$ BMDM, **p<0.01). After 24 hours of LPS stimulation, BMDM from both genotypes revealed significant increments in ECAR in comparison to untreated conditions (167.85mpH/min ±5.01 vs. 125.64mpH/min ±4.56 in $Pkm2^{fl/fl}$ BMDM, ****p<0.0001; 170.85mpH/min ±4.37 vs. 145.78mpH/min ±8.56 in $Pkm2^{\Delta myel}$ BMDM, *p<0.05). However, there was no significant difference between the genotypes after 24 hours of stimulation with LPS. Treatment with TEPP-46 lead to a decrease in basal ECAR in both genotypes, though this this turned out to be only substantially lower in $Pkm2^{\Delta myel}$ BMDM compared to untreated conditions (121.02mpH/min ±5.27 vs. 145.78mpH ±8.56, *p<0.05).

Next, the observed differences in basal respiration and glycolytic turnover were complemented by calculating the proportion of cellular respiration attributable to ATP synthesis (see Figure 10(c)). ATP-linked respiration can be blocked by oligomycin and

is the difference between basal OCR and proton leakage (Divakaruni et al., 2014). Very similarly to basal OCR values, the amount of ATP-linked respiration showed the same differences between genotypes and treatments. Without stimulation, ATP-linked O_2 consumption was increased in BMDM derived from $Pkm2^{\Delta myel}$ mice in comparison to floxed controls (272.26pmol/min ±22.5 vs. 207.39pmol/min ±9.59, *p<0.05), an effect that was also visible after two hours of LPS stimulation (190.31 pmol/min ±19.18 in $Pkm2^{fl/fl}$ BMDM vs. 288.96pmol/min ±13.14 in $Pkm2^{\Delta myel}$ BMDM, ***p<0.001). 24 hours of LPS exposure caused ATP-linked OCR to decline equivalently (72.37pmol/min ±4.81 in $Pkm2^{fl/fl}$ BMDM, ****p<0.0001; 95.88pmol/min ±7.28 in $Pkm2^{\Delta myel}$ BMDM, ****p<0.0001). BMDM treated with TEPP-46 exhibited a significantly reduced ATP-linked consumption of O_2 in comparison to their untreated counterparts (36.57pmol/min ±2.48 in $Pkm2^{fl/fl}$ BMDM, ****p<0.0001; 24.01pmol/min ±2.53 in $Pkm2^{\Delta myel}$ BMDM, ****p<0.0001). Notably, the residual O_2 consumption was minor in $Pkm2^{\Delta myel}$ derived BMDM than their controls only after treatment of the cells with TEPP-46.

To further dissect the underlying metabolic features of BMDM, proton leakage was determined. Proton leakage occurs when the coupling of proton flux through the mitochondrial membrane as part of ATP synthesis is incomplete and is indicative for the generation of reactive oxygen species in macrophages (El-Khoury et al., 2011). In homeostasis, $Pkm2^{fl/fl}$ BMDM showed an increased proton leak in comparison to the control group, though this difference was not statistically significant (67.35pmol/min ±3.17 vs. 56.67pmol/min ±1.94). After two hours of LPS stimulation, proton leakage increased slightly in $Pkm2^{\Delta myel}$ BMDM, whereas stimulation caused a small decrease in $Pkm2^{fl/fl}$ BMDM (68.6pmol/min ±2.35 vs. 51.54 ±4.24, **p<0.01). Again, long-term stimulation with LPS and exposure to TEPP-46 significantly reduced proton leakage in both genotypes (LPS 24h: 28.61pmol/min ±0.35 in $Pkm2^{fl/fl}$ BMDM, 34.02pmol/min ±2.05 in $Pkm2^{\Delta myel}$ BMDM; TEPP-46: 13.38pmol/min ±0.96 in $Pkm2^{fl/fl}$ BMDM, 11.79pmol/min ±0.98 in $Pkm2^{\Delta myel}$ BMDM).

The mitochondrial stress assay mentioned above was performed to elicit the cellular reaction to specific reagents blocking certain parts of mitochondrial proton flux and therefore allowing assumptions on the cellular energy metabolism in both genotypes. Figure 11 shows detailed results of the assay with regard to genotypes and various conditions of the cell culture (Basal OCR measurements given in Figure 10 reflect the mean of the three repeated measurements before the injection of oligomycin in Figure 11 for the respective treatment. OCR values given in the following paragraph represent mean values of temporal triplicates for each genotype displayed in Figure 11).

As shown in Figures 10(a) and 11(a), untreated BMDM obtained and differentiated from $Pkm2^{\Delta myel}$ mice displayed an elevated basal OCR. Blocking complex V of the respiratory chain (ATP synthase) by the injection of oligomycin lead to a substantial decrement of O_2 consumption in both genotypes, simultaneously minimizing the difference between them (94.59pmol/min ±2.72 in $Pkm2^{fl/fl}$ BMDM, 111.95pmol/min ±5.22 in $Pkm2^{\Delta myel}$ BMDM). The subsequent injection of FCCP (which results in a collapse of the proton gradient and thus causes OCR to reach maximum levels) restored

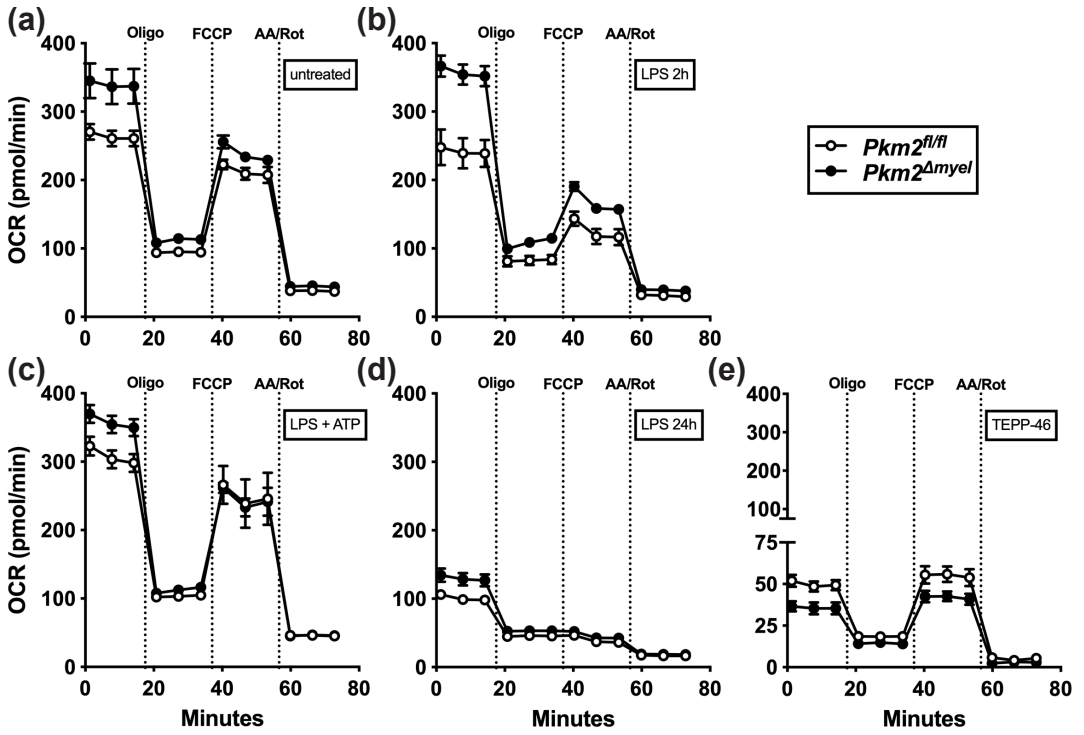

Figure 11: Detailed measurements of the mitochondrial stress assay. BMDM derived from both genotypes were either left untreated **(a)** or stimulated with LPS (100ng/ml) for 2 hours **(b)** or 24 hours **(d)**, treated with LPS (100ng/ml) and ATP (250µM, **(c)**) or TEPP-46 (100µM, **(e)**), respectively and subsequently assessed by a Seahorse XFe96 metabolic analyzer.

respiration partly. It failed, however, to reach levels above basal OCR as originally intended and which would have been necessary to assess the spare respiratory capacity within the cell culture (213.11pmol/min ±8.72 in $Pkm2^{fl/fl}$ BMDM, 239.56pmol/min ±6.86 in $Pkm2^{\Delta myel}$ BMDM). The final injection of antimycin A and rotenone, inhibitors of respiratory chain complexes III and I that completely cease mitochondrial respiration, reduced O_2 consumption to comparable levels between genotypes (37.92pmol/min ±in $Pkm2^{fl/fl}$ BMDM, 44.61pmol/min ±2.88 in $Pkm2^{\Delta myel}$ BMDM), indicating no genotype-specific differences in non-mitochondrial respiration and equal cell numbers within the wells of the analysis plate (observable in all experimental setups (a)-(e)). Short term stimulation with LPS (Figure 11(b)) showed similar differences between genotypes before (241.84pmol/min ±22.59 in $Pkm2^{fl/fl}$ BMDM vs. 357.57pmol/min ±15.0 in $Pkm2^{\Delta myel}$ BMDM) and after the injection of oligomycin (82.53pmol/min ±6.75 in $Pkm2^{fl/fl}$ BMDM vs. 107.73pmol/min ±4.08 in $Pkm2^{\Delta myel}$ BMDM). The injection of FCCP only raised OCR partly, suggesting mitochondrial dysfunction in activated BMDM; this effect was more pronounced in $Pkm2^{\Delta myel}$ BMDM (125.87pmol/min ±10.87 in $Pkm2^{fl/fl}$ BMDM vs. 168.73pmol/min ±5.37 in $Pkm2^{\Delta myel}$ BMDM). Interestingly, adding exogeneous ATP restored cellular respiration after FCCP injection (Figure 11(c)) to levels comparable to untreated conditions (a). In this case, supplementary ATP elevated the OCR of BMDM derived from both genotypes on almost

identical levels (250.33pmol/min ±33.64 in $Pkm2^{fl/fl}$ BMDM vs. 245.49pmol/min ±13.53 in $Pkm2^{\Delta myel}$ BMDM) after FCCP, whereas initial differences were once more visible before the injetion of oligomycin (308.2pmol/min ±13.32 in $Pkm2^{fl/fl}$ BMDM vs. 358.11pmol/min ±12.75 in $Pkm2^{\Delta myel}$ BMDM). Long term LPS stimulation resulted in drastically reduced OCR (Figure 11(d), 101.07pmol/min ±4.69 in $Pkm2^{fl/fl}$ BMDM vs. 129.9pmol/min ±9.24 in $Pkm2^{\Delta myel}$ BMDM); subsequent exposure to assay modulators equilibrated any genotypic differences. Remarkably, FCCP completely failed to induce any increase in O_2 consumption in this case. TEPP-46 significantly attenuated the overall OCR in both genotypes (Figure 11(e), see also Figure 10(a)). Only upon stimulation with TEPP-46, $Pkm2^{fl/fl}$ BMDM exhibited higher OCR than $Pkm2^{\Delta myel}$ BMDM before (49.51pmol/min ±3.26 vs. 35.8pmol/min ±3.36) and after modulation cellular respiration by oligomycin (18.54pmol/min ±1.42 vs. 14.32pmol/min ±1.46), antimycin A or rotenone. Treatment with TEPP-46 furthermore restored the expected increase in OCR after injection of FCCP (55.04pmol/min ±5.03 in $Pkm2^{fl/fl}$ BMDM vs. 42pmol/min ±3.2 in $Pkm2^{\Delta myel}$ BMDM), even though respiration in this assay was generally diminished.

In summary, BMDM of $Pkm2^{\Delta myel}$ mice showed increased basal O_2 consumption and extracellular acidification in comparison to floxed controls, both of which intensified after short term exposure of the cells to LPS. Since the differences were attributable to changes in ATP-linked O_2 consumption, these results point to genotypic deviations in cellular ATP demand, possibly related to macromolecule biosynthesis or other cellular responses. Higher levels of proton leakage were also observable in $Pkm2^{fl/fl}$ BMDM, probably indicating enhanced generation of reactive oxygen species in these cells. Long term LPS stimulation over 24 hours amplified extracellular acidification while simultaneously reducing O_2 consumption under normoxic conditions, depicting a Warburg effect in BMDM of either genotype. Overall, long term exposure of BMDM to LPS minimized genotypic differences. Treatment with TEPP-46 generally reduced cellular metabolism with regard to glycolytic flux and respiration, the latter of which has been reported previously in NK cells (Walls et al., 2020). Upon detailed examination, $Pkm2^{\Delta myel}$ BMDM revealed to rely more strongly on oxidative respiration than their controls. BMDM derived from both genotypes exhibited impaired maximum respiratory capacity after the administration of FCCP, with this defect being most pronounced after LPS administration. Addition of ATP partly restored spare respiratory capacity, whereas only TEPP-46 raised OCR above basal respiration after FCCP injection. Furthermore, only after exposure to TEPP-46 BMDM derived from $Pkm2^{fl/fl}$ mice showed increased OCR in comparison to $Pkm2^{\Delta myel}$ BMDM, suggesting a differential regulation of the metabolic flux via PKM2 depending on its abundance and state of activation.

3.2.4 Evaluation of M2 macrophage polarization in BMDM

As mentioned, macrophages develop numerous characteristics upon activation, depending on their microenvironment. Stimulation with IL-4 is a hallmark of alternative activation

and indicative for resolution of inflammatory processes by expression of modulatory molecules such as CD206 or secretion of anti-inflammatory cytokines (Stein et al., 1992). Previous reports suggested an involvement of PKM2 in macrophage polarization (Palsson-McDermott et al., 2015). To assess the possibility that a shift in PKM2 quarternary structure might alter the capability of macrophages to promote distinct features of alternative activation, flow cytometric analyses were performed. Figure 12 illustrates details of the analyses. Mature BMDM stably expressed the M2 marker CD206 (macrophage mannose receptor) even before further stimulation (, **(a)**). Similarly, mean fluorescence was low but detectable in untreated BMDM. As expected, LPS stimulation, emblematic of M1 polarization, lead to a decrease in $CD206^+$ BMDM in both genotypes. Treatment with TEPP-46 did not substantially increase the relative number $CD206^+$ macrophages, though it resulted in a minor increment of CD206 mean fluorescence intensity in $Pkm2^{\Delta myel}$ BMDM compared to untreated conditions (418 ±26.64 vs. 240.75 ±30.63, p=0.09). IL-4 greatly enhanced both abundance and MFI of CD206 in BMDM regardless of genotype in comparison to untreated conditions (relative cell counts: 45.83% ±8.9 vs. 18.49% ±6.08 in $Pkm2^{fl/fl}$ BMDM, 46.4% ±7.57 vs. 11.7% ±1.44 in $Pkm2^{\Delta myel}$ BMDM; MFI: 701.75 ±96.17 vs. 280.67 ±34.28 in $Pkm2^{fl/fl}$ BMDM, 699.75 ±95.68 vs. 240.75 ±30.63 in $Pkm2^{\Delta myel}$ BMDM). Figure 12(d) exemplarily visualizes the impact of LPS, TEPP-46 and IL-4 on $Pkm2^{fl/fl}$ BMDM with regard to CD206 expression. In addition to the metabolic characteristics mentioned in section 3.2.3, where different treatments caused significant changes in respiration and extracellular acidification, the presence of CD39, an ectonucleotidase that hydrolyzes extracellular ATP, was determined. Extracellular ATP acts as a danger signal which drives macrophages towards a pro-inflammatory phenotype characterized by NLRP3 inflammasome activation and subsequent release of IL-1β (Mariathasan et al., 2006). Apart from the observation that macrophages rely strongly on glycolysis for their metabolic demands when challenged with pro-inflammatory stimuli (Rodríguez-Prados et al., 2010), ATP release by macrophages is dependent on glycolytic turnover. ATP, in turn, induces CD39 expression, thereby limiting its pro-inflammatory effect and therefore playing in important role in resolving inflammatory responses (Cohen et al., 2013, Savio et al., 2020). Figure 12(c) shows a robust CD39 MFI in the flow cytometric analysis of BMDM derived from both genotypes, notably also in untreated cell culture conditions. As expected, LPS stimulation resulted in a substantial increase in CD39 MFI in both genotypes (1565.75 ±159.79 vs. 1120.68 in $Pkm2^{fl/fl}$ BMDM, *p<0.05; 1591 ±76.43 vs. 942.5 ±29.78 in $Pkm2^{\Delta myel}$ BMDM, **p<0.01), presumably due to the increase in glycolytic activity in BMDM (see Figure 10(b)). Treatment with TEPP-46 counterintuitively caused CD39 to amplify even further in comparison to untreated cells (2051.75 ±166.68 in $Pkm2^{fl/fl}$ BMDM and 2269.75 ±117.56 in $Pkm2^{\Delta myel}$ BMDM, both ****p<0.0001), despite the previous observation that TEPP-46 reduced their glycolytic activity.

As another established marker of M2 polarization, CD301 (C-type lectin domain family member 10A, CLEC10A) expression was determined by flow cytometry. While

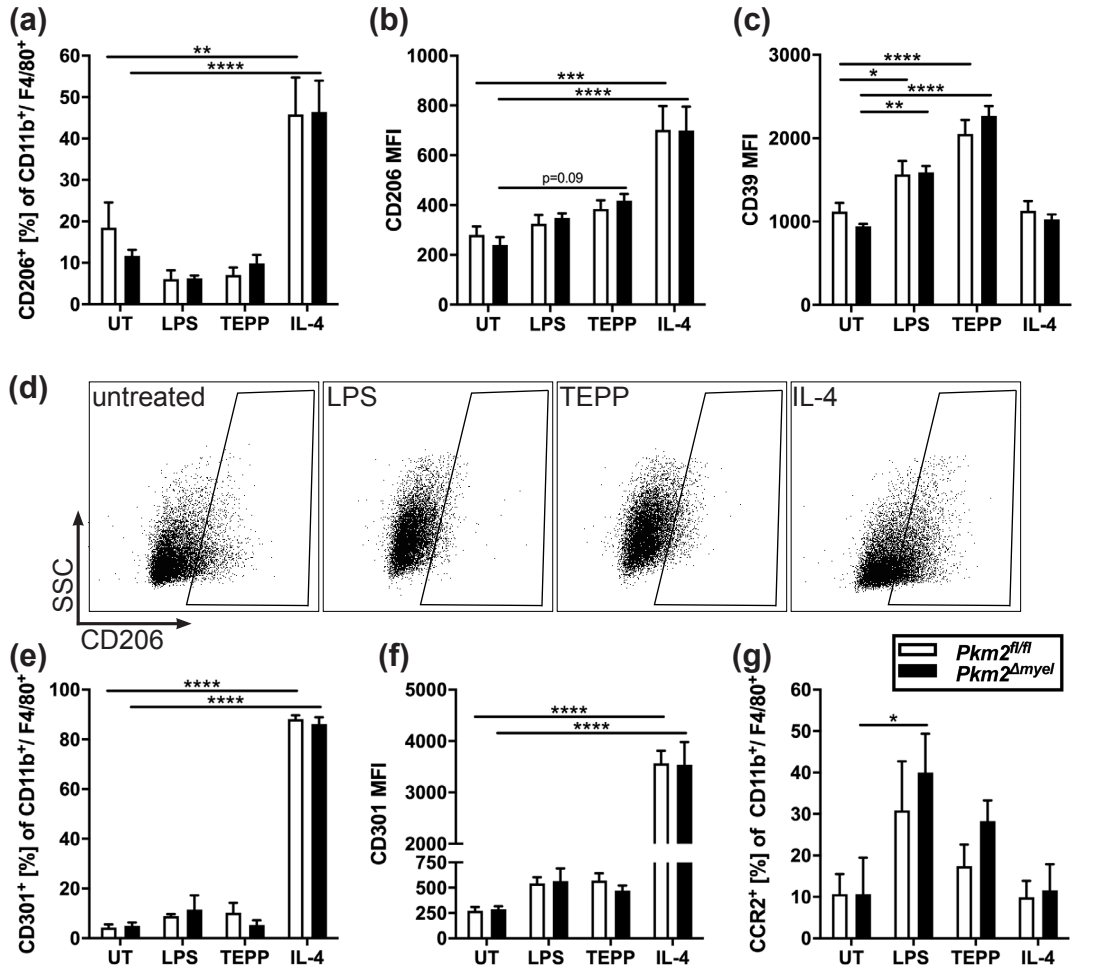

Figure 12: Flow cytometric analysis of BMDM M2 polarization. BMDM derived from both genotypes were either left untreated or stimulated with LPS (100ng/ml), TEPP-46 (100µM), or IL-4 (20ng/ml). **(a)** Abundance of $CD206^+$ macrophages and corresponding mean fluorescence intensity (MFI, **(b)**). **(c)** MFI of the ectonucleotidase CD39 on BMDM. **(d)** Illustrative dot plots of CD206 (x axis) and side scatter (y axis) subject to respective treatments in $Pkm2^{fl/fl}$ BMDM. **(e)** Abundance of $CD301^+$ macrophages and corresponding MFI **(f)**. **(g)** Relative quantities of $CCR2^+$ BMDM in untreated and stimulated conditions.

being only marginally detectable in untreated conditions, treatment with IL-4 caused massive upregulation of CD301 in both genotypes (see (e), 88.18% ±1.5 vs. 4.32% ±1.2 in $Pkm2^{fl/fl}$ BMDM, 86.13% ±2.8 vs. 4.95% ±1.33 in $Pkm2^{\Delta myel}$ BMDM, both ****$p<0.0001$). Upon challenge with LPS or TEPP-46, BMDM of either genotype did not react with a substantial change in CD301 expression. MFI increased correspondingly after IL-4 stimulation (3570.25 ±239.04 vs. 271.75 ±38.39 in $Pkm2^{fl/fl}$ BMDM, 3539.5 ±440.47 vs. 285 ±30.68 in $Pkm2^{\Delta myel}$ BMDM, both ****$p<0.0001$), whereas LPS and TEPP-46 only caused minor changes in fluorescence intensity, indicating a similar effect on a single cell level. Lastly, expression of CCR2 (C-C chemokine receptor type 2), a receptor known to be upregulated upon exposure to IL-10 and TGF-β (i.e. part of resolution of inflammation), was measured (Figure 12(f)). Untreated BMDM showed

low levels of CCR2 in BMDM derived from both genotypes, as did IL-4. LPS stimulation caused the fraction of $CCR2^{+}$ cells to triple in percentage of mature macrophages in $Pkm2^{fl/fl}$ BMDM in comparison to untreated cells (30.87% ±11.87 vs. 10.67 ±4.83, not significant); the increase was even more pronounced in $Pkm2^{\Delta myel}$ BMDM (40% ±9.93 vs. 10.67% ±8.81, *p<0.05). Interestingly, treatment with TEPP-46 without further LPS challenge also resulted in CCR2 upregulation in BMDM derived from both genotypes in an analogous manner (17.42% ±5.21 in $Pkm2^{fl/fl}$ BMDM, 28.3% ±4.99 in $Pkm2^{\Delta myel}$ BMDM, not significant). The effects of classical and alternative

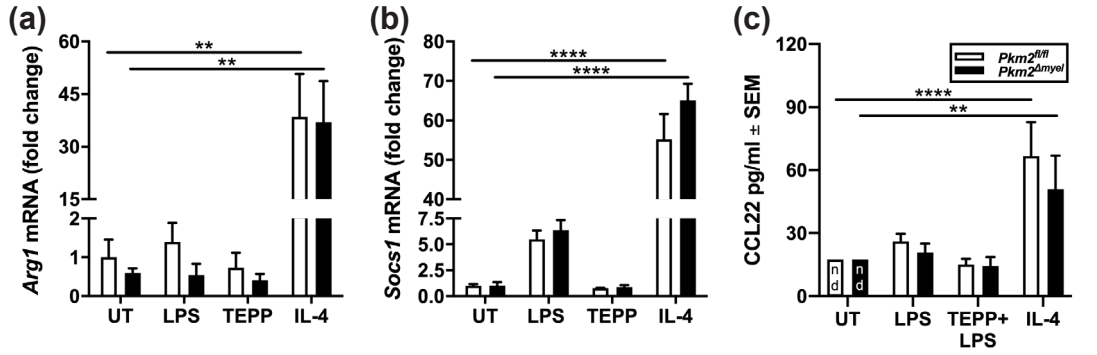

Figure 13: Analysis of additional M2 markers in BMDM. (a, b) BMDM derived from both genotypes were either left untreated or stimulated with LPS (100ng/ml), TEPP-46 (100µM), or IL-4 (20ng/ml) and subsequently analyzed by qPCR for *Arg1* **(a)** and *Socs1* **(b)**. **(c)** Immunoassay-based determination of CCL22 protein levels in BMDM treated as described in Figure 9 (n.d. = not detectable).

macrophage activation were also examined with regard to additional M2 polarization markers on their mRNA level. Arginase, catalyzing the conversion of arginine to ornithine (i.e. the last step of the urea cycle), is characteristically upregulated in M2 macrophages (REF). Ornithine is subsequently converted into polyamins, which can be used for DNA synthesis. Furthermore, ornithine can act as a precursor for proline, one of the major substrates for collagen synthesis and tissue repair (Mills, 2001). qPCR analyses revealed only minor changes concerning *Arg1* expression between $Pkm2^{fl/fl}$ and $Pkm2^{\Delta myel}$ BMDM in untreated conditions and after stimulation with LPS or TEPP-46. Treatment of the cells with IL-4 resulted in a significant upregulation of *Arg1* in both genotypes when compared to untreated conditions (38.48-fold ±12.28 vs. 1-fold ±0.46 in $Pkm2^{fl/fl}$ BMDM, 37.01-fold ±11.7 vs. 0.59-fold ±0.124 in $Pkm2^{\Delta myel}$ BMDM, both **p<0.01). Another key regulator involved in the arginine pathway is SOCS1 (suppressor of cytokine signalling 1), which tightly controls the ratio between M2-characteristic *Arg1* and M1-typical *iNOS* expression. As expected, IL-4 effectively induced upregulation of *Socs1* in comparison to untreated cells (55.19-fold ±6.43 vs. 1-fold ±0.15 in $Pkm2^{fl/fl}$ BMDM, 65.15-fold ±4.1 vs. 1.03-fold ±0.33 in $Pkm2^{\Delta myel}$ BMDM) without revealing a significant difference between genotypes. Interestingly, stimulation with LPS also lead to an increase in *Socs1* mRNA (5.49-fold ±0.85 in $Pkm2^{fl/fl}$ BMDM, 6.38-fold ±0.97 in $Pkm2^{\Delta myel}$ BMDM, not significant), indicating a

role for SOCS1 signaling in M1 macrophages. Furthermore, CCL22 was determined by immunoassay as a M2-typical cytokine. Again, IL-4 stimulation lead to a significant boost in CCL-22 production, which turned out to be slightly less substantial in BMDM derived from $Pkm2^{\Delta myel}$ (66.7pg/ml ±16.09 vs. not detectable in $Pkm2^{fl/fl}$ BMDM, ****p<0.0001; 50.94pg/ml ±16 vs. not detectable in $Pkm2^{\Delta myel}$ BMDM, **p<0.01). LPS alone and in combination with TEPP-46 only triggered negligible CCL22 responses.

In conclusion, BMDM prepared as described were equally susceptible to classical and alternative macrophage activation regardless of genotype. Cells derived from both genotypes showed unimpeded M2 polarization with regard to surface markers (CD206, CD301), mRNA levels of regulatory proteins (*Arg1, Socs1*) and chemokines (CCL22) without genotype-specific characteristics. However, an enhancement in CCR2 expression was visible in $Pkm2^{\Delta myel}$ BMDM, presumably implying differences in macrophage chemotaxis. Apart from a modest increment in mean fluorescence for CD206 (Figure 12(b)), pointing to a probable upregulation of the receptor on a single cell level, TEPP-46 did not clearly alter BMDM polarization. Still, CD39 was significantly upregulated on a single cell level in BMDM, which, in synopsis with the abovementioned changes in respiration and glycolytic turnover, indicates aberrations with regard to ATP generation, demand and secretion as a result of treatment with TEPP-46.

3.3 Implications of partial PKM2 knockdown *in vivo*

Myeloid cells constitute a flexible and versatile part of the immune system, partaking in inflammation, resolution of inflammation and wound repair (). While providing a useful model to study cellular effects *in vitro*, BMDM are artificially generated and therefore differ from their *in vivo* counterparts, especially lacking interaction with other (immune) cells in the organism. Also, *LysM* expression is not restricted to macrophages but can also be found in other cells of the myeloid lineage, such as hepatic Kupffer cells (He et al., 2013). Therefore, an examination of the effects of a partial PKM2 knockdown in other myeloid compartments was necessary. Since this project has been the first to use the described genetic approach to study the effects of PKM2 *in vivo*, mice and their livers were analyzed in homeostasis. In order to assess whether myeloid PKM2 plays a role in acute immune responses *in vivo*, $Pkm2^{\Delta myel}$ mice and their floxed counterparts were challenged with Concanavalin A (ConA) as a model of immune-mediated hepatitis (REF introduction).

3.3.1 $Pkm2^{\Delta myel}$ mice in homeostasis

To date, the genetic model and its implications on residual PKM2 expression have not been described or characterized (see also sections 3.1.1 and 3.1.3). As an initial step, $Pkm2^{\Delta myel}$ mice and their controls were examined at the age of 12 weeks with regard to general metabolic parameters, which are shown in Figure 14. $Pkm2^{\Delta myel}$ mice were substantially heavier than their controls ((a), 31.35g ±0,94 vs. 28.19g ±0.99, *p<0.05), corresponding to a difference of 11.21%. Similarly, livers of $Pkm2^{\Delta myel}$ were significantly

heavier ((b), 1.699g ±0.07 vs. 1.459g ±0.05, *p<0.05), equating to a difference of 16.45% between the genotypes. In homeostasis, there was no apparent difference between serum alanine aminotransferase (ALT) levels ((c), 59.95U/l ±22.43 in *Pkm2*$^{fl/fl}$ mice vs. 47.49U/l ±3.87 in *Pkm2*$^{\Delta myel}$ mice, not significant). Analyses of serum cholesterol and triglycerides, however, revealed remarkable differences between the groups. Sera of *Pkm2*$^{\Delta myel}$ mice contained almost double the amount of cholesterol compared to the control group ((d), 80.93mg/dl ±4.24 vs. 44.37mg/dl ±4.27, ***p<0.001). In an analogous manner, serum triglycerides were notably elevated in *Pkm2*$^{\Delta myel}$ mice, though this difference was not significant due to major variation within the group (see (e), 142.5mg/dl ±33.52 vs. 71.86mg/dl ±25.97, not significant).

In light of the clear differences in body and liver weight, qPCR of liver tissue was performed (see Figure 14(g), mRNA quantities are shown as fold changes compared to the benchmark of floxed controls). Cholesterol 7α-hydroxylase (*Cyp7a1*) marks the first and rate-limiting step of the synthesis of bile acids and is therefore crucial for cholesterol homeostasis. Strikingly, mRNA levels of the enzyme revealed a substantial increment in livers of *Pkm2*$^{\Delta myel}$ mice compared to floxed controls (2.03-fold ±0.13, *p<0.05). Carnitine palmitoyltransferase 1α (*Cpt1α*), a mitochondrial enzyme generating acyl carnitines and thus allowing long-chain fatty acids to be fueled into β-oxidation, turned out to also be significantly upregulated in the liver parenchyma of *Pkm2*$^{\Delta myel}$ mice (1.58-fold ±0.1, *p<0.05). mRNA for fatty acid synthase (*Fasn*), the metabolic counterpart to Cpt1α, was also upregulated (2.95-fold ±0.77, p=0.056), indicating both alterations in the degradation and the *de novo* synthesis of fatty acids. Another key player in lipid metabolism, sterol regulatory element binding factor 1 (*Srebf1*), involved in lipogenesis and the storage of fatty acids, happened to be upregulated on an hepatic mRNA level in *Pkm2*$^{\Delta myel}$ mice as well (1.88-fold ±0.28, *p<0.05). Interestingly, two key enzymes directly involved in the glycolytic pathway (glucose transporter 1 (*Glut1*) and lactate dehydrogenase A (*Ldha*)), showed no differences with regard to their mRNA level (1.45-fold ±0.14 and 1.05-fold ±0.13, not significant). Although being directly involved in *Ldha* regulation, hepatic hypoxia-induced factor 1α (*Hif1α*) mRNA levels were elevated in *Pkm2*$^{\Delta myel}$ mice (2.06-fold ±0.25, *p<0.05).

To gain a more detailed comprehension of the metabolic deviations apparent in *Pkm2*$^{\Delta myel}$ mice, ??? spectrometry was used to determine serum levels of different acyl carnitines. These metabolites (which are fatty acid esters of l-carnitine) are essential for the transport of fatty acids across the mitochondrial membrane and, lastly, for β-oxidation. Aberrations in acyl carnitine composition have been reported to indicate mitochondrial dysfunction, especially with reference to β-oxidation (Reuter and Evans, 2012). Furthermore, a link between NAFLD and elevated long-chain acyl carnitines in mice has been proposed recently (Bjørndal et al., 2018). Figure 14(f) depicts levels of several acyl carnitines in ascending number of carbon atoms of the acyl group. Since exact quantities vary physiologically, arbitrary units were chosen for the heatmap. Acyl carnitines were generally more abundant in sera of *Pkm2*$^{\Delta myel}$ mice. Still, especially long-chain acyl carnitines (C10 and greater) were remarkably elevated in comparison to the

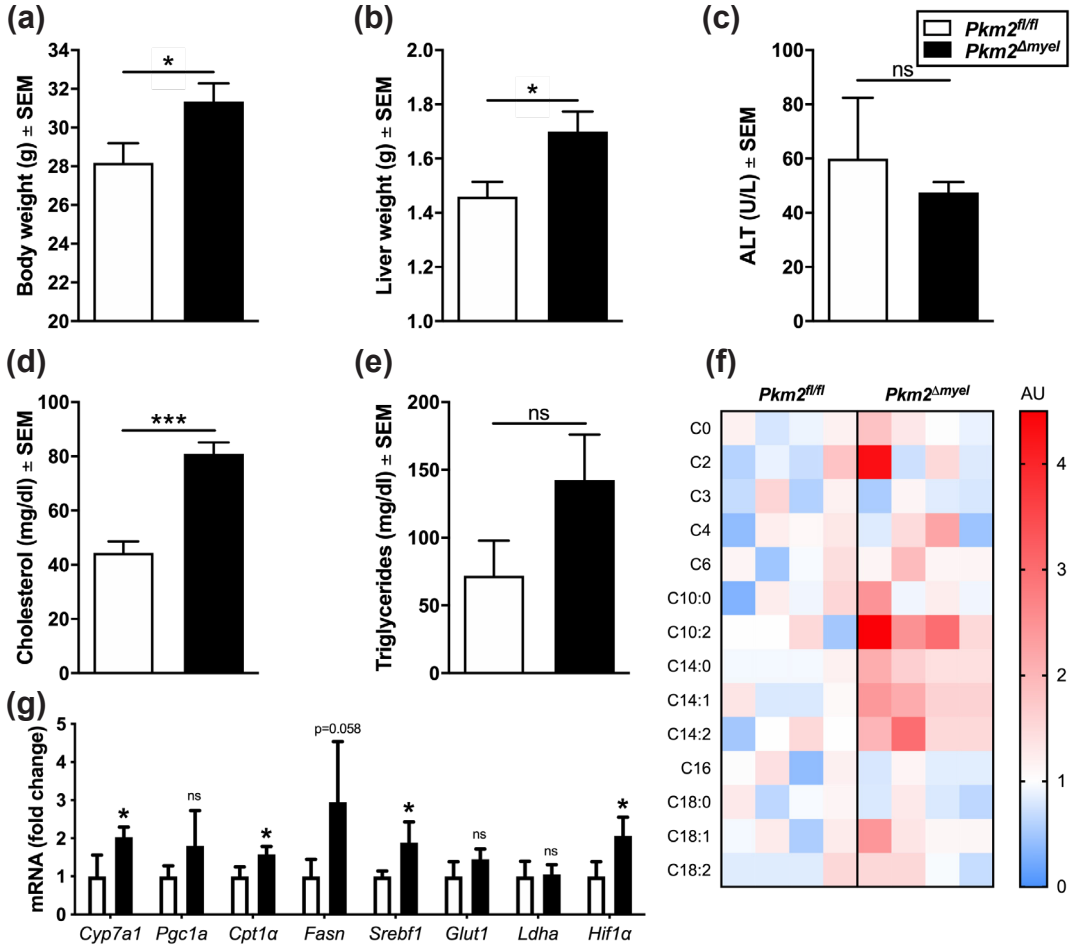

Figure 14: Consequences of partial myeloid PKM2 knockdown *in vivo*. 12-week old $Pkm2^{\Delta myel}$ mice and floxed controls were analyzed for general metabolic parameters. Body weight **(a)** and liver weight **(b)** in direct genotype comparison. Serum alanine aminotransferase (ALT) activities **(c)**, cholesterol **(b)** and triglycerides **(e)**. **(f)** Heatmap of serum acyl carnitine levels in ascending number of carbon atoms of the respective acyl group as determined by ??? spectrometry (AU = arbitrary units, see text for details). **(g)** Hepatic mRNA of key regulators of metabolism (shown as fold changes to floxed controls).

control group. This is of particular interest because of the inverse relationship between length of the carbon chain and free diffusion through the mitochondrial membrane, meaning that longer acyl-carnitines depend widely on the carnitine shuttle to carry out their physiological function as substrates for β-oxidation.

These results illustrate aberrant metabolic activities in the livers of $Pkm2^{\Delta myel}$ mice with regard to fatty acid oxidation, synthesis and storage, as well as their correlates within the blood stream (i.e. cholesterol, triglycerides, fatty acids and acyl carnitines). Myeloid PKM2 could therefore play a role in the development of an early stage of fatty liver disease.

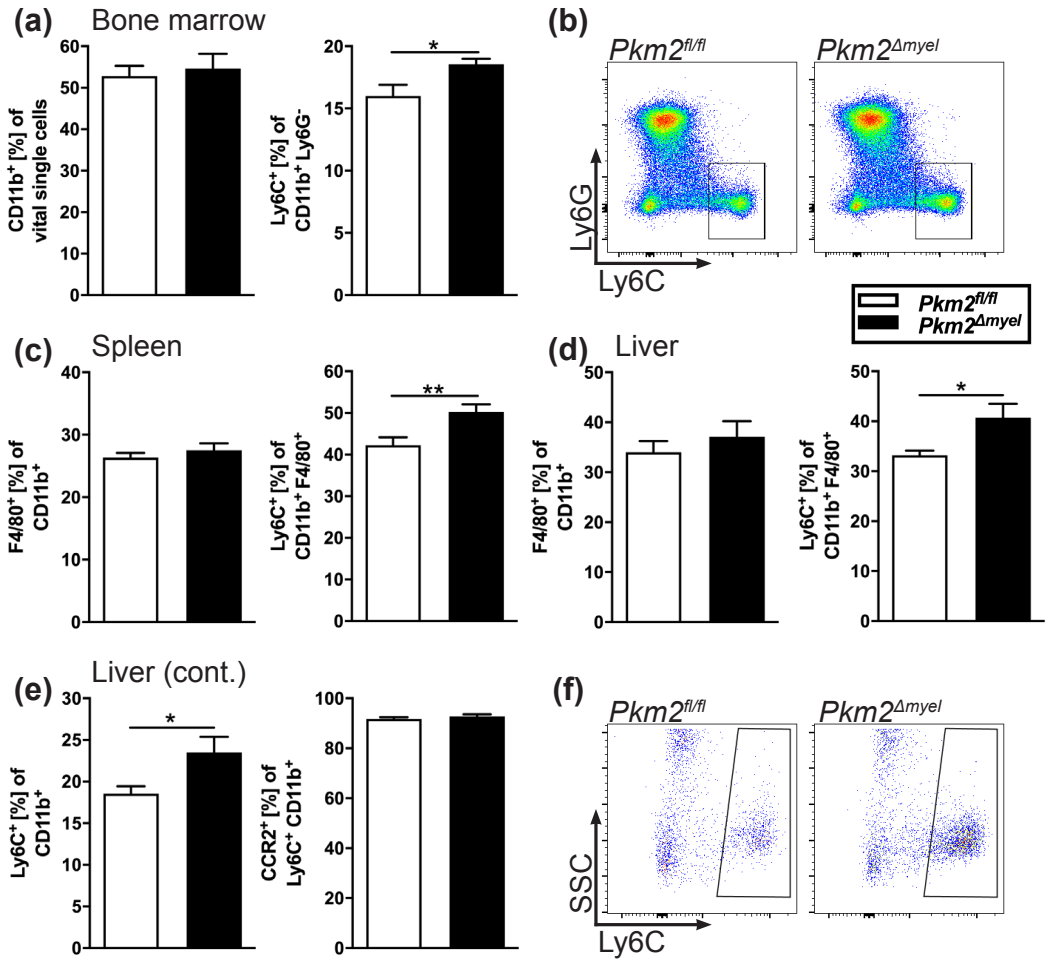

Figure 15: Examination of myeloid cellular compartments in *Pkm2*$^{\Delta myel}$ mice. (a) Relative quantities of myeloid marker CD11b (left) and monocytic marker Ly6C (right) in the bone marrow. **(b)** Representative dot plots of the Ly6C$^+$ CD11b$^+$ Ly6G$^-$ gate shown in (a), right bar graph. **(c)** Macrophage marker F4/80 (left) and monocytic marker Ly6C (right) within splenic myeloid cells. **(d)** Expression of F4/80 and Ly6C within hepatic myeloid cells. **(e)** Ly6C expression among all CD11b$^+$ cells in the liver (left), relative CCR2 expression of Ly6C$^+$ CD11b$^+$ cells (right). **(f)** Representative dot plots of the Ly6C$^+$ CD11b$^+$ gate shown in (e), left bar graph.

3.3.2 Cellular compartments in homeostasis

For the present study, three major cellular compartments were of particular interest with regard to their proportion of myeloid cells without further external intervention. Figure 15 shows the gating approach and the observed differences between both genotypes.

Analyses of the bone marrow as the primary source of myeloid cells showed no apparent differences in the proportion of cells positive for the pan-myeloid marker CD11b (a). However, Ly6C, a marker used for the identification of monocytes, was expressed more frequently within the myeloid cells of *Pkm2*$^{\Delta myel}$ BMDM (18.55& ±0.45 vs. 16.01% ±0.89, *p<0.05). The cell population in question was negative for Ly6G, ruling out an involvement of neutrophils (b). Interestingly, a significant

increase in Ly6C$^+$ cells was also observable among myeloid cells isolated from the spleen of *Pkm2*$^{\Delta myel}$ mice (see (c), 50.26% ±18.1 vs. 42.24% ±1.91, **p<0.01). The gating strategy of splenic myeloid cells also included F4/80 as a marker for mature macrophages, which did not show a difference between genotypes when analyzed solely. In addition, the composition of myeloid cells within nonparenchymal hepatic cells was studied ((d)-(f)). CD11b was stably detectable in approximately 5-10% of all NPC without genotype-specific differences (data not shown). Identically, F4/80 turned out to be comparably expressed, indicating no discrepancy between genotypes in the number of resident hepatic macrophages (see (d), left graph, 34.03% ±2.23 in *Pkm2*$^{fl/fl}$ mice vs. 37.13% ±3.09 in *Pkm2*$^{\Delta myel}$ mice, not significant). Ly6C, conversely, could be found on a significantly larger proportion of myeloid cells in the liver of *Pkm2*$^{\Delta myel}$ mice. This difference was visible with (see (d), right graph, 40.74% ±2.79 vs. 33.2% ±0.96, *p<0.05) and without (see (e), left graph, 23.49% ±1.88 vs. 18.55% ±0.9, *p<0.05) the inclusion of F4/80, pointing to a discrepancy in Ly6C expression which is independent of macrophage maturity. Figure 15(f) illustrates the aforementioned difference in hepatic myeloid Ly6C expression. These hepatic monocytes were also gated for CCR2 (see also section 3.2.4, elevated CCR2 expression on *Pkm2*$^{\Delta myel}$ BMDM). In this context, however, CCR2 turned out to be highly abundant on samples of either genotype (91.73% ±0.63 in *Pkm2*$^{fl/fl}$ mice vs. 92.71% ±0.91 in *Pkm2*$^{\Delta myel}$ mice, not significant). Very similar expression profiles were observed for programmed cell death 1 ligand 1 (PD-L1) on monocytes (data not shown), which was analyzed due to its suppressive effect on T lymphocytes (Carey et al., 2017). Still, *Pkm2*$^{\Delta myel}$ mice exhibited higher amounts of monocytes in their bone marrow, spleen and liver already in a steady state.

Apart from myeloid cells, lymphoid cells in *Pkm2*$^{\Delta myel}$ mice were examined, since aberrations in the myeloid compartment often influence the composition and marker expression of lymphoid cells. Therefore, spleens and livers were prepared as described, which were hence analyzed by flow cytometry (Figure 16). Livers of *Pkm2*$^{\Delta myel}$ mice showed a smaller proportion of CD4$^+$ cells within vital single cells than their controls ((a), 24.45% ±1.78 vs. 30.03% ±2.14, p=0.065). Splenic CD4$^+$ cells were similarly reduced (14.64% ±0.61 vs. 17.11% ±0.91, *p<0.05). CD8, which is predominantly expressed by cytotoxic T cells, was more abundant in livers of *Pkm2*$^{\Delta myel}$ mice (10.27% ±0.86 vs. 8.05% ±0.27, *p<0.05), whereas CD8 expression turned out to be similar among isolated splenocytes of *Pkm2*$^{\Delta myel}$ mice and their controls (see (b)). The reduction of CD4 expression among non-parenchymal cells within the liver was accompanied by a significant decrease in expression of CD25 (alias IL-2 receptor α chain), an established marker of T cell activation (Reddy et al., 2004). The proportion of CD25$^+$ cells among CD4$^+$ cells in *Pkm2*$^{\Delta myel}$ livers was greatly reduced (see (d), right graph, 49.48% ±2.31 vs. 62.1% ±1.93, ***p<0.001), as was mean fluorescence for this marker ((d), left graph, 346.3 ±17.81 vs. 434 ±30.02, *p<0.05). In light of a general diminution of hepatic CD4$^+$ cells and their reduced state of activation, programmed cell death protein 1 (PD-1) was measured, as expression of the co-inhibitory molecules limits the expansion of CD4$^+$ cells (Konkel et al., 2010). Indeed, hepatic CD4$^+$ cells of *Pkm2*$^{\Delta myel}$ mice exhibited

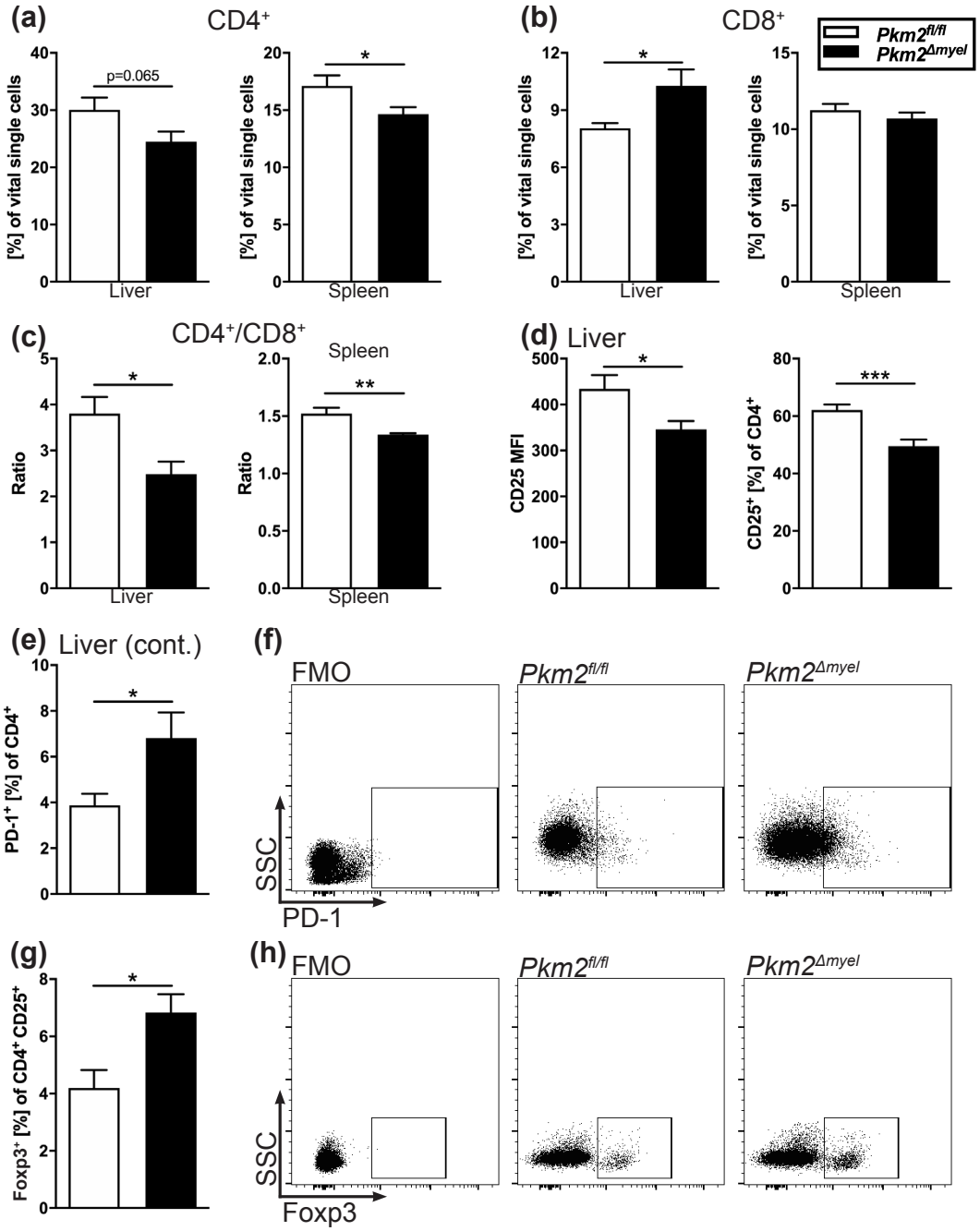

Figure 16: Examination of lymphoid cellular compartments in *Pkm2*$^{\Delta myel}$ mice. (a) Relative quantities of CD4$^+$ CD8$^-$ cells amongst vital single cells in liver and spleen. **(b)** CD8$^+$ CD4$^-$ cells as in (a). **(c)** CD4/CD8 ratio in liver and spleen. **(d)** CD25 MFI within the CD4$^+$ gate (left) and proportion of CD25$^+$ cells of CD4$^+$ cells (right). **(e)** PD-1 expression on CD4$^+$ cells and representative dot plots **(f)**. **(g)** Foxp3 expression on CD4$^+$CD25$^+$ cells and representatitve dot plots **(h)**.

a higher proportion of cells positive for PD-1 (see (e), 6.81% ±1.12 vs. 3.87% ±0.5, *p<0.05). This shift was verified by a FMO control and thus accurately measurable (see (f)). Furthermore, *Pkm2*$^{\Delta myel}$ mice were analyzed for hepatic regulatory T cells. Interestingly and despite the reduction of CD4 expression, the relative amount of cells

positive for Foxp3, the master transcription factor for regulator T cells, was increased in $Pkm2^{\Delta myel}$ mice on activated $CD4^+$ cells ((g), 6.83% ±0.64 vs. 4.19% ±0.63, *p<0.05). FMO controls validated this measurement (see (h)).

Taken together, these results suggest a crosstalk between the myeloid and lymphoid cellular compartment within the hepatic interface. This involves aberrations in hepatic metabolism, especially regarding a possible role of myeloid-associated dysfunction in the processing of lipids, that might ultimately alter the fate and composition of T cells in the liver.

3.3.3 Implications of partial PKM2 knockdown in ConA-mediated hepatitis

PKM2 has been reported to be highly upregulated in a broad variety of immune cells, such as macrophages, T cells and NK cells (Palsson-McDermott et al., 2015, Walls et al., 2020, Angiari et al., 2020), pointing out its non-canonical function within the cellular immune system. To date, whether preferential dimerization of the protein alters the outcome in immune-mediated hepatitis, remains unclear. In order to test this hypothesis, $Pkm2^{fl/fl}$ and $Pkm2^{\Delta myel}$ mice were challenged intravenously with Concanavalin A (ConA), a carbohydrate-binding protein, which is used as a model for immune-mediated hepatitis (Tiegs et al., 1992), at a dose of 5mg/kg. After 8 hours of ConA challenge, the mice were euthanized and subsequently analyzed. Figure 17 depicts exacerbated liver damage in $Pkm2^{\Delta myel}$ mice in comparison to the floxed controls. $Pkm2^{\Delta myel}$ mice showed massively elevated serum alanine aminotransferase (ALT) activities (see (a), 988.9U/l ±349.4 in $Pkm2^{\Delta myel}$ mice vs. 69.04U/l ±19.14 in $Pkm2^{fl/fl}$ mice, p=0.09), indicating extensive damage to the liver parenchyma. This observation was underlined by massive necrosis in livers of $Pkm2^{\Delta myel}$ mice, as shown in representative H&E stainings of liver sections (Figure 17(b)). Due to the substantial scatter of serum ALT values, the susceptibility towards ConA of mice of either genotype was assessed by nominal scaling. Mice with ALT levels above 75U/l were considered susceptible and thus labelled "responders", since ALT is liver-specific and thus indicates actual liver damage through enzyme release into the bloodstream. 75U/l marks a 2.5-fold increase compared to reference values for male C57BL/6 mice and was therefore chosen as a cut-off value (Otto et al., 2016). $Pkm2^{\Delta myel}$ mice were more likely to show substantial ALT elevations than their floxed counterparts (8 out of 13 individuals, 61.54% for $Pkm2^{\Delta myel}$ mice vs. 2 out of 6 individuals, 33.33% for $Pkm2^{fl/fl}$ mice, Figure 17(c)). To determine the influx of myeloid cells into the affected liver parenchyma, liver sections were stained for myeloperoxidase (MPO) by immunohistochemistry. MPO is expressed predominantly by neutrophilic granulocytes and monocytes, which release the enzyme as it generates the cytotoxic agent hypochlorous acid as part of their respiratory burst (Harrison and Schultz, 1976). After PBS injection, MPO^+ cells were only scarcely detectable within liver sections from both genotypes (20 cells/mm^2 ±6.3 in $Pkm2^{fl/fl}$ mice vs. 32.43 cells/mm^2 ±13.38). After 8 hours of ConA challenge, cell counts had increased

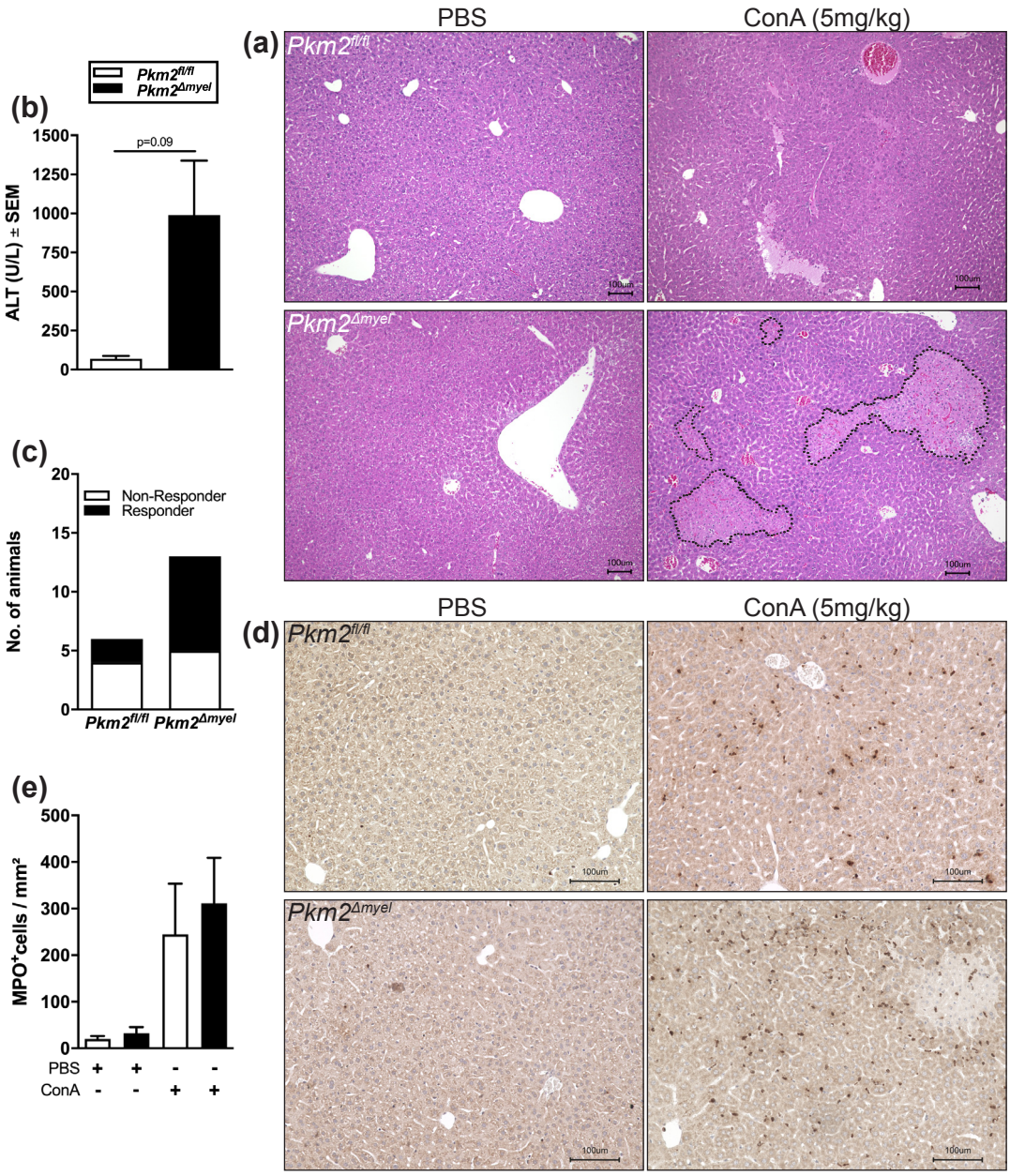

Figure 17: Effects of ConA-mediated liver injury. **(a)** Representative hematoxylin and eosin stainings of liver sections of $Pkm2^{fl/fl}$ mice and their controls. **(b)** Serum activity of alanine aminotransferase (ALT) 8h after i.v. ConA administration. **(c)** Susceptibility of $Pkm2^{\Delta myel}$ mice and controls towards ConA as indicated by a contingency plot (see text for details). **(d)** Quantification of myeloperoxidase (MPO) positive cells per mm^2 within liver sections after intravenous ConA administration. **(e)** Representative liver sections stained for MPO by immunohistochemistry.

remarkably (244.8 cells/mm^2 ±108.9 in $Pkm2^{fl/fl}$ mice vs. 310.9 cells/mm^2 ±97.85 in $Pkm2^{\Delta myel}$ mice), pointing to a pivotal involvement of myeloid cells in early stages of immune-mediated hepatitis. Further analyses of the liver parenchyma highlighted the role of myeloid-derived cytokines in the exacerbation of ConA hepatitis in $Pkm2^{\Delta myel}$ mice. As shown in Figure 18, mRNA levels of cytokines emblematic for M1 macrophage

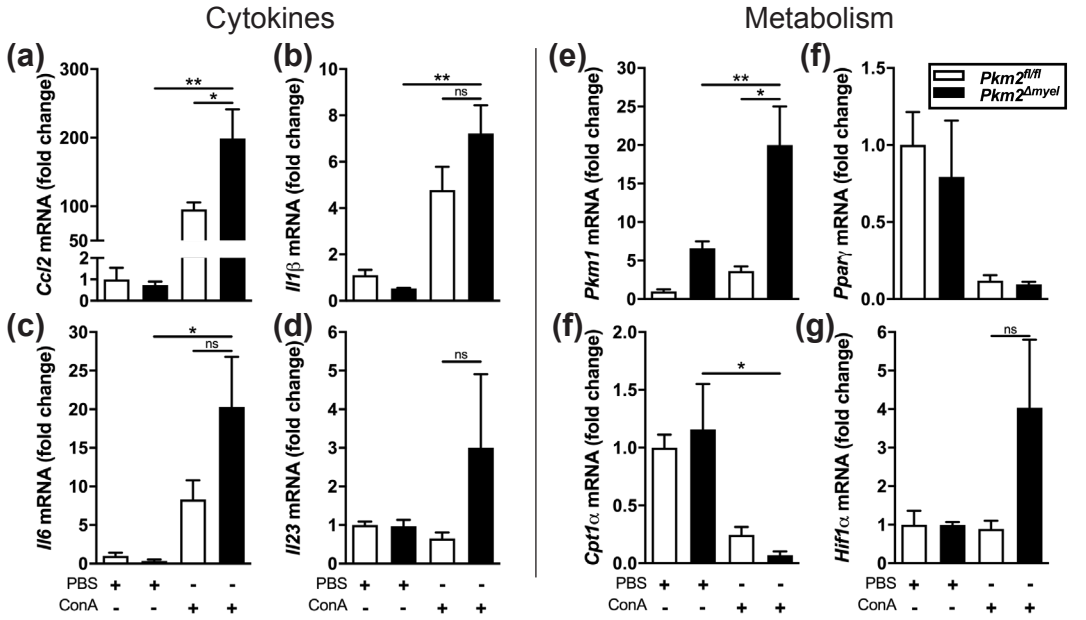

Figure 18: Impact of ConA-induced hepatitis on mRNA levels of cytokines and key metabolic enzymes in the liver. Livers were extracted from $Pkm2^{\Delta myel}$ and $Pkm2^{fl/fl}$ mice and subsequently analyzed by qPCR. Changes in mRNA quantities are shown as fold changes in comparison to controls treated with PBS. Left (a)-(d): *Ccl2* **(a)**, *Il1*β **(b)**, *Il6* **(c)** and *Il23* mRNA **(d)**. Right (e)-(h): *Pkm1* **(e)**, *Ppar*γ **(f)**, *Cpt1*α **(g)** and *Hif1*α mRNA **(h)**.

polarization were markedly upregulated in livers of $Pkm2^{\Delta myel}$ mice 8 hours after the administration of ConA. *Ccl2* mRNA was highly abundant in livers of $Pkm2^{\Delta myel}$ mice after ConA challenge compared to PBS treated mice (199-fold ±42.37 vs. 0.74-fold ±0.16, **p<0.01). Furthermore, *Ccl2* turned out to be significantly elevated compared to $Pkm2^{fl/fl}$ mice after ConA (199-fold ±42.37 vs. 95.54-fold ±10.06, *p<0.05), which is in line with data obtained from the abovementioned analyses of $Pkm2^{\Delta myel}$ BMDM (see Figures 8 and 9). *Il1*β mRNA was also increased after ConA exposure in comparison to PBS treated individuals (4.78-fold ±1 vs. 1-fold ±0.22 in $Pkm2^{fl/fl}$ mice, not significant, 7.22-fold ±1.22 vs. 0.53-fold ±0.03 in $Pkm2^{\Delta myel}$ mice, **p<0.01), although there was no statistically significant difference in comparison of the genotypes. Similar effects were observable for *Il6* (8.32-fold ±2.49 in ConA-treated vs. 1-fold ±0.44 in PBS-treated $Pkm2^{fl/fl}$ mice, not significant; 20.32-fold ±6.47 in ConA-treated vs. 0.37-fold ±0.18 in PBS-treated $Pkm2^{\Delta myel}$ mice, *p<0.05). Interestingly, mRNA levels of *Il23*, a myeloid-derived cytokine involved in expansion and maintenance of Th17 responses, were solely upregulated in livers of $Pkm2^{\Delta myel}$ mice treated with ConA compared to the PBS group (3.01-fold ±1.9 vs. 0.97-fold ±0.16, not significant), whereas no upregulation of *Il23* was detectable in floxed animals after ConA (0.65-fold ±0.15 vs. 1-fold ±0.09, not significant).

The deviations in susceptibility towards ConA and the resulting cytokine levels were accompanied by notable changes in hepatic mRNA levels of key players of metabolism (Figure 18 (e)-(h)). The induction of glycolytic genes is largely controlled by *Hif1*α

expression (Semenza et al., 1994, Semenza et al., 1996), whose mRNA levels were notably elevated after ConA treatment in livers of $Pkm2^{\Delta myel}$ mice (4.04-fold ±1.77 vs. 0.89-fold ±0.21 in $Pkm2^{fl/fl}$ mice, not significant). ConA exposure markedly boosted the expression of *Pkm1*, one of the three rate-limiting steps of glycolysis. This effect was observable already in a steady state (see (e), 6.6-fold ±0.89 in $Pkm2^{\Delta myel}$ mice vs. 1-fold ±0.27 in $Pkm2^{fl/fl}$ mice, not significant), though acute hepatitis aggravated this increase (20-fold ±5.04 in $Pkm2^{\Delta myel}$ mice vs. 3.63-fold ±0.6 in $Pkm2^{fl/fl}$ mice, *p<0.05). Of note, Pkm2 mRNA was also upregulated upon ConA stimulation in the livers of both $Pkm2^{fl/fl}$ and $Pkm2^{\Delta myel}$ mice, though the latter substantially failed to exploit the physiological magnitude of this inflammatory response (data not shown). This could explain the rise of *Pkm1* mRNA to be a compensatory mechanism in $Pkm2^{\Delta myel}$ mice. Simultaneously, *Cpt1α* was significantly downregulated upon exposure to ConA in $Pkm2^{\Delta myel}$ livers, suggesting a decrease in oxidative metabolism of fatty acids (0.07-fold ±0.03 vs. 1.16-fold ±0.39 in the PBS group, *p<0.05). However, a decline was also visible in $Pkm2^{fl/fl}$ mice, though to a lesser degree (0.25-fold ±0.07 vs. 1-fold ±0.11, not significant). *Pparγ* was also examined because of its role as master regulator of lipid storage (REF). ConA hepatitis lead to a clear reduction in *Pparγ* mRNA, though there were now observable differences between the genotypes.

In summary, the data suggest an aggravation of ConA-mediated hepatitis due to an excacerbation of key myeloid-derived cytokines in the livers of $Pkm2^{\Delta myel}$ mice. Furthermore, the qPCR results demonstrate a metabolic shift towards an anaerobic metabolic state in the inflamed liver, which was found to be more pronounced in $Pkm2^{\Delta myel}$ mice.

3.3.4 Effects of PKM2 activation prior to administration of ConA

Endogenous and exogenous agents have been reported to impact the quarternary structure of PKM2. PKM2 activators have been studied since the beginning of the 21^{st} century, two of which have been used frequently to activate PKM2 in various contexts: A sulfonamide derivate (DASA-58, Boxer et al., 2010) and a pyridazinone (TEPP-46, Jiang et al., 2010). These small molecules induce tetramer formation of PKM2 and thereby increase its catalytic activity. Consequently, less dimeric PKM2 is present intracellularly, which could enter the nucleus and regulate genetic transcription of glycolytic genes and proinflammatory mediators (Luo et al., 2011, Palsson-McDermott et al., 2015).

Since $Pkm2^{\Delta myel}$ mice sustain a shift towards dimeric PKM2 in their myeloid cellular compartment and thus present aggravated cellular damage in immune-mediated hepatitis, inhibition of this shift and subsequent induction of tetrameric PKM2 might be beneficial in this context. To test this hypothesis, $Pkm2^{\Delta myel}$ mice were either treated with intravenous ConA at a dose of 5mg/kg body weight or treated intravenously with TEPP-46 (50mg/kg) one hour prior to administration of ConA. The ensuing evaluation is displayed in Figure 19. ConA administration lead to a clear increase in ALT levels compared to PBS injection (see (b), 988.9U/l ±349.4 vs. 12.39U/l

±1.73, not significant). Pretreatment with TEPP-46 mitigated the enzyme release into the bloodstream, indicating reduced liver damage (167.9U/l ±74.19, not significant in comparison to sole ConA injection). However, ALT levels were still higher than the reference value (Otto et al., 2016), proving correct administration of ConA. As mentioned, *Pkm2*$^{\Delta myel}$ mice exhibit higher amounts of myeloid cells in homeostasis and acute liver inflammation (Figures 15 and 17) which are likely to contribute to the aggravation of ConA hepatitis in this model. TEPP-46 reduced the amount of MPO^{+} cells which infiltrated the liver upon ConA exposure in comparison to the ConA group (see (c), 137.2 cells/mm^2 ±0.25 vs. 186.6 cells/mm^2 ±10.14, p=0.081), which is illustrated in (d).

Next, a possible involvement of TEPP-46 in the transcription of M1-typical cytokines was assessed by qPCR (Figure 19(e)-(h)). Again, key M1-related cytokines were notably elevated after ConA treatment in *Pkm2*$^{\Delta myel}$ compared to mice treated with PBS and *Pkm2*$^{fl/fl}$ mice treated with ConA. *Ccl* mRNA was significantly upregulated in livers of *Pkm2*$^{\Delta myel}$ mice, whereas pretreatment with TEPP-46 substantially reduced this increment in *Ccl2* mRNA to levels comparable with *Pkm2*$^{fl/fl}$ individuals (0.0345 ±0.0134 [pretreated *Pkm2*$^{\Delta myel}$ mice] vs. 0.0793 ±0.0177 [*Pkm2*$^{\Delta myel}$ mice without pretreatment], *p<0.05; 0.0358 ±0.0057 in *Pkm2*$^{fl/fl}$ mice treated without pretreatment). The same effect of the pretreatment in *Pkm2*$^{\Delta myel}$ mice was observable for *Il1*β (0.002 ±0.0008 vs. 0.0042 ±0.0007, not significant) and *Il6* (5.21×10^{-5} ±8.27×10^{-6} vs. 2.84×10^{-4} ±1.25×10^{-4}, not significant). An increase in *Il23* was completely reverted by TEPP-46 pretreatment (1.78×10^{-4} ±5.59×10^{-5} vs. 6.16×10^{-5} ±2.54×10^{-5} in the pretreated group, not significant). Interestingly, changes in mRNA of metabolic players like *Pkm1* and *Cpt1*α due to acute onset hepatitis did not change notably in the context of PKM2 activation by TEPP-46 (see Figure 19 (j) and (l)). However, TEPP-46 administration did indeed cause a decrease in *Hif1*α mRNA (0.0026 ±0.0001 in the pretreated group vs. 0.0143±0.0071 in the ConA group, not significant), which points to a regulatory framework in transcription of glycolytic and respiratory enzymes without direct involvement of HIF1α in acute ConA hepatitis.

In addition to its effect on pro-inflammatory cytokines, transcription related to the NLRP3 inflammasome was also dampened by TEPP-46. Hepatic *Nlrp3* mRNA levels were elevated in *Pkm2*$^{\Delta myel}$ mice after ConA injection (2.93×10^{-4} ±6.69×10^{-5} vs. 6.33×10^{-5} ±6.97×10^{-6}, *p<0.05), but could again be reduced to levels comparable with floxed individuals when injected with TEPP-46 prior to ConA (1.95×10^{-4} ±5.23×10^{-5} for *Pkm2*$^{\Delta myel}$ mice pretreated with TEPP-46 vs. 1.93×10^{-4} ±2.36×10^{-5} for *Pkm2*$^{fl/fl}$ mice treated solely with ConA). This finding is in accordance with differences in Caspase 1 abundance in the inflamed livers of ConA treated mice and individuals pretreated with TEPP-46 (19(b)). The latter exhibited less cleavage of pro-Caspase 1 to its mature form, which was illustratively visualized by immunohistochemistry. As another element involved in the activation and assembly of the NLRP3 inflammasome, liver sections were stained immunohistochemically for high mobility group box 1 (HMGB1, see Figure 20). The protein is physiologically located in the nucleus but serves as an endogenous

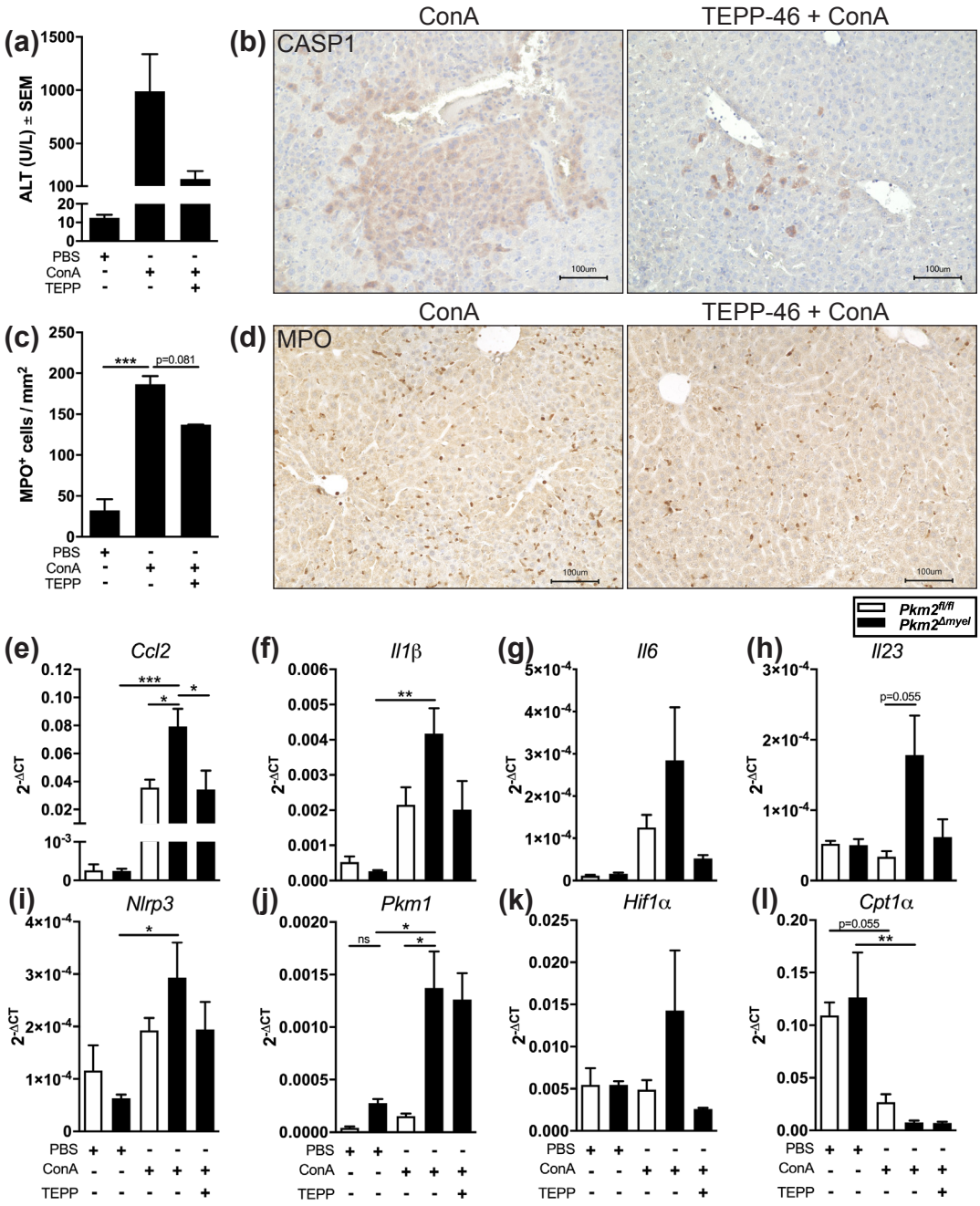

Figure 19: Impact of pharmacological PKM2 activation by TEPP-46 prior to ConA treatment. **(a)** Serum ALT activities 8 hours after i.v. ConA administration with or without 1 hour of i.v. TEPP-46 pretreatment. **(b)** Representative liver sections of $Pkm2^{\Delta myel}$ mice (treated as in (a)) stained for Caspase 1 (CASP1) by immunohistochemistry. **(c)** Quantification of MPO^+ cells per mm^2 within liver sections of mice treated as indicated. **(d)** Representative liver sections of $Pkm2^{\Delta myel}$ mice stained for MPO by immunohistochemistry. **(e)**-**(l)**: mRNA levels shown as $2^{-\Delta CT}$ to ensure comparability between two independent experiments. $Pkm2^{fl/fl}$ and $Pkm2^{\Delta myel}$ mice were injected with PBS or ConA 8 hours before organ extraction and subsequent analyses. $Pkm2^{\Delta myel}$ mice were additionally treated with TEPP-46 before ConA adminstration as in (a). Results of qPCR for *Ccl2* **(e)**, *Il1*β **(f)**, *Il6* **(g)**, *Il23* **(h)**, as well as *Nlrp3* **(i)**, *Pkm1* **(j)**, *Hif1*α **(k)** and *Cpt1*α **(l)**.

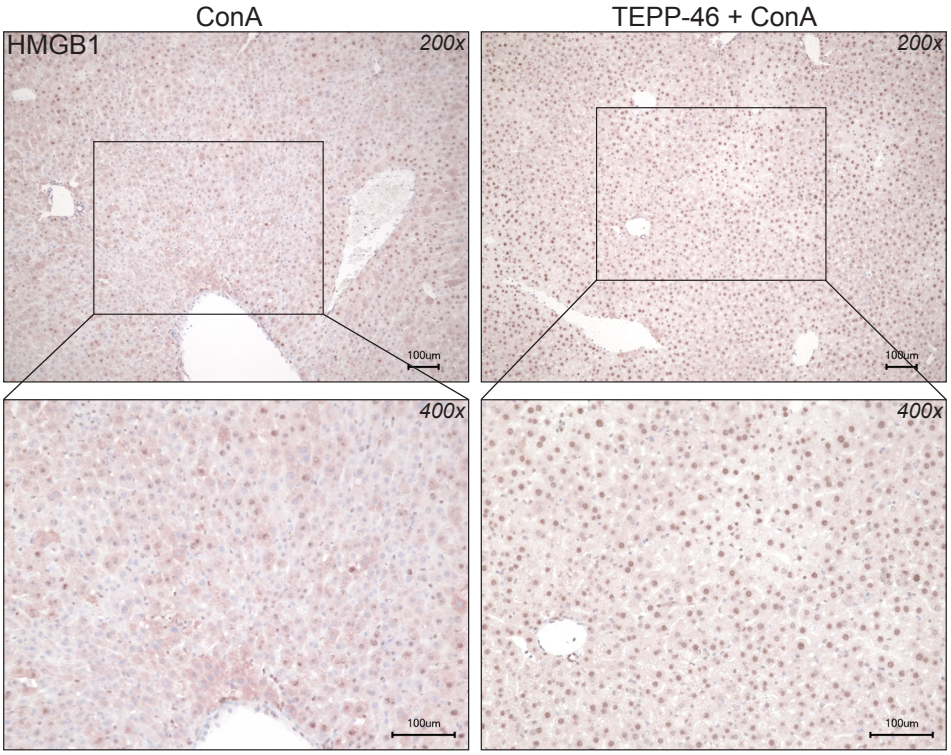

Figure 20: Pharmacological activation of PKM2 and its influence on the subcellular localization of high mobility group box 1 (HMGB1). Liver sections of *Pkm2*$^{\Delta myel}$ mice were immunohistochemically stained for HMGB1 after 8 hours of ConA exposure (left) and 1 hour of additional pretreatment with TEPP-46 (right). Upper row: 200-fold magnification, bottom row: Insets, 400-fold magnification.

alarmin once it is hyperacetylated and translocates to the cytosol. HMGB1 can be actively secreted by macrophages (Wang et al., 1999), but it also acts as a danger signal of hepatocytes in ConA hepatitis (Tu et al., 2013). Upon ConA exposure, liver sections of *Pkm2*$^{\Delta myel}$ mice showed a pronounced cytoplasmatic staining, indicating a translocation of HMGB1 from the nucleus into the cytosol in response to ConA (left images). Nuclear HMGB1 staining turned out to be faint and left the nuclear counterstaining with hematoxyline clearly visible. Conversely, pretreatment of the mice with TEPP-46 before ConA injection resulted in a prominent nuclear HMGB1 signal, which covered the majority of counterstained nuclei, whereas the hepatic cytosol remained largely unstained (right images). These data suggest a possible involvement of myeloid PKM2 activation in ameliorating pyroptosis during immune-mediated hepatitis.

Altogether, pharmacological activation of PKM2 protected *Pkm2*$^{\Delta myel}$ mice from excessive liver damage with regard to serum ALT levels, the influx of myeloid cells, pro-inflammatory cytokines and inflammasome-associated pyroptosis. TEPP-46 furthermore reduced *Hif1*α transcription, while leaving genes related to glycolysis and β-oxidation largely unaffected.

4 Discussion

The aim of the present study was to characterize the impact of a myeloid-specific knock-down of PKM2 on their cellular immune responses in mice. As demonstrated in section 3.1.1 and discussed in sections 4.1, 4.1.2 and 4.1.1, the *Cre*-mediated knock-down of PKM2 was incomplete and caused significant aberrations in the balance of PKM isoforms and PKM2 oligomerization in particular.

For an evaluation of this partial PKM2 knock-down in myeloid cells, BMDM were chosen as an established model to study the differentiation of macrophages, their metabolism and their immunological properties. The experimental setup for BMDM comprised mainly of exposure of a BMDM mono-culture to polarizing and/or stimulating agents and subsequent analyses for the parameters mentioned above. Still, since these conditions pose a highly artificial environment for macrophages without the interaction with other cell types and in exposure to non-physiological environmental conditions, additional experiments were performed to study the effects of the murine genotype *in vivo*. This translational approach was chosen to provide for a more physiological experimental system, in which the effects of a partial PKM2 knock-down were hence analyzed.

4.1 Incomplete *Cre*-mediated knock-down of PKM2 in myeloid cells

The Cre-loxP system, whose genetic principles were first described by Sternberg in the early 1980s, is considered a powerful tool to study the effects of cell-specific genetic alterations (Sternberg and Hamilton, 1981). To this date, it is widely used in fundamental research because of its versatility and its (theoretically) straight forward approach to modify only a certain set of cells by employing cell type-specific promotors to activate *Cre*.

Due to its established role in research over the last 30 years, it has become clear that designing a genetic construct using the Cre-loxP system might contain pitfalls, which can render the interpretation of data more difficult than initially expected. In the present work, mice with homozygous *loxP* sites around PKM2-specific exon 10 were crossed with mice carrying a heterozygous *Cre* recombinase downstream the myeloid *LysM* promotor in order to achieve a myeloid-specific knock-down of the enzyme (Figure 4). Mice homozygous for *Cre* showed a more efficient reduction of *Pkm2* mRNA (Figure 5). However, since lysozyme plays an integral role in the myeloid immune response, a heterozygous knock in of *Cre* was chosen in order to preserve one intact allele and to avoid a possible confounder in experimental models of inflammation. As described, the knockout of PKM2 on a protein level in this model turned out to be incomplete; although exhibiting significantly reduced levels of PKM2 (-33% to XYZ%, depending on the analysis), BMDM derived from $Pkm2^{\Delta myel}$ mice still showed detectable remnants of PKM2 protein in all measurements.

There are various possible explanations for this observation. Previous studies have found inconsistent *Cre* recombination in littermates due to spontaneous ectopic

recombination and concomitant removal of *loxP* sites *in vivo* (Eckardt et al., 2004). Incomplete recombination has also been attributed to *Cre* mosaicism, meaning that the recombinase might not be active in a proportion of the targeted cells (Heffner et al., 2012). However, the first study on the utilization of a murine *LysM-Cre* model by Clausen reported a deletion of the target protein in 95% of peritoneal macrophages and 99% of peritoneal neutrophilic granulocytes, with no significant deletion in T and B cells and only a modest reduction of 16% in dendritic cells (Clausen et al., 1999), indicating a satisfactory recombination efficacy and target accuracy of *LysM-Cre*. Another, more recent publication addressed the issue of *Cre* efficacy in different strains targeting myeloid subsets (Abram et al., 2014). The authors crossed various myeloid-*Cre* strains with ROSA-EYFP reporter mice and analyzed the reported expression of the recombinase by flow cytometry. *LysM-Cre* mice showed EYFP expression in approx. 50% of inflammatory monocytes and 70% in polymorphonuclear leukocytes (which contains neutrophilic, basophilic and eosinophilic granulocytes as well as mast cells). For macrophage populations, these results varied widely depending on their location (approx. 100% in alveolar, 90% in peritoneal and 40% in splenic macrophages). Unfortunately, neither BMDM nor liver-resident macrophages were not included in this study, leaving room for speculation on these particular myeloid cellular subsets. Incomplete deletion of a target protein by *LysM-Cre* can furthermore differentiate macrophage subsets according to the activity of their *LysM* promotor, as has been demonstrated previously (Vannella et al., 2014). In addition to these observations regarding *LysM-Cre*, it is conceivable that promotor and recombinase might not be the only players in this phenomenon since the position of the *loxP* sites influences the efficacy on of recombination to a substantial extent (Vooijs et al., 2001). In light of these reports, more than one isolated reason might explain why *Cre*-mediated recombination in the present model turned out to be incomplete.

4.1.1 Reduction of PKM2 leads to compensatory upregulation of PKM1 in myeloid cells

The PKM gene encodes for two different isoforms, PKM1 and PKM2, through alternative splicing by exclusively including either exon 9 or 10, respectively. This process is tightly controlled by RNA binding proteins such as heterogeneous nuclear ribonucleoprotein (hnRNPA) 1 and 2, as well as polypyrimidine tract binding protein (PTB), whose transcription is in turn controlled by c-Myc, a transcription factor and proto-oncogene (David et al., 2010). In macrophages, both isoforms are expressed in homeostasis, but an increase in protein expression has only been reported for PKM2 in response to LPS (Palsson-McDermott et al., 2015). Due to the imperative role of glycolysis in macrophage function, we hypothesized that nullifying the cells' ability to upregulate PKM2 might result in a compensatory off-target effect. Indeed, PKM2-deficient BMDM showed strikingly elevated levels of PKM1 expression (approx. 30-fold in comparison to controls, Figure XYZ), pointing to a possible mechanism to bypass the last rate-limiting step

of glycolysis. This effect was not restricted to stimulated conditions, but was already visible in untreated cells. This observation supports the notion that macrophages rely strongly on glycolysis as their main source of ATP regeneration (Rodríguez-Prados et al., 2010).

Interestingly and in contrast with the study mentioned above, stimulation with LPS did not lead to a significant increase in total PKM1 or 2 protein. It did, however, remarkably induce dimerization of PKM2, especially in BMDM derived from $Pkm2^{\Delta myel}$ mice (see section 4.1.2). Furthermore, the study by Pålsson and colleagues does not comment on the possible effects a compensatory increase in PKM1 expression might have on the proposed accumulation of upstream glycolytic intermediates, which should be considered concerning the high enzymatic turnover of PKM1. Especially in the context of a low concentration of endogenous activators like FBP, both isoforms show comparable substrate affinity (K_m), whereas the V_{max} of PKM1 is twofold *higher* than that of PKM2 (Liu et al., 2020). In this context, the present study sheds light on the flexibility of macrophages in order to maintain a key metabolic pathway and to balance the glycolytic flux when PKM2 expression is not available at physiological levels.

4.1.2 Preferential dimerization of residual PKM2 in $Pkm2^{\Delta myel}$ BMDM

While PKM1 is regarded a highly catabolic enzyme in a stable homo-tetrameric form of subunits with few endogenous regulators, PKM2 has been reported to exist in an equilibrium of enzymatically inactive monomers/dimers and highly active tetramers (Morgan et al., 2013). Here, we report a significant influence of reduced total PKM2 protein levels on the quarternary structure of its remnants in BMDM of $Pkm2^{\Delta myel}$ mice. Phospho-PKM2 (Y105) was found to be substantially more abundant in $Pkm2^{\Delta myel}$-derived BMDM. In homeostasis and after stimulation with LPS, levels of dimeric PKM2 were 2 to 3-fold higher in comparison to control animals (Figure 6(c) and (d)), while total PKM2 protein was significantly reduced (Figure 5). Additionally, tetrameric PKM2 was observed to be decreased in $Pkm2^{\Delta myel}$ BMDM. Due to the antagonistic properties of monomeric/dimeric and tetrameric PKM2, we hypothesized that a net decrease of PKM2, accompanied by a larger proportion of dimeric PKM2 might alter the phenotype of BMDM towards a more pronounced inflammatory response (see section 4.2).

The equilibrium of PKM2 oligomers has been shown to be tightly regulated depending on, among other things, the cell's energy demand. PKM2 can be modified by a variety of post-translational modifications, such as phosphorylation, acetylation, hydroxylation, oxidation, ubiquitination, glycosylation, methylation and succinylation at different amino acid residues (Prakasam et al., 2018, Wang et al., 2017). Although the mechanisms and pathways that ensue from these modifications differ considerably, their unifying feature is PKM2 dimerization and subsequent translocation into the nucleus. In tumor cells, the main aim of PKM2 nuclear translocation is to accelerate the cell cycle and to induce transcription of genes which encode for glycolytic enzymes, such as LDHA,

GLUT-1 and also PKM2 itself (Hitosugi et al., 2009). A possible explanation for preferential dimerization in *Pkm2*$^{\Delta myel}$ BMDM might simply be a dose-effect due to the partial knock-down: If the total protein amount is reduced, a stable rate of phosphorylation and subsequent dimerization would convincingly account for a higher proportion of dimeric PKM2. Additionally and in consideration metabolic deviations in *Pkm2*$^{\Delta myel}$ BMDM discussed in section 4.2.2, other factors might contribute to the observed increase in dimeric PKM2. BMDM derived from *Pkm2*$^{\Delta myel}$ mice have shown higher basal O_2 consumption and extracellular acidification, pointing to a generally increased flux through glycolysis and oxidative phosphorylation (Figures 10 and 11). Concomitantly, an increase in proton leakage was measured, both of which suggest an increased production of ROS as a by-product of mitochondrial respiration (Murphy, 2009). ROS have been reported to initiate intracellular kinase pathways such as SRC, which in turn phosphorylate PKM2 and thus induce PKM2 dimerization (Heppner et al., 2018, Eigenbrodt et al., 1992, Zhou et al., 2018). Furthermore, the exact mechanism that leads to phosphorylation at Y105 by FGFR1 and to subsequent dimerization of PKM2 (Hitosugi et al., 2009), has very recently also been linked to excessive production of ROS (Glorieux et al., 2021).

Apart from a preferential dimerization of residual PKM2 in *Pkm2*$^{\Delta myel}$ BMDM, we observed a reduced amount of tetrameric PKM2 in comparison to controls (Figure 6(a) and (b)). Tetrameric PKM2 remains in the cytosol and has enzymatic properties similar to those of PKM1 (Liu et al., 2020). The formation of homotetramers is regulated by the presence of intracellular mediators, first and foremost by FBP (Ashizawa et al., 1991). This central glycolytic intermediate is generated by phopshorylation of F6P by PFK1, a key regulatory enzyme upstream of pyruvate kinase. Depending on the cell's energy demand, PFK1 is inhibited by ATP and lactate (which are abundant when energy depots are full) and is stimulated when the cell is running low on ATP. We found, that *Pkm2*$^{\Delta myel}$ BMDM are actually more metabolically active, as they exhibit greater rates of glycolysis and ATP-linked respiration (Figure 10(a)-(c)). In conjunction with the extensive upregulation of highly active PKM1 in BMDM (Figure XYZ), the excess in energy sources might could contribute to lower levels of FBP, thereby impeding the formation of PKM2 tetramers. In addition to FBP, accumulation of SAICAR (an intermediate of purine synthesis) has also been identified to promote PKM2 tetramerization in a nutrient-limited environment (Keller et al., 2012). Conversely, lower levels of SAICAR might destabilize tetrameric PKM2 once nutrients are plenteously available.

Altogether, the present work points to a differentially regulated balance of PKM isoforms and PKM2 oligomers within the regulatory framework of the metabolic flux and adjacent pathways (i.e. ROS and nucleotide synthesis) in macrophages. The results suggest an antecedently underestimated role of PKM1, which could compensate for the kinetic deficiency of PKM2, as well as a complex equilibrium of dimeric and tetrameric PKM2 which is conceivably affected by PKM1 upregulation and concurrent deviations of the metabolic flux in *Pkm2*$^{\Delta myel}$ BMDM.

4.2 Phenotypical characterization of *Pkm2*$^{\Delta myel}$ derived BMDM

Myeloid cells as the forerunners in inflammation can respond quickly towards inflammatory agents. Although being less proliferative than T cells, granulocytes, dendritic cells, monocytes and macrophages exert their defensive powers through rapid induction of effector molecules, such as cytokines, surface molecules or ROS. The synthesis of these effector molecules requires efficient mechanisms to divert metabolic intermediates into biomass-generating pathways upon stimulation. Macrophages rely heavily on glycolysis and convert the vast majority of it into lactate, especially when activated by TLR ligands like LPS, IFNγ or lipoteichoic acid (Rodríguez-Prados et al., 2010). PKM2 as the most downstream key regulatory enzyme of glycolysis plays a major role in this regulatory framework, since its regulatory flexibility enables the cell to meet its metabolic and molecular demands, depending on its state of activation and has thus been examined with regard to macrophage effector functions *in vitro*. The aim of this work was to characterize macrophages deficient in PKM2 expression, as well as the consequences that arise from PKM2-deficient macrophages for the entire organism.

4.2.1 *Pkm2*$^{\Delta myel}$-derived BMDM tend towards a more pro-inflammatory cytokine profile

In light of the unexpected results of PKM isoforms and oligomer formation mentioned before, we hypothesized that preferential dimerization of PKM2 could trigger a pro-inflammatory phenotype of *Pkm2*$^{\Delta myel}$ BMDM. Previous reports have demonstrated a direct interaction between PKM2 and Hif1α in BMDM, which leads to an increase in IL-1β transcription. Conversely, inducible *Cre*-mediated PKM2 knockout abrogated this response (Palsson-McDermott et al., 2015). In accordance with the abovementioned observations of an incomplete PKM2 knock-down and concomitant preferential dimerization of PKM2 remnants, *Pkm2*$^{\Delta myel}$ BMDM tended to a more pronounced transcription of genes related to pro-inflammatory (M1) cytokines like *Il1*β, *Il6* and *Ccl2* when compared to their controls (Figure 8). However, difference between the genotypes turned out to be rather discreet and did not reach significance in the experimental group. Similarly, there were no significant differences for TNFα when analyzed on a protein level (Figure 9(a)). CCL2 was analyzed due to its upregulation in myeloid cells in the context of inflammatory stimuli; apart from inducing myeloid chemotaxis, it is known to amplify M1 cytokine secretion and to induce the release of ROS (respiratory burst) in monocytes (Gschwandtner et al., 2019). Surprisingly, high concentrations of the chemokine were detectable in the supernatants of BMDM from both genotypes (Figure 9(b)). However, the experimental setup of BMDM maturation and differentiation included the use of a cell culture medium extracted from L929 fibroblasts (see also section 2.2.12). Despite its established role in macrophage research, this supernatant has only very recently been reported to contain, among 2192 other proteins, substantial amounts of CCL2 (Heap et al., 2020). The measured concentrations for the cytokine are thus likely to comprise of the intrinsic concentration of the medium as well as the proportion secreted

by the BMDM in the cell culture. Still, it is notable that *Pkm2*$^{\Delta myel}$ BMDM showed higher CCL2 concentrations in all groups of treatment, suggesting a higher production of the cytokine in comparison to controls. This is of particular interest because PKM2 has been reported to induce CCL2 expression in colorectal cancer via NF-κB signalling (Zou et al., 2017); to date, a similar regulation of CCL2 expression in macrophages has not yet been described.

On the other end of the spectrum, IL-10 was determined concerning its emblematic role in the resolution of inflammation by (M2) macrophages (Verreck et al., 2004). BMDM derived from *Pkm2*$^{fl/fl}$ and *Pkm2*$^{\Delta myel}$ mice produced notable amounts of IL-10 when stimulated with LPS. *Pkm2*$^{\Delta myel}$ BMDM showed slightly less IL-10 in the supernatant, although this effect was not significant (Figure 9(c)). This effect could possibly be attributed to a general tendency of *Pkm2*$^{\Delta myel}$ BMDM towards a more M1-like phenotype as indicated by the increase in the production pro-inflammatory cytokines mentioned above.

Apart from the examination of genotype-specific differences between *Pkm2*$^{fl/fl}$ and *Pkm2*$^{\Delta myel}$ BMDM, the effect of TEPP-46 on BMDM was evaluated. The small molecule has been claimed to promote PKM2 tetramerization, enzymatic activation and mitigation of LPS-induced cytokine production by macrophages *in vivo* (Jiang et al., 2010, Anastasiou et al., 2012). To rule out possible cytotoxic effects of TEPP-46, BMDM were exposed to TEPP-46 (100µM) alongside with LPS and IL-4. In homeostasis, TEPP-46 did not influence the transcription of *Il1*β, *Il6*, *Ccl2* and *Il10* (Figure 8). To assess whether pretreatment of the cell culture with TEPP-46 prior to LPS stimulation was able to mitigate the M1-like response, BMDM were pretreated with TEPP-46 30 minutes before LPS stimulation. Surprisingly, TEPP-46 failed to decrease the production of typical M1 cytokines like TNFα (Figure 8(a)) and IL-1β (data not shown). Instead, concentrations of these pro-inflammatory cytokines were elevated after pretreatment with TEPP-46 and even significantly higher in *Pkm2*$^{\Delta myel}$ BMDM when compared to stimulation with LPS alone. With regard to IL-10, TEPP-46 did not boost its secretion into the supernatant by BMDM. These findings directly contradict the reports by Pålsson and colleagues, who described a successful reduction of the transcription of pro-inflammatory cytokines and a boost of *Il10* transcription after treating BMDM with the exact same doses of TEPP-46 and LPS (Palsson-McDermott et al., 2015). A possible explanation for this divergence might in part be provided by the pro-inflammatory priming of *Pkm2*$^{\Delta myel}$ BMDM in comparison to wildtype BMDM used by Pålsson and colleagues. However, this does not explain why TEPP-46 failed to reduce pro-inflammatory cytokine concentrations in the control group *in vivo*.

4.2.2 Metabolic aberrations in BMDM derived from *Pkm2*$^{\Delta myel}$ mice

Macrophages have been identified as inherently glycolytic more than half a century ago (Hard, 1970). They undergo drastic alterations of their metabolic program upon classical or alternative activation. Activation with TLR ligands has been shown to induce the

incorporation of glucose transporters into the cell membrane (Fukuzumi et al., 1996) and to promote the induction of other glycolytic genes such as *HK* (**Newsholme1986a**) or PFK2 (Rodríguez-Prados et al., 2010).

In the present study, we speculated that aberrations in PKM isoform expression and quarternary structure had an impact on the glycolytic flux and the subsequent metabolism in the TCA and the ETC. For this purpose, a Seahorse XF Cell Mito Stress Test was used (see section 2.2.15 for details). The experimental setup comprised of classical activation by LPS, one in the very early state of stimulation (2h after exposure) and a late stimulatory condition (24 hours after exposure), in order to capture early adaptations (predominantly caused by molecular interactions) and delayed effects attributable to the induction of genetic transcription. As shown in section 3.2.3, $Pkm2^{\Delta myel}$ BMDM showed a higher rate of basal ECAR than BMDM from floxed individuals (Figure 10(b)). ECAR is often considered a direct indicator of the glycolytic flux. In this case, BMDM derived from $Pkm2^{\Delta myel}$ mice turned out to break down remarkably more glucose to pyruvate than their controls. In both groups, ECAR increased upon short term exposure to LPS (2 hours), underlining the importance of the glycolytic pathway in activated macrophages. The basally and initially increased levels of ECAR are presumably promoted by overexpression of PKM1 (see also section 4.1.1), principally driving $Pkm2^{\Delta myel}$ BMDM towards a more glycolytic program. Interestingly, long-term stimulation with LPS abrogated the genotypical difference, and $Pkm2^{fl/fl}$ BMDM showed almost identical acidification rates after 24 hours of LPS exposure. A possible explanation in addition to sheer PKM1 overexpression might be a genotypic difference in molecular interactions (such as posttranslational modifications) in $Pkm2^{\Delta myel}$ BMDM which lead to an increased ECAR on a basal level and after short term exposure, but which are compensated by the induction of glycolytic genes, which simply need more time to take effect. A potential candidate could be PFK-2, also called phosphofructokinase-2/fructose 2,6-bisphosphatase. It has been described to be activated by phosphorylation, and SRC has been identified as a facilitator of this posttranslational modification (Deprez et al., 1997, Ma et al., 2020). Additionally, this enzyme has been described to exist in two isoforms (called liver type PFK-2 and ubiquitous PFK-2), the latter of which is regulated by HIF1α and possesses a remarkable kinase activity, thus amplifying the glycolytic flux in macrophages (Rodríguez-Prados et al., 2010). The proposed mechanism leading to a preferential PKM2 dimerization might hence be also involved in the induction of glycolysis. A possible limitation of this notion, however, is the oversimplified view of ECAR as a direct indicator value of glycolytic activity. It does not take into account acidification derived from carbonate dehydratase-mediated CO_2 metabolism

$$CO_2 + H_2O \rightleftharpoons HCO_3^- + H^+ \rightleftharpoons H_2CO_3$$

in an aquaeous medium; also, ATP hydrolysis itself - which is the main source of energy especially in an activated cellular environment - is inherently acidifying (Divakaruni et al., 2014). Considering the observations for OCR described below, ECAR could consist

of an increase in glycolytic flux and ATP hydrolysis, fueled by the elevated demand for energy in *Pkm2*$^{\Delta myel}$ BMDM. Interestingly and in spite of the counterintuitive effects of TEPP-46 with regard to cytokine secretion (section 4.2.1), TEPP-46 successfully reduced ECAR in *Pkm2*$^{\Delta myel}$ BMDM (Figure 10(b), right bars). The reductive effect was more pronounced and thus only significant in BMDM derived from *Pkm2*$^{\Delta myel}$ mice, conceivably due to the basal enhancement of ECAR in this group as mentioned earlier. The Cell Mito Stress Test was originally designed as a "standard assay for assessing mitochondrial function" (https://www.agilent.com). Its basic principle is to measure the amount of O_2 consumed by the cells. OCR is often equated with ATP linked-respiration, as in complex IV of the ETC, electrons are transferred to O_2, thus generating H_2O. However, like the interpretation of ECAR, OCR similarly comprises of multiple additional factors contributing to the consumption of O_2, such as NADPH oxidases, nitric oxidases and other redox systems (Stuart et al., 2018), and should therefore not solely be accredited to ATP-linked respiration. In our experiments, BMDM from *Pkm2*$^{\Delta myel}$ mice displayed an intrinsically elevated OCR by approx. 30% in comparison to controls (Figure 10(a)). After two hours of LPS stimulation, O_2 consumption did not differ significantly from untreated conditions but was still substantially greater in *Pkm2*$^{\Delta myel}$ BMDM. However, after 24 hours of stimulation, OCR in the cell culture had plummeted in both groups, indicating a restriction of cellular respiration when challenged in a continuous manner. In light with the simultaneous induction of glycolysis (Figure 10(b)), the present study supports the assumption that classically activated macrophages undergo a metabolic switch towards a more glycolytic phenotype (Hard, 1970, Palsson-McDermott et al., 2015, Shirai et al., 2016). Interestingly, the observed increase in ECAR occured well before the decline in OCR, implying a decrement of a transcriptional program of oxidative phosphorylation over time in lieu of fast acting posttranslational modifications which would inhibit respiratory key players directly and thus more rapidly. As for TEPP-46, which has been shown to induce PKM2 tetramerization, the present study does not support the assumption that the small molecule promotes oxidative phosphorylation through an increased flux of pyruvate into the TCA. Conversely, TEPP-46 greatly reduced OCR in BMDM regardless of genotype (Figure 10(a), right bars), which questiones reports by Pålsson and colleagues who found no significant effect on OCR after treating BMDM with TEPP-46 (Palsson-McDermott et al., 2015). Still, TEPP-46 has been described to diminish OCR in NK cells (Walls et al., 2020), contributing to the controversial perspective of the modulator's role in metabolic reprogramming of immune cells.

The Cell Mito Stress Assay allows the assessment of additional metabolic parameters besides basal OCR and ECAR. Through inhibition and/or uncoupling of certain parts of the ETC, OCR can be broken down even further in order to calculate the amount of OCR that is attributable to ATP regeneration (see section 2.2.15 and Figures 10(c) and 11). ATP-linked respiration is calculated by subtracting proton leakage from basal respiration (Divakaruni et al., 2014). Our data demonstrates that *Pkm2*$^{fl/fl}$ BMDM exhibit a significantly elevated rate of ATP-linked OCR in comparison with *Pkm2*$^{fl/fl}$

BMDM. Like basal OCR, this effect was visible in homeostasis and after short term classical activation, and decreased considerably after 24 hours of LPS stimulation or treatment with TEPP-46. Although mimicking the kinetics shown for basal OCR, the very similar observation for ATP-linked OCR adds to the understanding of the metabolic demands in macrophages; this genotype-specific difference points to an enhanced demand for ATP in *Pkm2*$^{\Delta myel}$ BMDM, which is largely determined by the cell's ATP consumption (Lunt and Vander Heiden, 2011). In connection with the aforementioned differences in cytokine production, ATP demand and regeneration might mirror an intrinsic pro-inflammatory phenotype in *Pkm2*$^{\Delta myel}$ BMDM due to aberrations in the metabolic flux. This hypothesis is supported by the determination of another calculated parameter of the Cell Mito Stress Assay, the proton leak. This phenomenon is caused by protons which "leak" through the mitochondrial membrane and do not partake in fueling the ATP synthase (Brand and Nicholls, 2011). A previous study showed a positive correlation between proton leakage and ROS production in macrophages (El-Khoury et al., 2011), which additionally strengthens the hypothesis that, in our model, shifts in PKM expression ultimately lead to an increase in ROS production.

Aside from basal OCR and ECAR, we originally aimed to determine the spare respiratory capacity of BMDM from both genotypes, which is defined as the difference between maximal and basal respiration. Usually, this is achieved by the injection of FCCP, a potent uncoupler of respiration. This protonophore induces an artificial inward flux of protons in the mitochondrion, which leads to a compensatory boost of the ETC complexes in order to maintain the proton-driven potential across the mitochondrial membrane (Ward et al., 2000). As shown in Figure 11 (a)-(c), FCCP injection restored OCR partly but failed to surpass basal levels regardless of genotype, which would have been necessary in order to calculate the spare respiratory capacity (Divakaruni et al., 2014). The insufficiency of the FCCP injection could either be a result of suboptimal FCCP titration or mitochondrial dysfunction. Interestingly, stimulation with TEPP-46 restored a minimal reserve capacity in both genotypes (e), probably due to the overall suppressive effect on BMDM metabolism mentioned earlier, which leaves room for spare respiratory activity. Nonetheless, conclusions could be drawn from the detailed analysis of the assay. Firstly, LPS stimulation lead to an increase in mitochondrial dysfunction and exhaustion in a time-dependent manner, since the cellular response to FCCP declined over time (see (b), 2 hours LPS, and (d), 24 hours LPS). Secondly, exposure of BMDM to LPS and ATP as a second stimulus equalized the initially visible genotypic difference. This observation could be based on an intrinsically primed "pre-activation" of the NLRP3 inflammasome in *Pkm2*$^{\Delta myel}$ BMDM (see also section **??** and Figure 19(f)). Normally, the NLRP3 inflammasome pathway is initiated by two signals: TLR activation (in this case mediated through LPS) and binding of an appropriate ligand to the $P2X_7$ receptor (Bauernfeind et al., 2009, Mariathasan et al., 2006). The nullfication of the significant initial difference in O_2 consumption upon ATP stimulation could hence be linked to a pro-inflammatory transcriptional program in *Pkm2*$^{\Delta myel}$ BMDM.

In summary, BMDM derived from $Pkm2^{fl/fl}$ mice were inherently more active with regard to ECAR and OCR, suggesting a higher ATP and glycolytic turnover, with a substantial proportion of OCR being linked to ATP regeneration. $Pkm2^{\Delta myel}$ BMDM furthermore exhibited a less tightly coupled ETC, thus likely to contribute to the synthesis of ROS in these cells. TEPP-46 reduced both ECAR and OCR, indicating a suppressive effect on the entire metabolic flux in macrophages rather than promoting oxidative phosphorylation. Adding ATP to LPS as a stimulant enabled $Pkm2^{fl/fl}$ BMDM to catch up with $Pkm2^{\Delta myel}$ BMDM in terms of O_2 consumption, pointing to a preformed pro-inflammatory program in $Pkm2^{\Delta myel}$ BMDM which could involve the NLRP3 inflammasome.

4.2.3 $Pkm2^{\Delta myel}$-derived BMDM show unimpaired M2 polarization

Since the initial proposal of a dichotomous macrophage polarization devided into classically activated M1 and alternatively activated M2 macrophages (REF), researchers have come a long path contextualizing this theorem and adapting it to various contexts of microenvironments. Stimulation of TLR2 and 4 by LTA and LPS leads to a pro-inflammatory polarization including the secretion of IL-1, IL-6, IL-23 or TNFα (see section 3.2.2) and promotes a Th1 T cell response and subsequent pathogen clearance and tissue damage (Martinez and Gordon, 2014). On the other end of the spectrum, macrophages stimulated with IL-4 possess intriguing abilities in immunoregulation by (among other things) provoking a Th2 cell response and by inducing tissue repair (REF).

PKM2 has recently been reported to play a role in macrophage polarization. Emerging evidence supports the enzyme's role in promoting macrophage M1 polarization in coronary artery disease (Shirai et al., 2016) and non-alcoholic fatty liver disease (NAFLD, Kong et al., 2019), but also a direct involvement of PKM2 in M2 macrophage polarization has been proposed (Cheng et al., 2017, Xu et al., 2020). The mechanisms involving PKM2 which influence macrophage polarization are still being elicited and remain hitherto controversial, presumably due to the complexity and number of different players involved in the process. However, the flux of metabolites into the TCA has been found to mechanistically influence macrophage polarization (O'Neill et al., 2016). Very basically, pyruvate as the end product of glycolysis is converted to acetyl-CoA and enters the TCA, which regenerates ATP and GTP directly through substrate-level phosphorylation or indirectly by providing reduction equivalents ($NADH+H^+$ and $FADH_2$) for the subsequent in the complexes of the ETC. In classically activated (M1) macrophages, the flow through the TCA is delayed at the enzymatic step following the synthesis of succinate, succinate dehydrogenase (SDH), leading to an accumulation of succinate in macrophages. Initially, this build-up was considered a pro-inflammatory event, as succinate was shown to inhibit prolyl hydroxylase 3 (PHD3), which resulted in a stabilization of HIF1α and lastly lead to induction of glycolysis and upregulation of M1-like cytokines (Tannahill et al., 2013). Furthermore, PKM2 had previously been demonstrated to act as a cofactor for PHD3-mediated induction of HIF-associated

induction of transcription (Luo et al., 2011). However, the notion of cumulated succinate as a result of a stumbling TCA leading to M1 polarization has been challenged by reports indicating a anti-inflammatory role of succinate accumulation, as reduced SDH enzymatic activity dampens the production of ROS in macrophages (Lampropoulou et al., 2016). In alternatively activated (M2) macrophages, the TCA functions smoothly, thus enabling the cell to precede with the glycosylation of proteins relevant for M2 effector functions, such as CD206 or CD301 (Jha et al., 2015).

To test whether an interference in PKM2 conformation influenced the cells' capability of adopting an alternatively activated phenotype, M2-specific markers were assessed after stimulating BMDM derived from both genotypes with IL-4. CD206 and CD301 were clearly induced by treatment of the cell culture with IL-4. However, in this regard, BMDM from both genotypes were indistinguishable (Figure 12(a), (b), and (d)-(f)). BMDM derived from *Pkm2*$^{\Delta myel}$ mice showed no impairment of M2 polarization, as they were equally able to present these typical surface markers upon alternative activation. In addition to flow cytometric analyses, BMDM were analyzed for *Arg1* and *Socs1*, two proteins involved in M2-typical arginine metabolism. Again, IL-4 sufficiently induced upregulation of mRNA of *Arg1* and *Socs1*, though no significant differences between the genotypes were observed. Lastly, CCL22, a potent chemoattractant secreted by M2 macrophages known to attract regulatory T cells (Orecchioni et al., 2019, Rapp et al., 2019) was measured by an immunoassay. Stimulation with LPS triggered a small release of the cytokine in both groups, whereas IL-4 resulted in strong CCL22 secretion. CCL22 concentrations after IL-4 stimulation were lower in *Pkm2*$^{\Delta myel}$ BMDM, though this did not reach statistical significance.

Apart from the hypothesized differences between *Pkm2*$^{fl/fl}$ and *Pkm2*$^{\Delta myel}$ BMDM, the influence of TEPP-46 on macrophage polarization was assessed. The pharmacological activator of PKM2 has recently been published to play a role in M2 macrophage effector function and has been reported to inhibit Th1 polarization of T cells (Palsson-McDermott et al., 2015, Angiari et al., 2020). Surprisingly, the activator's effect exerted on key markers of M2 polarization was remarkably limited. A very modest increase in CD206 MFI was observed, as well as a mild increase in CD301 MFI (Figure 12(b) and (f)). CCR2 was additionally measured by flow cytometry (see (g)) because the receptor has previously been associated with M2 polarization in the context of multiple myeloma (Xu et al., 2019). The proportion of CCR^{+} cells was increased after LPS and TEPP-46, respectively. Still, evidence for a definitve role in M2 macrophage polarization is lacking. Intriguingly, the ectonucleotidase CD39 was highly expressed upon stimulation of the cell culture with TEPP-46 (Figure 12(c)). ???? Weniger Glycolyse, weniger OXPHOS, aber mehr CD39? Normalerweise wird ATP durch TLR signalling released und dann CD39 hochreguliert, um die Entzuendung zu begrenzen...

The unifying element of the studies cited above which propose a direct involvement of PKM2 in M2 macrophage polarization is their focus on either pharmacological activation of the enzyme (Palsson-McDermott et al., 2015, Xu et al., 2020) or the absence of dimeric PKM2 in the nucleus ameliorating a M1-like immune response rather than inducing

a classical M2 phenotype (Cheng et al., 2017). For that matter, it is imaginable that in this work, overexpression of the highly active isoform PKM1 allows for unimpeded manifestation of M2-like macrophage characteristics in *Pkm2*$^{\Delta myel}$ BMDM. In fact, a recent publication showed that in macrophages an intact oxidative metabolism is a critical determinant of a successful M2 polarization (Van den Bossche et al., 2016). PKM2 expression could even dispensable for M2 polarization based on the assumption that an unimpaired flow through the TCA and ETC is the main parameter for M2 macrophage polarization. This interpretation could moreover resolve the question why pharmacological activation of PKM2 by TEPP-46 did not influence BMDM polarization as clearly as previously reported.

4.3 Partial PKM2 knock-down affects hepatic homeostasis and renders mice more susceptible to acute liver damage

The liver as an organ within the equilibrium of immunogenic and tolerogenic factors harbors approximately 80-90% of all tissue-resident macrophages in mammals. KC account for roughly one third of all NPC (Bilzer et al., 2006). In addition to KC, monocyte-derived macrophages are part of the hepatic myeloid compartment (Ju and Tacke, 2016). Its characteristics and functions have extensively been described in (REF); briefly, myeloid cells have been shown to interact with almost every other cell type in the liver, including hepatocytes, LSEC, HSC, granucolytes and T cells. Besides maintaining a tolerogenic environment despite of the constant influx of nutrients and microbial agents, hepatic macrophages clear the liver of metabolic waste, regulate cholesterol homeostasis and eliminate aging cells (Wen et al., 2021). In light of this overarching set of interactions and functions in the hepatic cellular environment, *Pkm2*$^{\Delta myel}$ mice were analyzed for changes in hepatic metabolism and the composition of myeloid and lymphoid cellular compartments in homeostasis. Furthermore, the present study examined the role of differential PKM expression in acute immune-mediated hepatitis.

4.3.1 Aberrations in hepatic metabolism

KC and monocyte-derived hepatic macrophages engage in a dynamic crosstalk with hepatocytes. There is ample evidence for an involvement of hepatic macrophages in the initiation and maintenance of NAFLD (Wenfeng et al., 2014, Kong et al., 2019). Moreover, they have been shown to directly interact with hepatocytes and vice versa, thereby impacting the metabolism of the entire organism (Morgantini et al., 2019). Mechanistically, pro-inflammatory cytokines like IL-1β have been shown to induce *Srebf* transcription in hepatocytes, leading to an upregulation of the LDL receptor and consecutive accumulation of lipids, thus promoting the development of NAFLD (Ma et al., 2008).

Given the abundance of macrophages in the liver and based on the observations made in *Pkm2*$^{\Delta myel}$ BMDM with regard to PKM expression, aberrations in the metabolic flux and cytokine production, a possible impact on the systemic and hepatic metabolism was

hypothesized. Therefore, the mice and their livers were weighed, and serum ALT as well as cholesterol and triglyceride concentrations were measured. Intriguingly, 12-week old *Pkm2*$^{\Delta myel}$ mice and their livers were substantially heavier than the control mice (Figure 14(a) and (b)). While ALT levels showed no genotype-specific difference, *Pkm2*$^{\Delta myel}$ mice exhibited almost double the amount of blood cholesterol and triglycerides (see (c)-(e)). Since the joint presence of obesity, elevated cholesterol and triglycerides and an enlarged liver is a hallmark of a (developing) metabolic syndrome (Grundy et al., 2005), more in-depth analyses of indicators for aberrations in hepatic metabolism were performed. Therefore, the transcriptional activity of a set of key metabolic players was analyzed (Figure 14(g)). Unexpectedly, mRNA levels of genes involved in both degradation and *de novo* synthesis or storage of fatty acids were upregulated. *Cpt1α* as a key regulatory enzyme enabling β-Oxidation was upregulated, as was *Cyp7a1*, the rate-limiting step of bile acid synthesis, which has been shown to be increased in livers of NAFLD patients (Jiao et al., 2018). mRNA levels of *Pgc1α*, the master transcriptional regulator of mitochondrial biogenesis, were also observed to be increased. These targets were chosen in order to monitor different pathways involved in the processing of hepatic fatty acids in *Pkm2*$^{fl/fl}$ mice. On the other hand, *Fasn* and *Srebf1* were also upregulated, indicating an increase in *de novo* synthesis of fatty acids as well as an increased storage of fatty acids in the liver. Owing to the remarabkle differences in mRNA levels of genes related to fatty acid oxidation and synthesis, sera of *Pkm2*$^{fl/fl}$ mice and their controls were analyzed for concentrations of acyl carnitines (Figure 14(f)). These metabolites are generated by the reaction of acyl-CoA with a molecule of l-carnitine, a process facilitated by CPT1α. While there was no apparent difference of l-carnitine (C0) or short-chain acyl carnitines, medium and long-chain compounds, in particular consisting of 10-14 carbon atoms, were present in the sera at higher concentrations. These data support the proposed NAFLD-like phenotype in *Pkm2*$^{\Delta myel}$ mice, as long-chain acyl carnitines have been reported to reflect mitochondrial dysfunction in murine hepatocytes and in hepatocytes of NAFLD patients (Bjørndal et al., 2018, Peng et al., 2018, Enooku et al., 2019). Intriguingly, this dysfunction does not include insufficencies in the TCA, which has, on the contrary, been shown to be induced in a murine model of NASH (Patterson et al., 2016). An unhindered flux through the TCA could therefore explain why no significant difference in the transcriptional activity of *Glut1* and *Ldh*, two central glycolytic genes, was observed. Still, *Hif1α* mRNA was signficantly increased in *Pkm2*$^{\Delta myel}$ livers. Although mainly associated with the transcriptional regulation of glycolytic genes, HIF1α has been demonstrated to induce the transcription of *Fasn* and *Srebf1* in tumor cells (Furuta et al., 2008), which matches the observations made concerning the lipogenesis-associated genes in livers of *Pkm2*$^{\Delta myel}$ mice.

All observations mentioned above were made in whole liver tissue or in the serum of *Pkm2*$^{\Delta myel}$ mice, and a direct involvement of myeloid PKM2 in such deviations was initially not considered completely obvious. However, evidence is emerging that PKM2 in hepatic myeloid cells exerts a strong influence on hepatic metabolism and also in reverse. For instance, PKM2 has been related to HCC development by ectosomal release

of the enzyme which induces a monocyte to macrophage transition in the liver and results in a CCL1-mediated feedforward loop (Hou et al., 2020). A direct involvement of myeloid PKM2 has moreover been shown in the pathogenesis of NAFLD: dimeric PKM2 was identified as a critical determinant of a M1-like polarization of hepatic macrophages, which secrete TNFα, IL-1β and CCL2. The ensuing hepatic inflammation has furthermore been demonstrated to directly disturb the metabolic homeostasis of fatty acids in mice when fed a high-fat diet. By contrast, pharmacological activation of PKM2 in macrophages mitigated the initially observed inflammation and simultaneously reduced lipid accumulation in the adjacent hepatocytes, thus ameliorating the NAFLD phenotype (Kong et al., 2019).

Considering the cited literature and the data demonstrated in section 3.3.1, an involvement of myeloid PKM2 in the deviations of hepatic metabolism depicted in Figure 14 seems plausible. A mechanistical explanation might involve a pro-inflammatory macrophage phenotype driven by preferential PKM2 dimerization and subsequent transcription of pro-inflammatory genes in $Pkm2^{\Delta myel}$ mice.

4.3.2 Partial PKM2 knock-down changes leukocyte composition in key compartments

The portal vein consists of the vascular confluence of the splenic vein and the superior mesenteric vein and collects the venous blood of all unpaired abdominal organs, including stomach, pancreas, gallbladder, small intestine and colon. Due to this anatomical characteristic, the vast majority of nutrients and pathogens reabsorbed along the gastrointestinal tract ends up in the liver sinusoids, where hepatic macrophages are localized. These comprise of yolk-sac derived resident macrophages (KC) and monocytes circulating through the liver with the blood stream, which infiltrate the liver become tissue macrophages in response to chemotactic signals like CCL2, especially in an inflammatory context (Karlmark et al., 2009). However, despite originating from entirely different organs and disparate mechanisms of self-renewal, definite markers to distinguish both cell types are yet to be found. They include, among others, CD11b as a pan-myeloid marker, as well as F4/80 for mature macrophages, whereas Ly6G serves as a marker for neutrophils (Dos Anjos Cassado, 2017). Especially with regard to the hepatic niche, cells double-positive for CD11b and Ly6C have been considered to represent pro-inflammatory monocytes, which express the chemokine receptor CCR2 on their surface, while $CD11b^{+}$ $Ly6C^{-/low}$ cells mainly consist of "patrolling" monocytes, which are predominantly positive for CX3CR1 (Ju and Tacke, 2016). A monocytic population expressing intermediate levels of Ly6C has also been proposed, though whether they represent a distinct group of monocytes or exhibit a transitional state from $Ly6C^{-}$ to $Ly6C^{+}$ cells and vice versa has yet to be clarified (Zimmermann et al., 2012).

In the present work, we aimed to characterize myeloid cellular compartments by flow cytometry (see section 3.3.2). Due to the pro-inflammatory phenotype of $Pkm2^{\Delta myel}$ BMDM including elevated CCL2 production and in light of the metabolic changes

apparent in livers of *Pkm2*$^{\Delta myel}$ mice, three compartments were analyzed: The bone marrow as the hatchery for all myeloid cells, the spleen (due to its role as a secondary lymphatic organ and a forum for myeloid-lymphoid interactions) and the liver as the organ of particular interest for this study. There was no observable difference in CD11b^{+} cells in either organ (Figure 15(a) for bone marrow, data not shown for spleen and liver), pointing to an unimpeded development of myeloid cells in the bone marrow and indicating stable myeloid populations in the spleen and liver. Similarly, the amount of CD11b^{+} Ly6C$^{-/low}$ monocytes was widely comparable between the genotypes (data not shown). Still, the proportion of CD11b^{+} myeloid cells positive for Ly6C turned out to be significantly increased in all three compartments of *Pkm2*$^{\Delta myel}$ mice, suggesting a elevated count of monocytes in their respective parenchymae in homeostasis. In the spleen, F4/80 was included as a marker of mature macrophages, which did not differ between the genotypes (see (c), left bars). However, the number of Ly6C^{+} cells was increased with and without gating for F4/80 first (see (c), right bars for CD11b^{+} F4/80^{+} Ly6C^{+} cells and p=0.078 for the genotype comparison of CD11b^{+} Ly6C^{+} splenic cells, data not shown). Also, hepatic F4/80 expression turned out to be similar between between the genotypes, whereas the proportion of Ly6C^{+} of myeloid cells was increased with and without the inclusion of F4/80 in the livers of *Pkm2*$^{\Delta myel}$ mice (see (d)-(f)). Furthermore, the vast majority (>90%) of CD11b^{+} Ly6C^{+} cells expressed CCR2. These results point to a predisposition of *Pkm2*$^{\Delta myel}$ mice for monocytic infiltration already in homeostasis, which could possibly increase susceptibility towards inflammatory stimuli: Neutrophils and pro-inflammatory monocytes rapidly infiltrate the liver parenchyma upon acute liver injury (Karlmark et al., 2009). A key role in priming livers of *Pkm2*$^{\Delta myel}$ mice with pro-inflammatory monocytes could be mediated through the CCL2/CCR2 axis. *Pkm2*$^{\Delta myel}$ BMDM secreted more CCL2 upon LPS challenge *in vitro* (see Figure 8(b) and 9(b)), and CCL2 mRNA levels were elevated in *Pkm2*$^{\Delta myel}$ livers in comparison to controls after ConA injection (see Figure 18(a)). Recruitment of pro-inflammatory monocytes through CCL2/CCR2 interaction has been directly linked to liver injury and, strikingly, also to the exacerbation of NAFLD and NASH in mice (Baeck et al., 2012, Miura et al., 2012). Moreover, the direct pharmacological inhibition of CCR2 has been demonstrated to reduce monocyte infiltration and liver damage in acute liver injury (Song et al., 2017). Liver-resident macrophages (as indicated by high F4/80 expression) did not turn out to differ quantitatively, suggesting that the expansion of hepatic myeloid cells in *Pkm2*$^{\Delta myel}$ mice is primarily due to infiltrating monocytes rather than due to an increased proliferation of KC.

In the course of the myeloid characterization by flow cytometry, preliminary data was additionally collected regarding lymphoid cells in the spleen and bone marrow of *Pkm2*$^{\Delta myel}$ and *Pkm2*$^{fl/fl}$ mice (Figure 16), as an immune cross-talk between the lineages was hypothesized. Intriguingly, even on a rather basal level of marker differentiation, clear differences in the lymphoid cellular compartment were observed between the genotypes. CD4 expression was clearly reduced by approx. 3-5% of all vital single cells in the livers and spleens of *Pkm2*$^{\Delta myel}$ mice (see (a)). Furthermore, the amount of

hepatic $CD8^+$ cells was significantly elevated (see (b)). These shifts lead to a significantly reduced CD4/CD8 ratio in both organs of $Pkm2^{\Delta myel}$ mice. Under healthy conditions, this ratio is approx. 1:3.5 (Horst et al., 2016), as seen in livers of $Pkm2^{fl/fl}$ mice. Yet, in $Pkm2^{\Delta myel}$ mice we observed a ratio of 1:2.5 (see (c)). $CD8^+$ effector T cells have been identified as a key regulator of hepatic inflammation in a murine model of hyperlipidemic NASH, and NAFLD has been found to induce the specific loss of $CD4^+$ cells through hepatic lipotoxicity (Breuer et al., 2020, Ma et al., 2016). Given the aberrations in the systemic and hepatic metabolism which indicate a early NAFLD-like phenotype in $Pkm2^{\Delta myel}$ mice (see section 3.3.1), an involvement of the myeloid knockdown of PKM2 in the homeostasis of $CD4^+$ and $CD8^+$ cells is conceivable. The $CD4^+$ cellular subset was furthermore analyzed for markers of activation, suppression and regulatory cell subsets. $CD4^+$ cells showed less activation as indicated by CD25 MFI and proportional marker expression (Figure 16 (d)), while simultaneously expressing higher levels of PD-1 (see (e) and (f)). Upregulation of the co-inhibitory molecule PD-1 has in fact been described for $CD8^+$ cells in murine NAFLD, but it was not observed in $CD4^+$ cells (Hansel et al., 2019). The underlying difference which caused elevated levels of PD-1 on $CD4^+$ cells in the present study thus remains mostly unclear, though the simultaneous occurrence of CD4/CD25 downregulation and PD-1 upregulation points to an inhibitory program in the hepatic lymphoid compartment of $Pkm2^{\Delta myel}$ mice. Lastly, regulatory T cells ($CD4^+$ $CD25^+$ $Foxp3^+$, T_{reg}) were evaluated. $Pkm2^{\Delta myel}$ mice exhibited an increased proportion of $Foxp3^+$ cells of $CD4^+$ $CD25^+$ cells within their livers. A review by Van Herck and colleagues gathered data from seven studies (four murine, three human) with regard to frequencies of hepatic T_{reg} in models of murine NALFD or patients with NAFLD (Van Herck et al., 2019). Four studies reported decreased numbers of T_{reg}, whereas two found elevated T_{reg} frequencies and one study did not describe any difference of hepatic T_{reg} quantities. Despite the inconclusive narrative on the fate of T_{reg} in hyperlipidemic conditions, some evidence supports the notion that these cells might in fact profit from a high abundance of fatty acids in their immediate proximity. Oleic acid, an established compound known to induce steatosis in cell cultures of hepatocytes (Ricchi et al., 2009), has been demonstrated to promote oxidative phosphorylation in T_{reg}, thus increasing their suppressive capabilities towards effector T cells (Pompura et al., 2021). However, whether the proposed deviations in hepatic lipid metabolism caused by the genetic model used in the present study support T_{reg} survival, remains hypothetical. Moreover, it is essential to note that for this work proportional quantities of immune cells were measured, and that a reduction in CD4 expression could disguise the actual number of hepatic T_{reg}.

Taken together, the present work reports significant changes in the myeloid cellular compartment of the bone marrow, spleens and livers of $Pkm2^{\Delta myel}$ mice. These animals showed increased quantities of $Ly6C^+$ monocytes, which is hypothesized to display a pro-inflammatory predisposition, that might mechanistically be mediated through increased CCL2/CCR2 signalling, both of which have been linked to a NAFLD-like phenotype. The recruitment of additional monocytes into the liver parenchyma, which display the

same pro-inflammatory proclivity, might contribute to a subclinical phenotype of fatty liver disease in our model. Apart from myeloid cells, hepatic $CD4^+$ cell cells were reduced, while $CD8^+$ were more frequent, thus reducing the CD4:CD8 ratio in *Pkm2*$^{\Delta myel}$ livers in a NAFLD-like manner. $CD4^+$ cells expressed lower levels of CD25 as an activation marker, although a proportional upregulation of PD-1 as a co-inhibitory molecule and Foxp3 as a marker for T_{reg} was observed. As the data for lymphoid cells is considered a first, preliminary assessment, a role of myeloid PKM2 in the regulation of T cells is speculative. Still, the involvement of effector T cells in this context could potentiate the suggested pro-inflammatory disposition in *Pkm2*$^{\Delta myel}$ mice, which contributes to the aberrations in hepatic metabolism.

4.3.3 Exacerbated immune-mediated liver injury in *Pkm2*$^{\Delta myel}$ mice

To assess the hypothesis whether a partial knockdown of PKM2 might influence the immunological function of myeloid cells *in vivo*, *Pkm2*$^{fl/fl}$ and *Pkm2*$^{\Delta myel}$ were exposed to an intravenous injection of the lectin Concanavalin A (ConA). The carbohydrate-binding protein has been demonstrated to bind to liver sinusoids and to activate a variety of intrahepatic immune cells. Although initial studies assumed that ConA-mediated liver damage is mainly T cell-mediated, other studies have found a substantial involvement of myeloid cells, such as hepatic macrophages/KC and neutrophils (Tiegs et al., 1992, Zhuang et al., 2016, Schümann et al., 2000, Bonder et al., 2004). ConA-mediated liver injury is therefore most likely a result of an orchestrated immune response which involves several cellular players both from the lymphoid and myeloid compartment.

In this study, *Pkm2*$^{\Delta myel}$ mice exhibited exacerbated liver damage after sublethal injection of ConA in comparison to floxed control mice, as demonstrated by elevated serum ALT levels, aggravated necrosis and amplified diapedesis of myeloid cells (Figure 17). In preliminary experiments with ConA, *Pkm2*$^{\Delta myel}$ mice were found to be more susceptible and it was observed that a lower dose was needed in order to evaluate the liver damage after a pre-defined time period without individual mice succumbing to injection of the lectin. For this purpose, a dose of 5mg/kg body weight was chosen in this study. Previous studies used much higher ConA doses (up to 30mg/kg in NMRI albino mice, see Tiegs et al., 1992), though this difference is at least in part explained by a generally increased susceptibility of C57BL/6 mice toward the protein, and dose-finding experiments have been recommended. This is also due to the inevitable biological variation between batches, since ConA is extracted from the jack bean *Canavalia ensiformis*. Furthermore, serum ALT levels can vary considerably between individuals (Heymann et al., 2015). Despite considering and implementing the aforementioned premises, the results after ConA injection showed fluctuations (see Figure 17(b), (c) and (d)). To account for the scatter of serum ALT values, mice were additionally categorized by contingency analyses whether they did or did not respond to ConA with elevated serum ALT levels (Figure 17(c), see also section 3.3.3). *Pkm2*$^{\Delta myel}$ mice were twice as likely to respond to ConA treatment with elevated serum ALT levels as control mice,

which further highlights the increased susceptibility of *Pkm2*$^{\Delta myel}$ mice towards ConA. Moreover, myeloid cells were more frequent in livers of *Pkm2*$^{\Delta myel}$ mice, as indicated by MPO$^+$ cell quantities (see (d) and (e)). Given the physiological distribution of peripheral blood leukocytes, it is plausible that the majority of these MPO$^+$ are in fact neutrophilic granulocytes and monocytes. Also, CD11b$^+$ Ly6C$^+$ CCR2$^+$ monocytes have been found to be excessively recruited into the liver via the CCL2/CCR2 axis in acute liver injury as early as 8 hours after damage induction (Mossanen et al., 2016). This study shows that especially CD11b$^+$ Ly6C$^+$ CCR2$^+$ monocytes are more frequent in livers of *Pkm2*$^{\Delta myel}$ mice already in homeostasis (see Figure 15(d), (e) and (f)). It is possible that this causes a predisposed environment for hepatic myeloid cells and thus renders *Pkm2*$^{\Delta myel}$ mice more susceptible to ConA challenge. These data support the notion that myeloid cells play an important role in the pathogenesis of murine immune-mediated hepatitis.

As mentioned in sections 4.1.2 and 4.2.1, preferential dimerization of residual PKM2 in *Pkm2*$^{\Delta myel}$ myeloid cells intensified their pro-inflammatory cytokine response towards LPS *in vitro*. In conjunction with the elevated quantities of hepatic Ly6C$^+$ monocytes in *Pkm2*$^{\Delta myel}$ mice, the present study shows that cytokines emblematic for M1-polarized macrophages are exacerbated after 8 hours of ConA challenge (Figure 18). All key cytokines tested in BMDM after LPS stimulation (see section 3.2.2) were also elevated after ConA injection in *Pkm2*$^{\Delta myel}$ mice, pointing to a relevant contribution of macrophage-derived pro-inflammatory mediators in immune-mediated hepatitis. The data furthermore suggest a substantial role of myeloid PKM2 in exacerbating the inflammatory response in this model. Interestingly, *Ccl2* mRNA levels showed the greatest magnitude of regulation between PBS and ConA treatment and, in particular, between the genotypes. To date, a direct involvement of PKM2 in the production of myeloid CCL2 has not yet been demonstrated. In light with increased myeloid recruitment into the liver (as indicated by the number of MPO$^+$ cells as well as the abovementioned increased number of hepatic Ly6C$^+$ cells in homeostasis in *Pkm2*$^{\Delta myel}$ mice), a role for PKM2 in CCL2/CCR2-mediated expansion of the hepatic myeloid cellular niche is conceivable. A possible mechanism for PKM2-dependent transcription of *Ccl2* has been proposed by Zou et al. via phosphorylation of NF-κB in colorectal cancer. To assess whether the same pathway sufficiently explains the induction of CCL2 production in macrophages described in this study, further research is necessary. Another intriguing difference was observed for IL-23. In combination with IL-1 and IL-6, IL-23 is known to induce Th17 T cell polarization (Wilson et al., 2007), which contributes to ConA hepatitis and also to AIH in patients (Xia et al., 2018, Zhao et al., 2011). In addition to Th17 polarization, these cells have been found to be chemotactically attracted via the CCL2/CCR2 axis (Kara et al., 2015). An induction of hepatic myeloid IL-23 production in combination with elevated CCL2 levels might therefore promote Th17 polarization and migration into the liver parenchema, thereby amplifying the tissue damage in this model.

Pkm2$^{\Delta myel}$ mice exhibited symptoms of an early-stage metabolic syndrome with sign-

ficantly increased body weight, liver weight and blood cholesterol (Figure 14). Hepatic mRNA analyses showed severe aberrations in the homeostasis of liver metabolism, which were accompanied by an increase of long-chain acylcarnitines in the sera of *Pkm2*$^{\Delta myel}$ mice (see also section 4.3.1). These findings are in part emblematic of an early onset of NAFLD. Interestingly, NAFLD has been reported to aggravate acute-immune mediated hepatitis in mice (**Muller2016**). A similar observation has been made in humans, as patients with NAFLD or NASH and simultaneous AIH were more likely to develop liver cirrhosis than patients who solely suffered from AIH (**Weiler-Normann2016**). The authors assumed a pivotal role of "bystander cells" (referring to all non-antigen specific cells), which conceivably also include myeloid cells. It is therefore plausible that a NAFLD-like phenotype aggravates acute ConA hepatitis in *Pkm2*$^{\Delta myel}$ mice by priming the liver parenchyma with an increased number of myeloid cells, which display a more pro-inflammatory phenotype upon activation.

The exacerbated inflammatory response in the hepatic tissue of *Pkm2*$^{\Delta myel}$ mice was additionally accompanied by an acute metabolic shift in their livers. Genetic transcription directly linked to glycolysis was substantially upregulated in comparison to control mice (Figure 18 (e) and (h)), whereas genes linked to oxidative metabolism were widely suppressed (see (f) and (g)). In our model, the compensatory upregulation of PKM1 promotes aerobic glycolysis, as data gathered for extracellular acidification indicates (Figure 10(b)); the increase in *Hif1α* mRNA, which in our experiments was unique to *Pkm2*$^{\Delta myel}$ mice, also points to a Warburg-like phenotype. In fact, dimeric PKM2 has been shown to stabilize HIF and therefore promote PKM2-HIF1α-mediated transcription (Tannahill et al., 2013, Luo et al., 2011). To our knowledge, these data constitute the first assessment of metabolic aberrations caused by myeloid cells in acute immune-mediated hepatits, although metabolic aberrations towards aerobic glycolysis in the liver have been described for AIH, HBV and HCV (Wang et al., 2014, Meoni et al., 2019). The study by Wang et al. found increased levels of pyruvate, lactate and citrate by metabolomic analyses in the sera of AIH patients compared to healthy controls, patients with primary biliary cirrhosis or drug-induced liver injury, which points to a dysregulation of hepatic metabolism in favor of glycolysis. However, the authors could only speculate on the causes of these deviations. The present study sheds light on the underlying pathomechanisms which - apart from direct immune cellular effector functions - might partake in compromising hepatocyte integrity.

4.3.4 Activation of residual PKM2 mitigates liver damage in *Pkm2*$^{\Delta myel}$ mice

Since the first description of the *PKM* gene encoding for two distinct versions of PKM protein in 1986 by Noguchi et al. (Noguchi et al., 1986), PKM2 has been extensively studied in the context of cancer metabolism and has been found to be highly abundant in the majority of cancer entities, such as renal cell carcinoma, bladder carcinoma, hepatocellular carcinoma, lung and thyroid cancer Bluemlein et al., 2011). The observation

that PKM2 is involved in immune cellular effector functions has been, by comparison, made relatively recently. Pålsson and colleagues were the first to systematically identify PKM2 as a key regulator of macrophage polarization, phagocytosis and cytokine production (Palsson-McDermott et al., 2015). They applied the paradigm of cytosolic/tetrameric PKM2 and nuclear/dimeric PKM2 to macrophage function. The group demonstrated that macrophages rely on PKM2-mediated transcription of glycolysis to promote M1 polarization and subsequent production of IL-1β which can be reversed by pharmacological tetramerization and concomitant activation of PKM2 and its enzymatic activity. Their observations paved the way for translational experiments, which showed an involvement of myeloid PKM2 in sepsis, colitis, coronary artery disease and allergic airway disease, the latter of which were attenuated by pharmacological activation of PKM2 (Xie et al., 2016, Wang et al., 2017, Shirai et al., 2016, van de Wetering et al., 2020).

Since myeloid cells were more frequent in livers of *Pkm2*$^{\Delta myel}$ mice and due to the exacerbated damage seen after ConA injection, a beneficial role of pharmacological PKM2 activation in acute immune-mediated hepatitis was proposed (see sections 2.2.3 and 3.3.4 for experimental details). We hypothesized, that activation of PKM2 could prevent the enzyme to form dimers, which would enter the nucleus and promote the transcription of glycolytic and pro-inflammatory genes like *Il1*β. Nuclear Translocation of dimeric PKM2 has convincingly been demonstrated *in vitro* and *in vivo* (Palsson-McDermott et al., 2015, Shirai et al., 2016). In our experimental model, *Pkm2*$^{\Delta myel}$ mice pretreated with intravenous TEPP-46 (a pharmacological activator specific for PKM2) prior to ConA injection were protected from exacerbated liver damage, as shown in Figure 19. TEPP-46 attenuated serum ALT levels (see (a)) and reduced myeloid recruitment into the liver parenchyma (see (c) and (d)). Transcription of key cytokines like *Il1*β, *Il6* and *Il23*, which are all related to M1 polarization, was reduced (see (f)-(h)). Moreover, *Ccl2* transcription was dampened in the group pretreated with TEPP-46 (see (e)), which explains the reduced number of infiltrating myeloid cells after ConA injection and is consistent with the data acquired for myeloid CCL2 production and the increased frequencies of myeloid cells in homeostasis (see sections 3.2.2 and 3.3.2). TEPP-46 furthermore reduced *Hif1*α mRNA, though it did not alter the transcription of *Pkm1* or *Cpt1*α, which points to a transcriptional regulation besides a direct involvement of the PKM2-HIF1α axis.

In addition to the effects on diapedesis and cytokine secretion as direct myeloid effector functions, the implications of TEPP-46 on inflammasome-related pathways was assessed. PKM2-mediated induction of glycolysis has previously been shown to lead to NLRP3 activation and subsequent release of IL-1β and PAMP like HMGB-1 in macrophages in a murine model of LPS-induced sepsis (Xie et al., 2016). We hypothesized that TEPP-46 could ameliorate the inflammatory response attributable to NLRP3 inflammasome activation by suppressing hyperglycolysis (see Figure 10(b)). Indeed, TEPP-46 successfully suppressed transcription of *Nlrp3* (see Figure 19(i)), the major component of the NLRP3 inflammasome. Furthermore, *Pkm2*$^{\Delta myel}$ mice

treated with TEPP-46 showed lower levels of activated Caspase-1 (also called ICE, IL-1β converting enzyme) and lower levels of *Il1*β mRNA as direct downstream targets of the NLRP3 inflammasome. As another downstream mediator of inflammation, the subcellular localization of HMGB1 was assessed. Intriguingly, pretreatment with TEPP-46 prior to induction of hepatitis by ConA greatly reduced cytosolic and paracellular HMGB1, whereas mice treated solely with ConA showed massive release of HMGB1 into the liver parenchyma (see Figure 20). Although these findings have to be confirmed and quantified by further experiments (e.g. inflammasome compounds or serum levels of IL-1β and HMGB1 after adminstration of TEPP-46), the data presented in this work suggests an involvement of PKM2 in inflammasome-mediated activation of a pro-inflammatory macrophage phenotype that contributes pathogenetically to immune-mediated hepatitis.

4.4 Outlook

This study was performed to assess the role of PKM2 in myeloid effector function *in vitro* and in a murine inflammatory model *in vivo*. Furthermore, the present work aimed to broaden the molecular and cellular knowledge on the role of myeloid cells in immune-mediated hepatitis. Due to the diverse implications of partial PKM2 knockdown, including compensatory mechanisms and preferential dimerization of residual PKM2 in myeloid cells, this work primarily serves as an observational groundwork with a focus on hepatic and macrophage metabolism in $Pkm2^{\Delta myel}$ mice. It shows that metabolism and cellular effector functions are deeply intertwined and that interfering in the metabolic flux of myeloid cells has consequences for the entire organism. However, most of the relations discussed above have yet to be proven to confirm their direct and causal interconnections.

This study focussed mainly on macrophages and monocytes, although the genetic construct is likely to affect the majority of myeloid cells, which includes granulocytes and dendritic cells that have not been addressed so far; upcoming experiments should address these cell types in particular. Also, this study does not closely differentiate between monocyte-derived hepatic macrophages and KC, which are known to exhibit distinct functions as hepatic myeloid cells. Therefore, an assessment of *Cre*-mediated PKM2 knockdown in these cells should also be performed. Apart from cell-type considerations, future research should focus on confirming mechanistical explanations for the observed myeloid phenotype, for which this work offers a variety of concrete indications, like an increased ROS production by the hyperglycolytic metabolic state or the involvement of PKM2 in the production of CCL2 in $Pkm2^{\Delta myel}$ mice.

Moreover, the genetic construct used in this study should be reassessed. As discussed in detail in sections 4.1, 4.1.1 and 4.1.2, the incomplete knockdown of PKM2 in this study is difficult to interpret and leads to off-target effects like the drastic compensatory upregulation of PKM1 in $Pkm2^{\Delta myel}$ BMDM. Therefore, the immediate causal association between PKM2 knockdown and the effects observed *in vitro* and *in vivo* is in part

challenging to prove. Possible future strategies to address this issue include the use of a reporter-*Cre* strain in order to study the effects of a more complete PKM2 knockdown, which is currently underway in our laboratory. Additionally, the role of PKM1 should be taken into consideration, as an involvement of this PKM isoform is likely to contribute at least partially to the phenotype observed in $Pkm2^{\Delta myel}$ BMDM and mice due to its extensive overexpression (>30-fold in comparison to controls, see Figure 5). As most research focuces strongly on PKM2, it would be interesting to examine the effects of PKM1 overexpression. Although the latter is known to possess less regulatory setscrews than PKM2, the current study points to relevant PKM1 protein functions exerted by its enzymatic activity and its influence on the glycolytic flux in lieu of direct interactions with receptors or transcription factors.

In addition, since the phenotype displayed by $Pkm2^{fl/fl}$ mice points to the development of a metabolic syndrome and concomitant fatty liver disease, this predisposition should further be assessed by subjecting the mice to a methionine-choline deficient diet or a so called "Western diet", both of which are established animal models to study NAFLD/NASH development and implications in mice (**Machado2015**). This could help eliciting the underlying mechanisms which lead to aberrations in hepatic metabolism which were observed in this study in $Pkm2^{\Delta myel}$ mice. The Western diet would be also suitable to study the effects of myeloid PKM2 in the adipose tissue, as obesity is known to aggravate NAFLD and NASH by triggering pro-inflammatory macrophage responses, which influence the entire metabolic network and the liver in particular (**Lefere2019**).

With regard to PKM2-mediated aggravation of ConA hepatitis in $Pkm2^{\Delta myel}$ mice, these experiments should be repeated with a larger number of individuals to rule out possible exogenous confounders or coincidence. This would also help to obtain more biological material (e.g. liver samples, hepatic NPC) to further examine the exact signaling pathways which lead to an excacerbation of myeloid mediated damage after ConA injection. As mentioned, this study only provides first and to an extent preliminary data on a conceivable involvement of the NLPR3 inflammasome, which was successfully ameliorated by pretreating the mice with TEPP-46 prior to ConA. However, since the experimental groups are small, an experimental confirmation is necessary. Also, although macrophage contribution in acute immune-mediated hepatitis has been shown and studied in this work, investigating $Pkm2^{\Delta myel}$ mice in other models of liver injury could add to the insight of PKM2-related macrophage effector function *in vivo*. For instance, drug-induced liver damage by acetaminophen (APAP) could be an interesting model, as myeloid cells are known to extensively participate in damaging the liver after ingesting toxic doses of APAP (Mossanen et al., 2016).

Besides acute and chronic liver diseases, metabolic reprogramming is a common feature of many autoimmune diseases like systemic lupus erythematodes, rheumatoid arthritis, type 1 diabetes mellitus or multiple sclerosis (**Stathopoulou2019**). A deeper understanding of the underlying mechanisms could be beneficial through identifying specific metabolites or macromolecules as biomarkers for disease diagnosis or its pro-

gression; also, it could help to identify novel therapeutic approaches, which could be targeted specifically in order to ameliorate immune-mediated inflammation. In this context, TEPP-46 should be investigated in greater detail, as it has been beneficial in murine disease models from allergic airway disease to acute immune-mediated hepatitis shown in this work.

Abstract

Myeloid metabolism has emerged as a critical determinant of the innate immune system's capacity. Granulocytes, monocytes and macrophages as the immunological frontline not only have to quickly identify pathogens and endogenous alarmins but also to react and to contain the inflammatory stimulus, thus preventing pathogen dissemination and avoiding an unrestrained immune response, both of which pose a vital threat to the host organism. Myeloid cells in particular have been shown to regulate their own metabolism in order to execute these functions and to ensure an orchestrated subsequent immune response which also includes the adaptive immune system. Glycolysis as a gateway for carbon compounds is located at the very center of oxidative and anaerobic metabolic pathways. Posttranslational modifications of glycolytic enzymes enable the cell to rapidly regenerate ATP without time-consuming induction of oxidative metabolism while simultaneously providing intermediate compounds for the production of effector molecules. In this context, the role of PKM2 in myeloid cells was investigated. An incomplete *Cre*-mediated knockdown in macrophages exposed disturbances in the equilibrium of PKM2 oligomers by inducing PKM2 dimerization and upregulating PKM1 (Figure 5). *Pkm2*$^{\Delta myel}$ macrophages exhibited a more pro-inflammatory M1 phenotype *in vitro* (Figures 8 and 9) and showed an increased metabolic flux through glycolysis and oxidative respiration (Figure 10). However, they did not show signs of impaired or altered M2 macrophage polarization (Figure 12 and 13). Untreated 12 week old *Pkm2*$^{\Delta myel}$ mice presented characteristics of a beginning metabolic syndrome with elevated body and liver weight, hypercholesterolemia and accumulation of plasmatic long-chain acyl carnitines as well as aberrations in key metabolic players of hepatic metabolism, also indicating an early developmental stage of fatty liver disease (Figure 14). *Pkm2*$^{\Delta myel}$ mice showed increased numbers of CD11b^{+} Ly6C^{+} monocytes in their bone marrow, spleen and liver (Figure 15), as well as a reduced number of hepatic CD4^{+} cells with an increased CD4:CD8 ratio (Figure 16). Induction of acute immune-mediated hepatitis via ConA injection lead to an exacerbated liver damage in *Pkm2*$^{\Delta myel}$ mice with elevated serum ALT levels and myeloid infiltration (Figure 17), which was accompanied by an aggravated production of M1-like cytokines like IL-1β, CCL2 and IL-23 and a metabolic switch in the hepatic parenchyma towards aerobic glycolysis (Figure 18). Pharmacological activation of PKM2 by TEPP-46 ameliorated ConA-induced acute hepatitis and reduced the transcription of genes related to M1 macrophage polarization and inflammation, such as *Ccl2*, *Il1*β and *Il23*. Also, TEPP-46 reduced *Nlrp3* transcription, activation of Caspase-1 and release of HMGB-1 suggesting a role of myeloid PKM2 in the activation of the NLRP3 inflammasome (Figure 19 and 20). In conclusion, this study confirms the previosly proposed role of myeloid pyruvate kinases in macrophage effector function and expands its significance for the development and perpetuation of liver diseases.

Zusammenfassung

Der Stoffwechsel myeloischer Zellen stellt einen wesentlicher Indikator füer die Funktion des angeborenen Immunsystems dar. Diese müssen als immunologische Frontlinie einen inflammatorischen Stimulus schnell erkennen und eindämmen, um eine Dissemination und überbordende Stimulation des Immunsystems zu verhindern, welche eine vitale Bedrohnung für den Wirtsorganismus darstellen. Myeloische Zellen regulieren ihren Stoffwechsel, um diese Effektorfunktionen auszuführen und eine abgestimmte Immunantwort unter Beteiligung des spezifischen Immunsystems zu initiieren. Die Glykolyse als Eintrittstor für Kohlenstoffverbindungen ist ein zentraler Stoffwechselweg für oxidative und anaerobe Prozesse. Posttranslationale Modifikationen ihrer Enzyme ermöglichen der Zelle eine rasche Regenerierung von ATP-Reserven vor der nachfolgenden zeitintensiven Transkription Genen für Prozesse der oxidativen Phosphorylierung. Dies ermöglicht zudem eine Verwendung von Glykolysemetaboliten für die Synthese von Effektormolekülen. In diesem Kontext wurde die Rolle der PKM2 in myeloischen Zellen untersucht. Ein unvollständiger Knockout des Proteins in Makrophagen resultierte in Verschiebungen des Gleichgewichts von PKM-Oligomeren und -Isomeren mit Heraufregulation der PKM1 sowie einer präferenziellen Dimerisierung der verbleibenden PKM2 (Abbildung 5). *Pkm2*$^{\Delta myel}$ Makrophagen zeigten einen verstärkt proinflammatorischen M1-Phänotyp *in vitro* (Abbildung 8 und 9), sowie einen verstärkten Stoffwechselfluss durch Glykolyse und oxidative Phosphorylierung (Abbildung 10). Die M2-Makrophagenpolarisierung wurde hierdurch nicht beeinflusst (Abbildung 12 und 13). Unbehandelte *Pkm2*$^{\Delta myel}$ Mäuse zeigten Charakteristika eines beginnenden metabolischen Syndroms mit erhöhtem Körper -und Lebergewicht, Hypercholesterinämie und einem Anstieg langkettiger Acylcarnitine im Serum. Zudem zeigten sich Veränderungen in der Transkription von Schlüsselenzymen und Regulatoren des Leberstoffwechsels, die auf ein frühes Stadium einer Fettlebererkrankung hindeuten (Abbildung 14). *Pkm2*$^{\Delta myel}$ Mäuse zeigten mehr CD11b^{+} Ly6C^{+} Monozyten im Knochenmark, der Milz und der Leber (Abbildung 15) sowie weniger CD4^{+} Zellen und eine erhöhte CD4:CD8-Ratio in der Leber (Abbildung 16). Die Tiere reagierten mit erhöhtem Leberschaden und einer verstärkten Einwanderung myeloischer Zellen auf die Induktion einer immun-vermittelten akuten Hepatitis (Abbildung 17), was sich auch in einer gesteigerten Produktion M1-makrophagentypischer Zytokine wie IL-1β, CCL2 und IL-23 sowie einer Veränderung des Stoffwechsels im Lebergewebe hin zur aeroben Glykolyse widerspiegelte. Die pharmakologische Aktivierung der PKM2 mittels Injektion von TEPP-46 reduzierte den immun-vermittelten Leberschaden und die Transkription der pro-inflammatorischen Zytokine. Zusätzlich verringerte TEPP-46 die Transkription von *Nlpr3*, die Aktivierung von Caspase-1 und die Freisetzung von HMGB-1 nach ConA-Gabe, was einen Einfluss der myeloischen PKM2 auf die Aktivierung des NLRP3-Inflammasoms nahelegt (Abbildung 19 und 20). Zusammenfassend bestätigt die vorliegende Arbeit die vermutete Rolle der PKM2 in der Funktion myeloischer Zellen und trägt zu einem vertieften Verständnis dieser in der Entwicklung und dem Verlauf von Lebererkrankungen bei.

Publications

References

Abram, C. L., Roberge, G. L., Hu, Y., & Lowell, C. A. (2014). Comparative analysis of the efficiency and specificity of myeloid-Cre deleting strains using ROSA-EYFP reporter mice. *Journal of Immunological Methods*, *408*, 89–100. https://doi.org/10.1016/j.jim.2014.05.009

Al-Chalabi, T., Underhill, J. A., Portmann, B. C., McFarlane, I. G., & Heneghan, M. A. (2008). Impact of gender on the long-term outcome and survival of patients with autoimmune hepatitis. *Journal of Hepatology*, *48*(1), 140–147. https://doi.org/10.1016/j.jhep.2007.08.013

Alla, V., Abraham, J., Siddiqui, J., Raina, D., Wu, G. Y., Chalasani, N. P., & Bonkovsky, H. L. (2006). Autoimmune Hepatitis Triggered by Statins. *Journal of Clinical Gastroenterology*, *40*(8), 757–761. https://doi.org/10.1097/00004836-200609000-00018

Anastasiou, D., Yu, Y., Israelsen, W. J., Jiang, J.-K., Boxer, M. B., Hong, B. S., Tempel, W., Dimov, S., Shen, M., Jha, A., Yang, H., Mattaini, K. R., Metallo, C. M., Fiske, B. P., Courtney, K. D., Malstrom, S., Khan, T. M., Kung, C., Skoumbourdis, A. P., … Vander Heiden, M. G. (2012). Pyruvate kinase M2 activators promote tetramer formation and suppress tumorigenesis. *Nature Chemical Biology*, *8*(10), 839–847. https://doi.org/10.1038/nchembio.1060

Angiari, S., Runtsch, M. C., Sutton, C. E., Palsson-McDermott, E. M., Kelly, B., Rana, N., Kane, H., Papadopoulou, G., Pearce, E. L., Mills, K. H., & O'Neill, L. A. (2020). Pharmacological Activation of Pyruvate Kinase M2 Inhibits CD4+ T Cell Pathogenicity and Suppresses Autoimmunity. *Cell Metabolism*, *31*(2), 391–405.e8. https://doi.org/10.1016/j.cmet.2019.10.015

Ashizawa, K., Willingham, M., Liang, C., & Cheng, S. (1991). In vivo regulation of monomer-tetramer conversion of pyruvate kinase subtype M2 by glucose is mediated via fructose 1,6-bisphosphate. *Journal of Biological Chemistry*, *266*(25), 16842–16846. https://doi.org/10.1016/S0021-9258(18)55378-3

Baeck, C., Wehr, A., Karlmark, K. R., Heymann, F., Vucur, M., Gassler, N., Huss, S., Klussmann, S., Eulberg, D., Luedde, T., Trautwein, C., & Tacke, F. (2012). Pharmacological inhibition of the chemokine CCL2 (MCP-1) diminishes liver macrophage infiltration and steatohepatitis in chronic hepatic injury. *Gut*, *61*(3), 416–426. https://doi.org/10.1136/gutjnl-2011-300304

Bauernfeind, F. G., Horvath, G., Stutz, A., Alnemri, E. S., MacDonald, K., Speert, D., Fernandes-Alnemri, T., Wu, J., Monks, B. G., Fitzgerald, K. A., Hornung, V., & Latz, E. (2009). Cutting Edge: NF-κB Activating Pattern Recognition and Cytokine Receptors License NLRP3 Inflammasome Activation by Regulating NLRP3 Expression. *The Journal of Immunology*, *183*(2), 787–791. https://doi.org/10.4049/jimmunol.0901363

Bilzer, M., Roggel, F., & Gerbes, A. L. (2006). Role of Kupffer cells in host defense and liver disease. *Liver International*, *26*(10), 1175–1186. https://doi.org/10.1111/j.1478-3231.2006.01342.x

Bjørndal, B., Alterås, E. K., Lindquist, C., Svardal, A., Skorve, J., & Berge, R. K. (2018). Associations between fatty acid oxidation, hepatic mitochondrial function, and plasma acylcarnitine levels in mice. *Nutrition & Metabolism*, *15*(1), 10. https://doi.org/10.1186/s12986-018-0241-7

Bluemlein, K., Grüning, N.-M., Feichtinger, R. G., Lehrach, H., Kofler, B., & Ralser, M. (2011). No evidence for a shift in pyruvate kinase PKM1 to PKM2 expression during tumorigenesis. *Oncotarget*, *2*(5), 393–400. https://doi.org/10.18632/oncotarget.278

Bonder, C. S., Ajuebor, M. N., Zbytnuik, L. D., Kubes, P., & Swain, M. G. (2004). Essential Role for Neutrophil Recruitment to the Liver in Concanavalin A-Induced Hepatitis. *The Journal of Immunology*, *172*(1), 45–53. https://doi.org/10.4049/jimmunol.172.1.45

Boxer, M. B., Jiang, J., Vander Heiden, M. G., Shen, M., Skoumbourdis, A. P., Southall, N., Veith, H., Leister, W., Austin, C. P., Park, H. W., Inglese, J., Cantley, L. C., Auld, D. S., & Thomas, C. J. (2010). Evaluation of Substituted N,N'-Diarylsulfonamides as Activators of the Tumor Cell Specific M2 Isoform of Pyruvate Kinase. *Journal of Medicinal Chemistry*, *53*(3), 1048–1055. https://doi.org/10.1021/jm901577g

Brand, M. D., & Nicholls, D. G. (2011). Assessing mitochondrial dysfunction in cells. *Biochemical Journal*, *435*(2), 297–312. https://doi.org/10.1042/BJ20110162

Breuer, D. A., Pacheco, M. C., Washington, M. K., Montgomery, S. A., Hasty, A. H., & Kennedy, A. J. (2020). CD8 + T cells regulate liver injury in obesity-related nonalcoholic fatty liver disease. *American Journal of Physiology-Gastrointestinal and Liver Physiology*, *318*(2), G211–G224. https://doi.org/10.1152/ajpgi.00040.2019

Carey, C. D., Gusenleitner, D., Lipschitz, M., Roemer, M. G. M., Stack, E. C., Gjini, E., Hu, X., Redd, R., Freeman, G. J., Neuberg, D., Hodi, F. S., Liu, X. S., Shipp, M. A., & Rodig, S. J. (2017). Topological analysis reveals a PD-L1-associated microenvironmental niche for Reed-Sternberg cells in Hodgkin lymphoma. *Blood*, *130*(22), 2420–2430. https://doi.org/10.1182/blood-2017-03-770719

Cheng, Y., Feng, Y., Xia, Z., Li, X., & Rong, J. (2017). ω-Alkynyl arachidonic acid promotes anti-inflammatory macrophage M2 polarization against acute myocardial infarction via regulating the cross-talk between PKM2, HIF-1α and iNOS. *Biochimica et Biophysica Acta - Molecular and Cell Biology of Lipids*, *1862*(12), 1595–1605. https://doi.org/10.1016/j.bbalip.2017.09.009

Clausen, B. E., Burkhardt, C., Reith, W., Renkawitz, R., & Förster, I. (1999). Conditional gene targeting in macrophages and granulocytes using LysMcre mice. *Transgenic research*, *8*(4), 265–77. https://doi.org/10.1023/a:1008942828960

Cohen, H. B., Briggs, K. T., Marino, J. P., Ravid, K., Robson, S. C., & Mosser, D. M. (2013). TLR stimulation initiates a CD39-based autoregulatory mechanism that limits macrophage inflammatory responses. *Blood*, *122*(11), 1935–1945. https://doi.org/10.1182/blood-2013-04-496216

David, C. J., Chen, M., Assanah, M., Canoll, P., & Manley, J. L. (2010). HnRNP proteins controlled by c-Myc deregulate pyruvate kinase mRNA splicing in cancer. *Nature*, *463*(7279), 364–368. https://doi.org/10.1038/nature08697

Deprez, J., Vertommen, D., Alessi, D. R., Hue, L., & Rider, M. H. (1997). Phosphorylation and Activation of Heart 6-Phosphofructo-2-kinase by Protein Kinase B and Other Protein Kinases of the Insulin Signaling Cascades. *Journal of Biological Chemistry*, *272*(28), 17269–17275. https://doi.org/10.1074/jbc.272.28.17269

Divakaruni, A. S., Paradyse, A., Ferrick, D. A., Murphy, A. N., & Jastroch, M. (2014). Analysis and Interpretation of Microplate-Based Oxygen Consumption and pH Data. *Methods in enzymology* (1st ed., pp. 309–354). Elsevier Inc. https://doi.org/10.1016/B978-0-12-801415-8.00016-3

Donaldson, P. T. (2004). Genetics of liver disease: immunogenetics and disease pathogenesis. *Gut*, *53*(4), 599–608. https://doi.org/10.1136/gut.2003.031732

Dos Anjos Cassado, A. (2017). F4/80 as a Major Macrophage Marker: The Case of the Peritoneum and Spleen. In M. Kloc (Ed.), *Macrophages: Origin, functions and biointervention* (pp. 161–179). Springer International Publishing. https://doi.org/10.1007/978-3-319-54090-0_7

Eckardt, D., Theis, M., Döring, B., Speidel, D., Willecke, K., & Ott, T. (2004). Spontaneous ectopic recombination in cell-type-specific Cre mice removes loxP -flanked marker cassettes in vivo. *Genesis*, *38*(4), 159–165. https://doi.org/10.1002/gene.20011

Eigenbrodt, E., Reinacher, M., Scheefers-Borchel, U., Scheefers, H., & Friis, R. (1992). Double role for pyruvate kinase type M2 in the expansion of phosphometabolite pools found in tumor cells. *Critical reviews in oncogenesis*, *3*(1-2), 91–115. https://doi.org/10.1007/978-3-0348-8950-6_2

El-Khoury, T. G., Bahr, G. M., & Echtay, K. S. (2011). Muramyl-dipeptide-induced mitochondrial proton leak in macrophages is associated with upregulation of uncoupling protein 2 and the production of reactive oxygen and reactive nitrogen species. *FEBS Journal*, *278*(17), 3054–3064. https://doi.org/10.1111/j.1742-4658.2011.08226.x

Enooku, K., Nakagawa, H., Fujiwara, N., Kondo, M., Minami, T., Hoshida, Y., Shibahara, J., Tateishi, R., & Koike, K. (2019). Altered serum acylcarnitine profile is associated with the status of nonalcoholic fatty liver disease (NAFLD) and NAFLD-related hepatocellular carcinoma. *Scientific Reports*, *9*(1), 10663. https://doi.org/10.1038/s41598-019-47216-2

Fukuzumi, M., Shinomiya, H., Shimizu, Y., Ohishi, K., & Utsumi, S. (1996). Endotoxin-induced enhancement of glucose influx into murine peritoneal macrophages via GLUT1. *Infection and immunity*, *64*(1), 108–12. https://doi.org/10.1128/IAI.64.1.108-112.1996

Furuta, E., Pai, S. K., Zhan, R., Bandyopadhyay, S., Watabe, M., Mo, Y. Y., Hirota, S., Hosobe, S., Tsukada, T., Miura, K., Kamada, S., Saito, K., Iiizumi, M., Liu, W., Ericsson, J., & Watabe, K. (2008). Fatty acid synthase gene is up-regulated by hypoxia via activation of Akt and sterol regulatory element binding protein-1. *Cancer Research*, *68*(4), 1003–1011. https://doi.org/10.1158/0008-5472.CAN-07-2489

Glorieux, C., Xia, X., He, Y.-Q., Hu, Y., Cremer, K., Robert, A., Liu, J., Wang, F., Ling, J., Chiao, P. J., & Huang, P. (2021). Regulation of PD-L1 expression in K-ras-driven cancers through ROS-mediated FGFR1 signaling. *Redox Biology*, *38*, 101780. https://doi.org/10.1016/j.redox.2020.101780

Grundy, S. M., Cleeman, J. I., Daniels, S. R., Donato, K. A., Eckel, R. H., Franklin, B. A., Gordon, D. J., Krauss, R. M., Savage, P. J., Smith, S. C., Spertus, J. A., & Costa, F. (2005). Diagnosis and Management of the Metabolic Syndrome. *Circulation*, *112*(17), 322–327. https://doi.org/10.1161/CIRCULATIONAHA.105.169405

Gschwandtner, M., Derler, R., & Midwood, K. S. (2019). More Than Just Attractive: How CCL2 Influences Myeloid Cell Behavior Beyond Chemotaxis. *Frontiers in Immunology*, *10*(December), 1–29. https://doi.org/10.3389/fimmu.2019.02759

Hansel, C., Erschfeld, S., Baues, M., Lammers, T., Weiskirchen, R., Trautwein, C., Kroy, D. C., & Drescher, H. K. (2019). The Inhibitory T Cell Receptors PD1 and 2B4 Are Differentially Regulated on CD4 and CD8 T Cells in a Mouse Model of Non-alcoholic Steatohepatitis. *Frontiers in Pharmacology*, *10*(March), 1–16. https://doi.org/10.3389/fphar.2019.00244

Hard, G. C. (1970). Some biochemical aspects of the immune macrophage. *British journal of experimental pathology*, *51*(1), 97–105. http://www.ncbi.nlm.nih.gov/pubmed/5434449%7B%5C%%7D0Ahttp://www.pubmedcentral.nih.gov/articlerender.fcgi?artid=PMC2072214%20http://www.ncbi.nlm.nih.gov/pubmed/5434449%20http://www.pubmedcentral.nih.gov/articlerender.fcgi?artid=PMC2072214

Harrison, J. E., & Schultz, J. (1976). Studies on the chlorinating activity of myeloperoxidase. *Journal of Biological Chemistry*, *251*(5), 1371–1374. https://doi.org/10.1016/S0021-9258(17)33749-3

He, J. Q., Katschke, K. J., Gribling, P., Suto, E., Lee, W. P., Diehl, L., Eastham-Anderson, J., Ponakala, A., Komuves, L., Egen, J. G., & van Lookeren Campagne, M. (2013). CRIg mediates early Kupffer cell responses to adenovirus. *Journal of leukocyte biology*, *93*(2), 301–6. https://doi.org/10.1189/jlb.0612311

Heap, R. E., Marín-Rubio, J. L., Peltier, J., Heunis, T., Dannoura, A., Moore, A., & Trost, M. (2020). Proteomics characterisation of the L929 cell supernatant and its role in BMDM differentiation. *bioRxiv*, 2020.08.20.259515. https://doi.org/10.1101/2020.08.20.259515

Heffner, C. S., Herbert Pratt, C., Babiuk, R. P., Sharma, Y., Rockwood, S. F., Donahue, L. R., Eppig, J. T., & Murray, S. A. (2012). Supporting conditional mouse mutagenesis with a comprehensive cre characterization resource. *Nature Communications*, *3*(1), 1218. https://doi.org/10.1038/ncomms2186

Heneghan, M. A., Yeoman, A. D., Verma, S., Smith, A. D., & Longhi, M. S. (2013). Autoimmune hepatitis. *The Lancet*, *382*(9902), 1433–1444. https://doi.org/10.1016/S0140-6736(12)62163-1

Heppner, D. E., Dustin, C. M., Liao, C., Hristova, M., Veith, C., Little, A. C., Ahlers, B. A., White, S. L., Deng, B., Lam, Y.-W., Li, J., & van der Vliet, A. (2018). Direct cysteine sulfenylation drives activation of the Src kinase. *Nature Communications*, *9*(1), 4522. https://doi.org/10.1038/s41467-018-06790-1

Heymann, F., Hamesch, K., Weiskirchen, R., & Tacke, F. (2015). The concanavalin A model of acute hepatitis in mice. *Laboratory Animals*, *49*(1_suppl), 12–20. https://doi.org/10.1177/0023677215572841

Hitosugi, T., Kang, S., Vander Heiden, M. G., Chung, T.-W., Elf, S., Lythgoe, K., Dong, S., Lonial, S., Wang, X., Chen, G. Z., Xie, J., Gu, T.-L., Polakiewicz, R. D., Roesel, J. L., Boggon, T. J., Khuri, F. R., Gilliland, D. G., Cantley, L. C., Kaufman, J., & Chen, J. (2009). Tyrosine Phosphorylation Inhibits PKM2 to Promote the Warburg Effect and Tumor Growth. *Science Signaling*, *2*(97), ra73–ra73. https://doi.org/10.1126/scisignal.2000431

Horst, A. K., Neumann, K., Diehl, L., & Tiegs, G. (2016). Modulation of liver tolerance by conventional and nonconventional antigen-presenting cells and regulatory immune cells. *Cellular & Molecular Immunology*, *13*(3), 277–292. https://doi.org/10.1038/cmi.2015.112

Hou, P.-p., Luo, L.-j., Chen, H.-z., Chen, Q.-t., Bian, X.-l., Wu, S.-f., Zhou, J.-x., Zhao, W.-x., Liu, J.-m., Wang, X.-m., Zhang, Z.-y., Yao, L.-m., Chen, Q., Zhou, D., & Wu, Q. (2020). Ectosomal PKM2 Promotes HCC by Inducing Macrophage Differentiation and Remodeling the Tumor Microenvironment. *Molecular Cell*, *78*(6), 1192–1206.e10. https://doi.org/10.1016/j.molcel.2020.05.004

Israelsen, W. J., Dayton, T. L., Davidson, S. M., Fiske, B. P., Hosios, A. M., Bellinger, G., Li, J., Yu, Y., Sasaki, M., Horner, J. W., Burga, L. N., Xie, J., Jurczak, M. J., Depinho, R. A., Clish, C. B., Jacks, T., Kibbey, R. G., Wulf, G. M., Vizio, D. D., … Heiden, M. G. V. (2013). PKM2 Isoform-Specific Deletion Reveals a Differential Requirement for Pyruvate Kinase in Tumor Cells. *Cell*, *155*(2), 397–409. https://doi.org/10.1016/j.cell.2013.09.025

Jha, A. K., Huang, S. C.-C., Sergushichev, A., Lampropoulou, V., Ivanova, Y., Loginicheva, E., Chmielewski, K., Stewart, K. M., Ashall, J., Everts, B., Pearce, E. J., Driggers, E. M., & Artyomov, M. N. (2015). Network Integration of Parallel Metabolic and Transcriptional Data Reveals Metabolic Modules that Regulate Macrophage Polarization. *Immunity*, *42*(3), 419–430. https://doi.org/10.1016/j.immuni.2015.02.005

Jiang, J., Boxer, M. B., Vander Heiden, M. G., Shen, M., Skoumbourdis, A. P., Southall, N., Veith, H., Leister, W., Austin, C. P., Park, H. W., Inglese, J., Cantley, L. C., Auld, D. S., & Thomas, C. J. (2010). Evaluation of thieno[3,2-b]pyrrole[3,2-d]pyridazinones as activators of the tumor cell specific M2 isoform of pyruvate kinase. *Bioorganic and Medicinal Chemistry Letters*, *20*(11), 3387–3393. https://doi.org/10.1016/j.bmcl.2010.04.015

Jiao, N., Baker, S. S., Chapa-Rodriguez, A., Liu, W., Nugent, C. A., Tsompana, M., Mastrandrea, L., Buck, M. J., Baker, R. D., Genco, R. J., Zhu, R., & Zhu, L. (2018). Suppressed hepatic bile acid signalling despite elevated production of primary and secondary bile acids in NAFLD. *Gut*, *67*(10), 1881–1891. https://doi.org/10.1136/gutjnl-2017-314307

Ju, C., & Tacke, F. (2016). Hepatic macrophages in homeostasis and liver diseases: from pathogenesis to novel therapeutic strategies. *Cellular and Molecular Immunology*, *13*(October 2015), 1–12. https://doi.org/10.1038/cmi.2015.104

Kara, E. E., McKenzie, D. R., Bastow, C. R., Gregor, C. E., Fenix, K. A., Ogunniyi, A. D., Paton, J. C., Mack, M., Pombal, D. R., Seillet, C., Dubois, B., Liston, A., MacDonald, K. P. A., Belz, G. T., Smyth, M. J., Hill, G. R., Comerford, I., & McColl, S. R. (2015). CCR2 defines in vivo development and homing of IL-23-driven GM-CSF-producing Th17 cells. *Nature Communications*, *6*(1), 8644. https://doi.org/10.1038/ncomms9644

Karlmark, K. R., Weiskirchen, R., Zimmermann, H. W., Gassler, N., Ginhoux, F., Weber, C., Merad, M., Luedde, T., Trautwein, C., & Tacke, F. (2009). Hepatic recruitment of the inflammatory Gr1 + monocyte subset upon liver injury promotes hepatic fibrosis. *Hepatology*, *50*(1), 261–274. https://doi.org/10.1002/hep.22950

Keller, K. E., Tan, I. S., & Lee, Y.-S. (2012). SAICAR Stimulates Pyruvate Kinase Isoform M2 and Promotes Cancer Cell Survival in Glucose-Limited Conditions. *Science*, *338*(6110), 1069–1072. https://doi.org/10.1126/science.1224409

Kong, Q., Li, N., Cheng, H., Zhang, X., Cao, X., Qi, T., Dai, L., Zhang, Z., Chen, X., Li, C., Li, Y., Xue, B., Fang, L., Liu, L., & Ding, Z. (2019). HSPA12A Is a Novel Player in Nonalcoholic Steatohepatitis via Promoting Nuclear PKM2-Mediated M1 Macrophage Polarization. *Diabetes*, *68*(2), 361–376. https://doi.org/10.2337/db18-0035

Konkel, J. E., Frommer, F., Leech, M. D., Yagita, H., Waisman, A., & Anderton, S. M. (2010). PD-1 signalling in CD4 + T cells restrains their clonal expansion to an immunogenic stimulus, but is not critically required for peptide-induced tolerance. *Immunology*, *130*(1), 92–102. https://doi.org/10.1111/j.1365-2567.2009.03216.x

Lafdil, F., Wang, H., Park, O., Zhang, W., Moritoki, Y., Yin, S., Fu, X. Y., Gershwin, M. E., Lian, Z.-X., & Gao, B. (2009). Myeloid STAT3 Inhibits T Cell-Mediated Hepatitis by Regulating T Helper 1 Cytokine and Interleukin-17 Production. *Gastroenterology*, *137*(6), 2125–2135.e2. https://doi.org/10.1053/j.gastro.2009.08.004

Lampropoulou, V., Sergushichev, A., Bambouskova, M., Nair, S., Vincent, E. E., Loginicheva, E., Cervantes-Barragan, L., Ma, X., Huang, S. C. C., Griss, T., Weinheimer, C. J., Khader, S., Randolph, G. J., Pearce, E. J., Jones, R. G., Diwan, A., Diamond, M. S., & Artyomov, M. N. (2016). Itaconate Links Inhibition of Succinate Dehydrogenase with Macrophage Metabolic Remodeling and Regulation of Inflammation. *Cell Metabolism*, *24*(1), 158–166. https://doi.org/10.1016/j.cmet.2016.06.004

Lin, R., Zhang, J., Zhou, L., & Wang, B. (2016). Altered function of monocytes/macrophages in patients with autoimmune hepatitis. *Molecular Medicine Reports*, *13*(5), 3874–3880. https://doi.org/10.3892/mmr.2016.4998

Liu, V. M., Howell, A. J., Hosios, A. M., Li, Z., Israelsen, W. J., & Vander Heiden, M. G. (2020). Cancer-associated mutations in human pyruvate kinase M2 impair enzyme activity. *FEBS Letters*, *594*(4), 646–664. https://doi.org/10.1002/1873-3468.13648

Longhi, M. S., Hussain, M. J., Mitry, R. R., Arora, S. K., Mieli-Vergani, G., Vergani, D., & Ma, Y. (2006). Functional Study of CD4 + CD25 + Regulatory T Cells in Health and Autoimmune Hepatitis. *The Journal of Immunology*, *176*(7), 4484–4491. https://doi.org/10.4049/jimmunol.176.7.4484

Lunt, S. Y., & Vander Heiden, M. G. (2011). Aerobic glycolysis: Meeting the metabolic requirements of cell proliferation. *Annual Review of Cell and Developmental Biology*, *27*, 441–464. https://doi.org/10.1146/annurev-cellbio-092910-154237

Luo, W., Hu, H., Chang, R., Zhong, J., Knabel, M., O'Meally, R., Cole, R. N., Pandey, A., & Semenza, G. L. (2011). Pyruvate kinase M2 is a PHD3-stimulated coactivator for hypoxia-inducible factor 1. *Cell*, *145*(5), 732–744. https://doi.org/10.1016/j.cell.2011.03.054

Ma, C., Kesarwala, A. H., Eggert, T., Medina-Echeverz, J., Kleiner, D. E., Jin, P., Stroncek, D. F., Terabe, M., Kapoor, V., ElGindi, M., Han, M., Thornton, A. M., Zhang, H., Egger, M., Luo, J., Felsher, D. W., McVicar, D. W., Weber, A., Heikenwalder, M., & Greten, T. F. (2016). NAFLD causes selective CD4+ T lymphocyte loss and promotes hepatocarcinogenesis. *Nature*, *531*(7593), 253–257. https://doi.org/10.1038/nature16969

Ma, H., Zhang, J., Zhou, L., Wen, S., Tang, H.-Y., Jiang, B., Zhang, F., Suleman, M., Sun, D., Chen, A., Zhao, W., Lin, F., Tsau, M.-T., Shih, L.-M., Xie, C., Li, X., Lin, D., Hung, L.-M., Cheng, M.-L., & Li, Q. (2020). c-Src Promotes Tumorigenesis and Tumor Progression by Activating PFKFB3. *Cell Reports*, *30*(12), 4235–4249.e6. https://doi.org/10.1016/j.celrep.2020.03.005

Ma, K. L., Ruan, X. Z., Powis, S. H., Chen, Y., Moorhead, J. F., & Varghese, Z. (2008). Inflammatory stress exacerbates lipid accumulation in hepatic cells and fatty livers of apolipoprotein E knockout mice. *Hepatology*, *48*(3), 770–781. https://doi.org/10.1002/hep.22423

Manns, M. P., Griffin, K. J., Sullivan, K. F., & Johnson, E. F. (1991). LKM-1 autoantibodies recognize a short linear sequence in P450IID6, a cytochrome P-450 monooxygenase. *Journal of Clinical Investigation*, *88*(4), 1370–1378. https://doi.org/10.1172/JCI115443

Manns, M. P. (2011). Autoimmune Hepatitis: The Dilemma of Rare Diseases. *Gastroenterology*, *140*(7), 1874–1876. https://doi.org/10.1053/j.gastro.2011.04.026

Mariathasan, S., Weiss, D. S., Newton, K., McBride, J., O'Rourke, K., Roose-Girma, M., Lee, W. P., Weinrauch, Y., Monack, D. M., & Dixit, V. M. (2006). Cryopyrin activates the inflammasome in response to toxins and ATP. *Nature*, *440*(7081), 228–232. https://doi.org/10.1038/nature04515

Martinez, F. O., & Gordon, S. (2014). The M1 and M2 paradigm of macrophage activation: time for reassessment. *F1000Prime Reports*, *6*(March), 13. https://doi.org/10.12703/P6-13

Meoni, G., Lorini, S., Monti, M., Madia, F., Corti, G., Luchinat, C., Zignego, A. L., Tenori, L., & Gragnani, L. (2019). The metabolic fingerprints of HCV and HBV infections studied by Nuclear Magnetic Resonance Spectroscopy. *Scientific Reports*, *9*(1), 4128. https://doi.org/10.1038/s41598-019-40028-4

Mills, C. D. (2001). Macrophage Arginine Metabolism to Ornithine/Urea or Nitric Oxide/Citrulline: A Life or Death Issue. *Critical Reviews™ in Immunology*, *21*(5), 28. https://doi.org/10.1615/CritRevImmunol.v21.i5.10

Miura, K., Yang, L., van Rooijen, N., Ohnishi, H., & Seki, E. (2012). Hepatic recruitment of macrophages promotes nonalcoholic steatohepatitis through CCR2. *American Journal of Physiology - Gastrointestinal and Liver Physiology*, *302*(11), 1310–1321. https://doi.org/10.1152/ajpgi.00365.2011

Morgan, H. P., O'Reilly, F. J., Wear, M. A., O'Neill, J. R., Fothergill-Gilmore, L. A., Hupp, T., & Walkinshaw, M. D. (2013). M2 pyruvate kinase provides a mechanism for nutrient sensing and regulation of cell proliferation. *Proceedings of the National Academy of Sciences*, *110*(15), 5881–5886. https://doi.org/10.1073/pnas.1217157110

Morgantini, C., Jager, J., Li, X., Levi, L., Azzimato, V., Sulen, A., Barreby, E., Xu, C., Tencerova, M., Näslund, E., Kumar, C., Verdeguer, F., Straniero, S., Hultenby, K., Björkström, N. K., Ellis, E., Rydén, M., Kutter, C., Hurrell, T., … Aouadi, M. (2019). Liver macrophages regulate systemic metabolism through non-inflammatory factors. *Nature Metabolism*, *1*(4), 445–459. https://doi.org/10.1038/s42255-019-0044-9

Mossanen, J. C., Krenkel, O., Ergen, C., Govaere, O., Liepelt, A., Puengel, T., Heymann, F., Kalthoff, S., Lefebvre, E., Eulberg, D., Luedde, T., Marx, G., Strassburg, C. P., Roskams, T., Trautwein, C., & Tacke, F. (2016). Chemokine (C-C motif) receptor 2-positive monocytes aggravate the early phase of acetaminophen-induced acute liver injury. *Hepatology*, *64*(5), 1667–1682. https://doi.org/10.1002/hep.28682

Murphy, M. P. (2009). How mitochondria produce reactive oxygen species. *Biochemical Journal*, *417*(1), 1–13. https://doi.org/10.1042/BJ20081386

Noguchi, T., Inoue, H., & Tanaka, T. (1986). The M1- and M2-type isozymes of rat pyruvate kinase are produced from the same gene by alternative RNA splicing. *Journal of Biological Chemistry*, *261*(29), 13807–13812. https://doi.org/10.1016/S0021-9258(18)67091-7

O'Neill, L. A. J., Kishton, R. J., & Rathmell, J. (2016). A guide to immunometabolism for immunologists. *Nature Reviews Immunology*, *16*(9), 553–565. https://doi.org/10.1038/nri.2016.70

Orecchioni, M., Ghosheh, Y., Pramod, A. B., & Ley, K. (2019). Macrophage Polarization: Different Gene Signatures in M1(LPS+) vs. Classically and M2(LPS–) vs. Alternatively Activated Macrophages. *Frontiers in Immunology*, *10*(MAY), 1–14. https://doi.org/10.3389/fimmu.2019.01084

Otto, G. P., Rathkolb, B., Oestereicher, M. A., Lengger, C. J., Moerth, C., Micklich, K., Fuchs, H., Gailus-Durner, V., Wolf, E., & Hrabě de Angelis, M. (2016). Clinical Chemistry Reference Intervals for C57BL/6J, C57BL/6N, and C3HeB/FeJ Mice (Mus musculus). *Journal of the American Association for Laboratory Animal Science : JAALAS*, *55*(4), 375–86. http://www.ncbi.nlm.nih.gov/pubmed/27423143%20http://www.pubmedcentral.nih.gov/articlerender.fcgi?artid=PMC4943607

Palsson-McDermott, E. M., Curtis, A. M., Goel, G., Lauterbach, M. A., Sheedy, F. J., Gleeson, L. E., van den Bosch, M. W., Quinn, S. R., Domingo-Fernandez, R., Johnston, D. G., Jiang, J.-k., Israelsen, W. J., Keane, J., Thomas, C., Clish, C., Vander Heiden, M., Xavier, R. J., & O'Neill, L. A. (2015). Pyruvate Kinase M2 Regulates Hif-1α Activity and IL-1β Induction and Is a Critical Determinant of the Warburg Effect in LPS-Activated Macrophages. *Cell Metabolism*, *21*(1), 65–80. https://doi.org/10.1016/j.cmet.2014.12.005

Patterson, R. E., Kalavalapalli, S., Williams, C. M., Nautiyal, M., Mathew, J. T., Martinez, J., Reinhard, M. K., McDougall, D. J., Rocca, J. R., Yost, R. A., Cusi, K., Garrett, T. J., & Sunny, N. E. (2016). Lipotoxicity in steatohepatitis occurs despite an increase in tricarboxylic acid cycle

activity. *American Journal of Physiology-Endocrinology and Metabolism*, *310*(7), E484–E494. https://doi.org/10.1152/ajpendo.00492.2015

Peng, K.-Y., Watt, M. J., Rensen, S., Greve, J. W., Huynh, K., Jayawardana, K. S., Meikle, P. J., & Meex, R. C. (2018). Mitochondrial dysfunction-related lipid changes occur in nonalcoholic fatty liver disease progression. *Journal of Lipid Research*, *59*(10), 1977–1986. https://doi.org/10.1194/jlr.M085613

Pompura, S. L., Wagner, A., Kitz, A., LaPerche, J., Yosef, N., Dominguez-Villar, M., & Hafler, D. A. (2021). Oleic acid restores suppressive defects in tissue-resident FOXP3 Tregs from patients with multiple sclerosis. *Journal of Clinical Investigation*, *131*(2). https://doi.org/10.1172/JCI138519

Prakasam, G., Iqbal, M. A., Bamezai, R. N., & Mazurek, S. (2018). Posttranslational modifications of pyruvate kinase M2: Tweaks that benefit cancer. https://doi.org/10.3389/fonc.2018.00022

Rapp, M., Wintergerst, M. W., Kunz, W. G., Vetter, V. K., Knott, M. M., Lisowski, D., Haubner, S., Moder, S., Thaler, R., Eiber, S., Meyer, B., Röhrle, N., Piseddu, I., Grassmann, S., Layritz, P., Kühnemuth, B., Stutte, S., Bourquin, C., von Andrian, U. H., … Anz, D. (2019). CCL22 controls immunity by promoting regulatory T cell communication with dendritic cells in lymph nodes. *Journal of Experimental Medicine*, *216*(5), 1170–1181. https://doi.org/10.1084/jem.20170277

Reddy, M., Eirikis, E., Davis, C., Davis, H. M., & Prabhakar, U. (2004). Comparative analysis of lymphocyte activation marker expression and cytokine secretion profile in stimulated human peripheral blood mononuclear cell cultures: an in vitro model to monitor cellular immune function. *Journal of Immunological Methods*, *293*(1-2), 127–142. https://doi.org/10.1016/j.jim.2004.07.006

Reuter, S. E., & Evans, A. M. (2012). Carnitine and Acylcarnitines. *Clinical Pharmacokinetics*, *51*(9), 553–572. https://doi.org/10.2165/11633940-000000000-00000

Ricchi, M., Odoardi, M. R., Carulli, L., Anzivino, C., Ballestri, S., Pinetti, A., Fantoni, L. I., Marra, F., Bertolotti, M., Banni, S., Lonardo, A., Carulli, N., & Loria, P. (2009). Differential effect of oleic and palmitic acid on lipid accumulation and apoptosis in cultured hepatocytes. *Journal of Gastroenterology and Hepatology*, *24*(5), 830–840. https://doi.org/10.1111/j.1440-1746.2008.05733.x

Rodríguez-Prados, J.-C., Través, P. G., Cuenca, J., Rico, D., Aragonés, J., Martín-Sanz, P., Cascante, M., & Boscá, L. (2010). Substrate Fate in Activated Macrophages: A Comparison between Innate, Classic, and Alternative Activation. *The Journal of Immunology*, *185*(1), 605–614. https://doi.org/10.4049/jimmunol.0901698

Savio, L. E. B., de Andrade Mello, P., Santos, S. A. C. S., de Sousa, J. C., Oliveira, S. D. S., Minshall, R. D., Kurtenbach, E., Wu, Y., Longhi, M. S., Robson, S. C., & Coutinho-Silva, R. (2020). P2X7 receptor activation increases expression of caveolin-1 and formation of macrophage lipid rafts, thereby boosting CD39 activity. *Journal of Cell Science*, *133*(5), jcs237560. https://doi.org/10.1242/jcs.237560

Schümann, J., Wolf, D., Pahl, A., Brune, K., Papadopoulos, T., van Rooijen, N., & Tiegs, G. (2000). Importance of Kupffer Cells for T-Cell-Dependent Liver Injury in Mice. *The American Journal of Pathology*, *157*(5), 1671–1683. https://doi.org/10.1016/S0002-9440(10)64804-3

Semenza, G., Roth, P., Fang, H., & Wang, G. (1994). Transcriptional regulation of genes encoding glycolytic enzymes by hypoxia-inducible factor 1. *Journal of Biological Chemistry*, *269*(38), 23757–23763. https://doi.org/10.1016/S0021-9258(17)31580-6

Semenza, G. L., Jiang, B.-H., Leung, S. W., Passantino, R., Concordet, J.-P., Maire, P., & Giallongo, A. (1996). Hypoxia Response Elements in the Aldolase A, Enolase 1, and Lactate Dehydrogenase A Gene Promoters Contain Essential Binding Sites for Hypoxia-inducible Factor 1. *Journal of Biological Chemistry*, *271*(51), 32529–32537. https://doi.org/10.1074/jbc.271.51.32529

Shirai, T., Nazarewicz, R. R., Wallis, B. B., Yanes, R. E., Watanabe, R., Hilhorst, M., Tian, L., Harrison, D. G., Giacomini, J. C., Assimes, T. L., Goronzy, J. J., & Weyand, C. M. (2016). The glycolytic

enzyme PKM2 bridges metabolic and inflammatory dysfunction in coronary artery disease. *Journal of Experimental Medicine*, *213*(3), 337–354. https://doi.org/10.1084/jem.20150900

Song, P., Zhang, J., Zhang, Y., Shu, Z., Xu, P., He, L., Yang, C., Zhang, J., Wang, H., Li, Y., & Li, Q. (2017). Hepatic recruitment of CD11b+Ly6C+ inflammatory monocytes promotes hepatic ischemia/reperfusion injury. *International Journal of Molecular Medicine*, *41*(2), 935–945. https://doi.org/10.3892/ijmm.2017.3315

Stein, M., Keshav, S., Harris, N., & Gordon, S. (1992). Interleukin 4 potently enhances murine macrophage mannose receptor activity: a marker of alternative immunologic macrophage activation. *Journal of Experimental Medicine*, *176*(1), 287–292. https://doi.org/10.1084/jem.176.1.287

Sternberg, N., & Hamilton, D. (1981). Bacteriophage P1 site-specific recombination. *Journal of Molecular Biology*, *150*(4), 467–486. https://doi.org/10.1016/0022-2836(81)90375-2

Stuart, J. A., Fonseca, J., Moradi, F., Cunningham, C., Seliman, B., Worsfold, C. R., Dolan, S., Abando, J., & Maddalena, L. A. (2018). How Supraphysiological Oxygen Levels in Standard Cell Culture Affect Oxygen-Consuming Reactions. *Oxidative Medicine and Cellular Longevity*, *2018*, 1–13. https://doi.org/10.1155/2018/8238459

Tannahill, G. M., Curtis, A. M., Adamik, J., Palsson-McDermott, E. M., McGettrick, A. F., Goel, G., Frezza, C., Bernard, N. J., Kelly, B., Foley, N. H., Zheng, L., Gardet, A., Tong, Z., Jany, S. S., Corr, S. C., Haneklaus, M., Caffrey, B. E., Pierce, K., Walmsley, S., … O'Neill, L. A. J. (2013). Succinate is an inflammatory signal that induces IL-1β through HIF-1α. *Nature*, *496*(7444), 238–242. https://doi.org/10.1038/nature11986

Tiegs, G., Hentschel, J., & Wendel, A. (1992). A T cell-dependent experimental liver injury in mice inducible by concanavalin A. *Journal of Clinical Investigation*, *90*(1), 196–203. https://doi.org/10.1172/JCI115836

Treichel, U., McFarlane, B. M., Seki, T., Krawitt, E. L., Alessi, N., Stickel, F., McFarlane, I. G., Kiyosawa, K., Furuta, S., Freni, M. A., Gerken, G., & Büschenfelde, K.-H. M. Z. (1994). Demographics of anti-asialoglycoprotein receptor autoantibodies in autoimmune hepatitis. *Gastroenterology*, *107*(3), 799–804. https://doi.org/10.1016/0016-5085(94)90129-5

Tu, C.-t., Yao, Q.-y., Xu, B.-l., & Zhang, S.-c. (2013). Curcumin Protects Against Concanavalin A-Induced Hepatitis in Mice Through Inhibiting the Cytoplasmic Translocation and Expression of High Mobility Group Box 1. *Inflammation*, *36*(1), 206–215. https://doi.org/10.1007/s10753-012-9536-4

Van den Bossche, J., Baardman, J., Otto, N. A., van der Velden, S., Neele, A. E., van den Berg, S. M., Luque-Martin, R., Chen, H.-J., Boshuizen, M. C., Ahmed, M., Hoeksema, M. A., de Vos, A. F., & de Winther, M. P. (2016). Mitochondrial Dysfunction Prevents Repolarization of Inflammatory Macrophages. *Cell Reports*, *17*(3), 684–696. https://doi.org/10.1016/j.celrep.2016.09.008

van de Wetering, C., Aboushousha, R., Manuel, A. M., Chia, S. B., Erickson, C., MacPherson, M. B., van der Velden, J. L., Anathy, V., Dixon, A. E., Irvin, C. G., Poynter, M. E., van der Vliet, A., Wouters, E. F. M., Reynaert, N. L., & Janssen-Heininger, Y. M. W. (2020). Pyruvate Kinase M2 Promotes Expression of Proinflammatory Mediators in House Dust Mite–Induced Allergic Airways Disease. *The Journal of Immunology*, *204*(4), 763–774. https://doi.org/10.4049/jimmunol.1901086

Van Herck, M. A., Weyler, J., Kwanten, W. J., Dirinck, E. L., De Winter, B. Y., Francque, S. M., & Vonghia, L. (2019). The Differential Roles of T Cells in Non-alcoholic Fatty Liver Disease and Obesity. *Frontiers in Immunology*, *10*(FEB). https://doi.org/10.3389/fimmu.2019.00082

Vannella, K. M., Barron, L., Borthwick, L. A., Kindrachuk, K. N., Narasimhan, P. B., Hart, K. M., Thompson, R. W., White, S., Cheever, A. W., Ramalingam, T. R., & Wynn, T. A. (2014). Incomplete Deletion of IL-4Rα by LysMCre Reveals Distinct Subsets of M2 Macrophages Controlling Inflammation and Fibrosis in Chronic Schistosomiasis (J. W. Kazura, Ed.). *PLoS Pathogens*, *10*(9), e1004372. https://doi.org/10.1371/journal.ppat.1004372

Vento, S., Garofano, T., Di Perri, G., Dolci, L., Concia, E., & Bassetti, D. (1991). Identification of hepatitis A virus as a trigger for autoimmune chronic hepatitis type 1 in susceptible individuals. *Lancet*, *337*(8751), 1183–7. https://doi.org/10.1016/0140-6736(91)92858-y

Verreck, F. A. W., de Boer, T., Langenberg, D. M. L., Hoeve, M. A., Kramer, M., Vaisberg, E., Kastelein, R., Kolk, A., de Waal-Malefyt, R., & Ottenhoff, T. H. M. (2004). Human IL-23-producing type 1 macrophages promote but IL-10-producing type 2 macrophages subvert immunity to (myco)bacteria. *Proceedings of the National Academy of Sciences*, *101*(13), 4560–4565. https://doi.org/10.1073/pnas.0400983101

Vooijs, M., Jonkers, J., & Berns, A. (2001). A highly efficient ligand-regulated Cre recombinase mouse line shows that LoxP recombination is position dependent. *EMBO reports*, *2*(4), 292–297. https://doi.org/10.1093/embo-reports/kve064

Walls, J. F., Subleski, J. J., Palmieri, E. M., Gonzalez-Cotto, M., Gardiner, C. M., McVicar, D. W., & Finlay, D. K. (2020). Metabolic but not transcriptional regulation by PKM2 is important for natural killer cell responses. *eLife*, *9*, 1–23. https://doi.org/10.7554/eLife.59166

Wang, F., Wang, K., Xu, W., Zhao, S., Ye, D., Wang, Y., Xu, Y., Zhou, L., Chu, Y., Zhang, C., Qin, X., Yang, P., & Yu, H. (2017). SIRT5 Desuccinylates and Activates Pyruvate Kinase M2 to Block Macrophage IL-1b Production and to Prevent DSS-Induced Colitis in Mice. *Cell Reports*, *19*(11), 2331–2344. https://doi.org/10.1016/j.celrep.2017.05.065

Wang, H., Bloom, O., Zhang, M., Vishnubhakat, J. M., Ombrellino, M., Che, J., Frazier, A., Yang, H., Ivanova, S., Borovikova, L., Manogue, K. R., Faist, E., Abraham, E., Andersson, J., Andersson, U., Molina, P. E., Abumrad, N. N., Sama, A., & Tracey, K. J. (1999). HMG-1 as a Late Mediator of Endotoxin Lethality in Mice. *Science*, *285*(5425), 248–251. https://doi.org/10.1126/science.285.5425.248

Wang, J.-b., Pu, S.-b., Sun, Y., Li, Z.-f., Niu, M., Yan, X.-z., Zhao, Y.-l., Wang, L.-f., Qin, X.-m., Ma, Z.-j., Zhang, Y.-m., Li, B.-s., Luo, S.-q., Gong, M., Sun, Y.-q., Zou, Z.-s., & Xiao, X.-h. (2014). Metabolomic Profiling of Autoimmune Hepatitis: The Diagnostic Utility of Nuclear Magnetic Resonance Spectroscopy. *Journal of Proteome Research*, *13*(8), 3792–3801. https://doi.org/10.1021/pr500462f

Ward, M. W., Rego, A. C., Frenguelli, B. G., & Nicholls, D. G. (2000). Mitochondrial Membrane Potential and Glutamate Excitotoxicity in Cultured Cerebellar Granule Cells. *The Journal of Neuroscience*, *20*(19), 7208–7219. https://doi.org/10.1523/JNEUROSCI.20-19-07208.2000

Wen, Y., Lambrecht, J., Ju, C., & Tacke, F. (2021). Hepatic macrophages in liver homeostasis and diseases-diversity, plasticity and therapeutic opportunities. *Cellular & Molecular Immunology*, *18*(1), 45–56. https://doi.org/10.1038/s41423-020-00558-8

Wenfeng, Z., Yakun, W., Di, M., Jianping, G., Chuanxin, W., & Chun, H. (2014). Kupffer cells: increasingly significant role in nonalcoholic fatty liver disease. *Annals of Hepatology*, *13*(5), 489–495. https://doi.org/10.1016/S1665-2681(19)31247-5

Wilson, N. J., Boniface, K., Chan, J. R., McKenzie, B. S., Blumenschein, W. M., Mattson, J. D., Basham, B., Smith, K., Chen, T., Morel, F., Lecron, J.-C., Kastelein, R. A., Cua, D. J., McClanahan, T. K., Bowman, E. P., & de Waal Malefyt, R. (2007). Development, cytokine profile and function of human interleukin 17–producing helper T cells. *Nature Immunology*, *8*(9), 950–957. https://doi.org/10.1038/ni1497

Xia, G., Wu, S., Wang, X., & Fu, M. (2018). Inhibition of microRNA-155 attenuates concanavalin-A-induced autoimmune hepatitis by regulating Treg/Th17 cell differentiation. *Canadian Journal of Physiology and Pharmacology*, *96*(12), 1293–1300. https://doi.org/10.1139/cjpp-2018-0467

Xie, M., Yu, Y., Kang, R., Zhu, S., Yang, L., Zeng, L., Sun, X., Yang, M., Billiar, T. R., Wang, H., Cao, L., Jiang, J., & Tang, D. (2016). PKM2-dependent glycolysis promotes NLRP3 and AIM2 inflammasome activation. *Nature Communications*, *7*, 13280. https://doi.org/10.1038/ncomms13280

Xu, F., Guo, M., Huang, W., Feng, L., Zhu, J., Luo, K., Gao, J., Zheng, B., Kong, L.-D., Pang, T., Wu, X., & Xu, Q. (2020). Annexin A5 regulates hepatic macrophage polarization via directly

targeting PKM2 and ameliorates NASH. *Redox Biology*, *36*, 101634. https://doi.org/10.1016/j.redox.2020.101634

Xu, R., Li, Y., Yan, H., Zhang, E., Huang, X., Chen, Q., Chen, J., Qu, J., Liu, Y., He, J., Yi, Q., & Cai, Z. (2019). CCL2 promotes macrophages-associated chemoresistance via MCPIP1 dual catalytic activities in multiple myeloma. *Cell Death & Disease*, *10*(10), 781. https://doi.org/10.1038/s41419-019-2012-4

Ye, M., Iwasaki, H., Laiosa, C. V., Stadtfeld, M., Xie, H., Heck, S., Clausen, B., Akashi, K., & Graf, T. (2003). Hematopoietic Stem Cells Expressing the Myeloid Lysozyme Gene Retain Long-Term, Multilineage Repopulation Potential. *Immunity*, *19*(5), 689–699. https://doi.org/10.1016/S1074-7613(03)00299-1

Zhao, L., Tang, Y., You, Z., Wang, Q., Liang, S., Han, X., Qiu, D., Wei, J., Liu, Y., Shen, L., Chen, X., Peng, Y., Li, Z., & Ma, X. (2011). Interleukin-17 Contributes to the Pathogenesis of Autoimmune Hepatitis through Inducing Hepatic Interleukin-6 Expression (P. Proost, Ed.). *PLoS ONE*, *6*(4), e18909. https://doi.org/10.1371/journal.pone.0018909

Zhou, Z., Li, M., Zhang, L., Zhao, H., Şahin, Ö., Chen, J., Zhao, J. J., Songyang, Z., & Yu, D. (2018). Oncogenic Kinase–Induced PKM2 Tyrosine 105 Phosphorylation Converts Nononcogenic PKM2 to a Tumor Promoter and Induces Cancer Stem–like Cells. *Cancer Research*, *78*(9), 2248–2261. https://doi.org/10.1158/0008-5472.CAN-17-2726

Zhuang, Y., Li, Y., Li, X., Xie, Q., & Wu, M. (2016). Atg7 Knockdown Augments Concanavalin A-Induced Acute Hepatitis through an ROS-Mediated p38/MAPK Pathway (B. Ryffel, Ed.). *PLOS ONE*, *11*(3), e0149754. https://doi.org/10.1371/journal.pone.0149754

Zimmermann, H. W., Trautwein, C., & Tacke, F. (2012). Functional role of monocytes and macrophages for the inflammatory response in acute liver injury. *Frontiers in Physiology*, *3 OCT*(October), 1–18. https://doi.org/10.3389/fphys.2012.00056

Zou, K., Wang, Y., Hu, Y., Zheng, L., Xu, W., & Li, G. (2017). Specific tumor-derived CCL2 mediated by pyruvate kinase M2 in colorectal cancer cells contributes to macrophage recruitment in tumor microenvironment. *Tumor Biology*, *39*(3), 101042831769596. https://doi.org/10.1177/1010428317695962

List of Figures

List of Tables

List of Abbreviations

Abbreviation	Complete technical term
ACTB	β-Actin
AF	AlexaFluor®
ALT	Alanine aminotransferase
ANOVA	Analysis of variance
APC	Allophycocyanin
ARG1	Arginase 1
ATP	Adenosine triphosphate
BMDM	Bone marrow derived macrophage(s)
bp	Base pair
BSA	Bovine serum albumin
BV	Brilliant Violet™
CASP-1	Caspase 1
CCL	C-C motif chemokine ligand
CCR	C-C motif chemokine receptor
CD	Cluster of differentiation
cDNA	Complementary → DNA
CPT1α	Carnitine palmitoyltransferase I subunit α
CO_2	Carbon dioxide
CoA	Coenzyme A
ConA	Concanavalin A
Cre	Cyclization recombinase, "causes recombination"
CX3CR1	CX3C chemokine receptor 1
CYP	Cytochrome P450
DEPC	Diethyl pyrocarbonate
DMSO	Dimethyl sulfoxide
DNA	Deoxyribonucleic acid
dNTP	Deoxynucleotide triphosphate
DPBS	Dulbecco's Phosphate Buffered Saline
ECAR	Extracellular acidification rate
EDTA	Ethylenediaminetetraacetic acid (EDTA)
ELISA	Enzyme-linked immunosorbent assay
ETC	Electron transport chain
F6P	Fructose 6-phosphate
FACS	Fluorescence activated cell sorting
FASN	Fatty acid synthase
FBC	Fetal bovine serum
FBP	Fructose 1,6-bisphosphate
FCCP	Carbonyl cyanide-4-(trifluoromethoxy)phenylhydrazone
FCS	Fetal calf serum
FGFR	Fibroblast growth factor receptor
FITC	Fluorescein isothiocyanate
fl	Floxed allele
FMO	Fluorescence minus one
Foxp3	Forkhead box protein 3
FSC	Forward scatter
g	gravitational force equivalent

H_2O	Water
HBSS	Hank's Balanced Salt Solution
HCC	Hepatocellular carcinoma
H&E	Hematoxylin & Eosin
HIF	Hypoxia-inducible factor
HMGB1	High mobility group box 1
HRP	Horseradish peroxidase
Ig	Immunoglobulin
IHC	Immunohistochemistry
IL	Interleukin
i.p.	intraperitoneal
IU	International units
i.v.	intravenous
kbp	kilobase pair
KC	Kupffer cell(s)
kDa	Kilodalton
L929	Murine fibroblast cell line
LDH	Lactate dehydrogenase
LDS	Lithium dodecyl sulfate
loxP	Locus of X-over P1
LPS	Lipopolysaccharides
Ly6C	Lymphocyte antigen 6 complex locus C
Ly6G	Lymphocyte antigen 6 complex locus G
LysM	Lysozyme, murine
M-CSF	Macrophage colony-stimulating factor
MFI	Mean fluorescence intensity
MPO	Myeloperoxidase
mRNA	Messenger → RNA
NAFLD	Non-alcoholic fatty liver disease
NaOH	Sodium hydroxide
NASH	Non-alcoholic steatohepatisis
NF-κB	Nuclear factor κ-light-chain-enhancer of activated B-cells
NLRP3	NLR family pyrin domain containing 3
NPC	Non-parenchymal cell(s)
ns	Not significant
O_2	Oxygen
OCR	Oxygen consumption rate
p	*probabilitas* (lat.)
PBS	Phosphate buffered saline
PCR	Polymerase chain reaction
PD-1	Programmed cell death protein 1
PD-L1	Programmed cell death ligand 1
PE	Phycoerythrin
PFA	Para-formaldehyde
PFK	Phosphofructokinase
PKM	Pyruvate kinase muscle isozyme
$Pkm2^{fl/fl}$	PKM2 control mice (see section 3.1.1)
$Pkm2^{\Delta myel}$	PKM2 knockdown mice (see section 3.1.1)
PPAR	Peroxisome proliferator-activated receptor

qPCR	Quantitative real time → PCR
rpm	Revolutions per minute
RNA	Ribonucleic acid
RPMI	Roswell Park Memorial Institute (Medium)
SAICAR	Succinylaminoimidazolecarboxamide ribose-5' phosphate
SDH	Succinate dehydrogenase
SDS	Sodium dodecyl sulfate
SLC	Solute carrier
SOCS	Suppressor of cytokine signalling
SRC	Proto-oncogene tyrosine-protein kinase SRC
SREBF	Sterol regulatory element-binding factor
SSC	Sideward scatter
TCA	Tricarboxylic acid cycle
TIGIT	T cell immunoreceptor with Ig and ITIM domains
TNFα	Tumor necrosis factor α
TRIS	Tris(hydroxymethyl)aminomethane
U	Unit(s)
UT	Untreated
V	Volt
w/v	Weight per volume
+	Wiltype allele
Δ	Genetically modified allele

Acknowledgements

Die Erstellung dieser Arbeit wäre ohne die Unterstützung von verschiedenster Seite nicht möglich gewesen. Zu allererst möchte ich mich herzlich bei meiner Promotionsbetreuerin und Doktormutter, Frau PD Dr. Andrea Kristina Horst, bedanken. Im Rahmen eines Wahlfachseminars über das *tumor microenvironment* kam es über ein paar Umwege schließlich zu diesem Forschungsprojekt. Ich bekam unter ihrer Supervision die Gelegenheit, mich intensiv mit einem komplexen Hypothesenkomplex auseinanderzusetzen und erhielt neben der Anleitung zum selbstständigen Erarbeiten zahlreiche Impulse zur Weiterentwicklung des Projekts. Ein direkter und freundlicher Draht, zusammen mit einer gehörigen Portion Humor für den Wahnsinn des Laboralltags war von der experimentellen Laborarbeit bis zur schriftlichen Ausführung der Dissertation gegeben, wofür ich ihr ausdrücklich danke. Ferner möchte ich auch Frau Prof. Dr. Gisa Tiegs danken, die als Leiterin des Instituts für experimentelle Immunologie und Hepatologie die Durchführung dieser Arbeit ermöglicht hat. In diesem Zusammenhang gilt mein Dank auch den Verantwortlichen des Sonderforschungsbereichs 841, die diese Arbeit freundlicherweise mit einem Forschungsstipendium und einem supportiven wissenschaftlichen Umfeld unterstützt haben.

Einen überproportionalen Anteil meiner Dankbarkeit verdienen unsere technischen Assistenten Paulina Sprezyna, Carsten Rothkegel und Elena Tasika. Neben händischen Tricks und Hilfestellungen bei Experimenten zu absoluten Unzeiten hattet ihr stets ein offenes Ohr für Bitten und (zahlreiche) Nachfragen. Ohne euch wäre kein einziges Blatt dieser Arbeit zustandegekommen. Prof. Dr. Udo Schumacher und Tobias Gosau (Institut für Anatomie und experimentelle Morphologie) möchte ich in diesem Zuge für die Unterstützung beim Ausgießen von Paraffinblöcken und der Anfertigung von H&E-Färbungen danken. Benjamin Dreyer und Dr. Barbara Finckh vom Institut für Klinische Chemie und Laboratoriumsmedizin danke ich herzlich für die Kooperation und die Auswertung der Massenspektrometriedaten, die in dieser Arbeit enthalten sind. Ein besonderer Dank geht darüber hinaus an meine Kolleginnen und Kollegen im IEIH, insbesondere an Mareike Kellerer, Dr. Laura Berkhout, Dr. Gevitha Ananthavettivelu, Dr. Birgit Schiller und Dr. Jessica Endig, die von mir häufig in die Durchführung von Experimenten mit einbezogen wurden, die nicht ihre eigenen waren, und die mir trotzdem Geduldig mit Rat oder Tat zur Seite standen. Außerdem bedanke ich mich bei meinen Doktorandenkollegen Marek Schoedsack und Dr. Philippe Breda, die während und auch nach der offiziellen Arbeitszeit meine Gesamtmoral deutlich gehoben haben. Abseits des Labors danke ich Dr. Julia Hoppe, Dr. Falko Brinkmann, Nikolai Reinke, Janis Vernier und Doris Zahner für die Unterstützung beim Schreiben (sei es durch die Bereitstellung eines Arbeitsplatzes, LaTeX-Support, Fragen zum Grafikdesign oder zur Statistik oder durch die Erstellung eines Mauspiktogramms).

Zu allerletzt möchte ich mich von Herzen bei meinen Eltern, meiner ganzen Familie und meinem Freund Bastian Cheng bedanken. Ohne eure fortwährende Unterstützung auf verschiedenster Ebene hätte ich die Kraft zur Fertigstellung nicht aufbringen können.

Curriculum Vitae

Personal Information

Last Name	Weltzsch
First Names	Jan Philipp
Date of Birth	01 April 1992, Hamburg
Parents	Barbara Elisabeth Weltzsch, geb. Spieler
	Dr. med. dent. Michael Edgar Herrmann Weltzsch
Address	Vereinsstrasse 81, 20357 Hamburg, Germany

Education

2002 - 2010	Gymnasium Hochrad, Hamburg
06/2010	Allgemeine Hochschulreife
10/2011 - 09/2012	Studies in Musical Composition and Musical Theory,
	University of Music and Theater, Hamburg
10/2013 - 11/2020	Studies in Medicine, University of Hamburg
	04/2016 1st State Examination
	10/2019 2nd State Examination
	11/2020 3rd State Examination
	12/2020 License to practice Medicine
Since 10/2016	Medical Doctorate (Dr. med.)
	Institute for Experimental Immunology and Hepatology
	University Hospital Hamburg-Eppendorf, Germany
	Laboratory Director: Prof. Dr. rer. nat. Gisa Tiegs
	Supervisor: PD Dr. rer. nat. Andrea Kristina Horst

Scholarships

10/2016 - 09/2017	Doctoral scholarship, German Research Foundation
	Graduate School of the Collaborative Research Center 841
	Liver inflammation, infection, immune regulation and consequences
01/2020 - 03/2020	Hamburglobal Program, German Academic Exchange Service
	Academic stay, Universidad Autonoma de Queretaro, Mexico

Scientific Contributions

09/2017	47th Annual Meeting of the German Society For Immunology
	Activation of myeloid PKM2 protects from ConA-mediated liver injury
	Scientific Talk
	Erlangen, Germany
01/2018	34th Annual Meeting of the German Association for the Study of the Liver
	Activation of myeloid PKM2 protects from ConA-mediated liver injury
	Poster Presentation
	Hamburg, Germany

Eidesstattliche Versicherung

Ich versichere ausdrücklich, dass ich die vorliegende Arbeit selbstständig und ohne fremde Hilfe verfasst, andere als die von mir angegebenen Quellen und Hilfsmittel nicht benutzt und die aus den benutzten Werken wörtlich oder inhaltlich entnommenen Stellen einzeln nach Ausgabe (Auflage und Jahr des Erscheinens), Band und Seite des benutzten Werkes kenntlich gemacht habe.

Ferner versichere ich, dass ich die Dissertation bisher nicht einem Fachvertreter an einer anderen Hochschule zur Überprüfung vorgelegt oder mich anderweitig um Zulassung zur Promotion beworben habe. Ich erkläre mich einverstanden, dass meine Dissertation vom Dekanat der Medizinischen Fakultät mit einer gängigen Software zur Erkennung von Plagiaten überprüft werden kann.

Unterschrift: _____

Jan Philipp Weltzsch